공학박사 학위논문

Redox Properties of Heteropolyacid Catalysts Probed by Electrochemical Analysis, UV-visible Spectroscopy, and Scanning Tunneling Microscopy

전기화학적 분석, 자외선-가시광선 분광법 및 주사 터널링 현미경을 이용한 헤테로폴리산 촉매의 산화환원 특성연구

2015년 2월

서울대학교 대학원

화학생물공학부

최 정 호

Abstract

Redox Properties of Heteropolyacid Catalysts Probed by Electrochemical Analysis, UV-visible Spectroscopy, and Scanning Tunneling Microscopy

Jung Ho Choi

School of Chemical and Biological Engineering

The Graduate School

Seoul National University

Heteropolyacids (HPAs) are polymeric metal-oxide clusters that exhibit the diverse range of structures and compositions. Because of their robust structures and unique redox properties, HPAs have been widely employed as catalysts for several redox reactions. Catalytic oxidations over HPAs have been extensively studied over the past few decades and mixed-addenda HPAs have attracted recent attention due to the variety in stoichiometric combinations and outstanding redox natures. Physicochemical properties and catalytic activity of mixed-addenda HPAs can be easily tuned at molecular level by changing the constituent elements including counter-cation, central heteroatom, or framework addenda atom. Because a number of elements including metals, semimetals, and even non-metals could be incorporated into the HPA frameworks, a number of mixed-addenda HPAs with different structures can be

designed as a candidate for promising oxidation catalyst.

In this work, several series of transition metal-substituted HPAs were designed and synthesized. They were investigated by several experimental techniques including electrochemical analysis, UV-visible spectroscopy, and scanning tunneling microscopy (STM) in order to elucidate the effect of transition metal-substitution on redox properties and catalytic activities in oxidation catalysis. Furthermore, reliabilities of absorption edge energy and negative differential resistance (NDR) peak voltage as alternative parameters for the reducibility were also examined.

First, molybdenum-substituted $H_6P_2W_{18-x}Mo_xO_{62}$ (x=0, 3, 9, 15, 18) Wells-Dawson HPAs were prepared by "etherate method" to elucidate the effect of molybdenum-substitution on the redox properties and catalytic activity of Wells-Dawson-type tungstophosphates. Electrochemical measurements were conducted to elucidate the redox properties of HPAs. Several tungsten-based redox transitions were observed in the cyclic voltammogram of $H_6P_2W_{18}O_{62}$. However, $H_6P_2Mo_{18}O_{62}$ exhibited molybdenum-based redox transitions. Interestingly, molybdenum-substituted Wells-Dawson HPAs showed an additional molybdenum-centered redox transition at more positive potential. First electron reduction potentials increased with increasing molybdenum-substitution. UV-visible spectroscopy measurements were conducted to probe the electronic structure of bulk $H_6P_2W_{18-x}Mo_xO_{62}$ (x=0, 3, 9, 15, 18) Wells-Dawson HPAs. Absorption edge energy determined from the linear fit of $[F(R_\infty) \cdot h\nu]^{1/2}$ (Tauc plot) decreased with increasing molybdenum content. Scanning tunneling microscopy (STM) measurements were performed for the

further investigation about the local surface electronic structure of $H_6P_2W_{18-x}Mo_xO_{62}$ (x=0, 3, 9, 15, 18) Wells-Dawson HPAs. In STM measurements, two-dimensional self-assembled HPA arrays were observed. Tunneling spectra taken at bright corrugations showed a distinctive current-voltage responses, referred to as negative differential resistance (NDR) phenomenon. NDR peak voltage appeared at less negative voltage with increasing the molybdenum content. Gas-phase oxidative dehydrogenation of ethanol to acetaldehyde was carried out as a model reaction to probe the oxidation catalysis of $H_6P_2W_{18-x}Mo_xO_{62}$ (x=0, 3, 9, 15, 18) Wells-Dawson HPAs. Yield for acetaldehyde (oxidation product) increased with increasing molybdenum content. Among the tested catalysts, $H_6P_2Mo_{18}O_{62}$ with the highest reduction potential showed the best catalytic performance.

In order to explore the effect of group 5 metal (V and Nb)-substitution on redox properties and catalytic activity of Wells-Dawson-type tungstophosphates. α_2-$K_7P_2W_{17}V_1O_{62}$ and α_2-$K_7P_2W_{17}Nb_1O_{62}$ Wells-Dawson HPAs were synthesized via direct incorporation of transition metal into the mono-lacunary species to yield the selectively-substituted structures. α-$K_6P_2W_{18}O_{62}$ and α_2-$K_6P_2W_{17}Mo_1O_{62}$ were also prepared for the comparison. In the electrochemical analysis, molybdenum- and vanadium-substituted Wells-Dawson tungstophosphates showed additional molybdenum- and vanadium-based redox transitions, respectively, at more positive potential. However, niobium-substituted Wells-Dawson tungstophosphates showed significantly shifted redox transitions. First electron reduction potential increased in the order of α_2-$K_7P_2W_{17}Nb_1O_{62}$ < α-$K_6P_2W_{18}O_{62}$ < α_2-$K_6P_2W_{17}Mo_1O_{62}$ < α_2-$K_7P_2W_{17}V_1O_{62}$. Absorption edge energy determined by UV-visible

spectroscopy decreased in the order of α_2-$K_7P_2W_{17}Nb_1O_{62}$ > α-$K_6P_2W_{18}O_{62}$ > α_2-$K_6P_2W_{17}Mo_1O_{62}$ > α_2-$K_7P_2W_{17}V_1O_{62}$. STM images clearly showed the formation of self-assembled and well-ordered HPA arrays on HOPG surface. The trend of NDR peak voltage was also well consistent with that of absorption edge energy. Gas-phase oxidative dehydrogenation of benzylamine was carried out as a model reaction to probe oxidation catalysis. Yield for dibenzylimine (oxidation product) increased in the order of α_2-$K_7P_2W_{17}Nb_1O_{62}$ < α-$K_6P_2W_{18}O_{62}$ < α_2-$K_6P_2W_{17}Mo_1O_{62}$ < α_2-$K_7P_2W_{17}V_1O_{62}$.

Heteropolytungstates with different central atom, α-$H_nXW_{12}O_{40}$ ($X=Co^{2+}$, B^{3+}, Si^{4+}, and P^{5+}) Keggin HPAs were prepared to elucidate the effect of central atom on the redox properties and catalytic activity. All α-$H_nXW_{12}O_{40}$ HPAs exhibited well-defined reversible and stepwise tungsten-centered redox transitions during the electrochemical measurements. First electron reduction potential increased in the order of α-$H_6CoW_{12}O_{40}$ < α-$H_5BW_{12}O_{40}$ < α-$H_4SiW_{12}O_{40}$ < α-$H_3PW_{12}O_{40}$. Absorption edge energy determined by UV-visible spectroscopy decreased in the order of α-$H_6CoW_{12}O_{40}$ > α-$H_5BW_{12}O_{40}$ > α-$H_4SiW_{12}O_{40}$ > α-$H_3PW_{12}O_{40}$. The trend of NDR peak voltage was also well consistent with that of absorption edge energy. Among the tested, PO_4^{3-} anion with smaller negative charge and lager size was the most effective to enhance the reducibility.

Another series of heteropolytungstates containing AsO_4^{3-} as a central unit were also examined to elucidate the effect of transition metal-substitution on the redox properties and catalytic activities of Wells-Dawson-type tungstoarsenates. A series of α-$K_6As_2W_{18-x}Mo_xO_{62}$ (x=0-3) Wells-Dawson HPAs were prepared via direct incorporation of transition metal into the mono-,

di-, and tri-lacunary species. In electrochemical analysis, α-$K_6As_2W_{18}O_{62}$ exhibited four tungsten-centered redox transitions. However, molybdenum-substituted α-$K_6As_2W_{18-x}Mo_xO_{62}$ (x=1-3) exhibited an additional molybdenum-centered redox transition at more positive potential. First electron reduction potential increased with increasing molybdenum content. Absorption edge energy determined by UV-visible spectroscopy decreased with increasing molybdenum content. It is interesting to note that NDR peak voltage appeared at less negative voltage with increasing molybdenum content. These results are nearly same with the results in the series of $H_6P_2W_{18-x}Mo_xO_{62}$ (x=0, 3, 9, 15, 18). Gas-phase oxidative dehydrogenation of benzyl alcohol was carried out as a model reaction to track the oxidation catalysis. Yield for benzaldehyde (oxidation product) increased with increasing molybdenum content.

Furthermore, group 5 metal-substituted α_2-$K_7As_2W_{17}V_1O_{62}$ and α_2-$K_7As_2W_{17}Nb_1O_{62}$ Wells-Dawson HPAs were synthesized via direct incorporation of transition metal into the mono-lacunary species to yield the selectively-substituted structures. α-$K_6As_2W_{18}O_{62}$ and α_2-$K_6As_2W_{17}Mo_1O_{62}$ were also prepared for the comparison. In the electrochemical analysis, molybdenum- and vanadium-substituted Wells-Dawson tungstoarsenates showed additional molybdenum- and vanadium-based redox transitions, respectively, at more positive potential. However, niobium-substituted Wells-Dawson tungstoarsenates showed significantly shifted redox transitions. First electron reduction potential increased in the order of α_2-$K_7As_2W_{17}Nb_1O_{62}$ < α-$K_6As_2W_{18}O_{62}$ < α_2-$K_6As_2W_{17}Mo_1O_{62}$ < α_2-$K_7As_2W_{17}V_1O_{62}$. Absorption edge energy determined by UV-visible spectroscopy decreased in the order of α_2-$K_7As_2W_{17}Nb_1O_{62}$ > α-$K_6As_2W_{18}O_{62}$ > α_2-$K_6As_2W_{17}Mo_1O_{62}$ > α_2-

$K_7As_2W_{17}V_1O_{62}$. Gas-phase oxidative dehydrogenation of benzylamine was carried out as a model reaction to track the oxidation catalysis. Yield for dibenzylimine (oxidation product) increased in the order of α_2-$K_7As_2W_{17}Nb_1O_{62}$ < α-$K_6As_2W_{18}O_{62}$ < α_2-$K_6As_2W_{17}Mo_1O_{62}$ < α_2-$K_7As_2W_{17}V_1O_{62}$.

In summary, several series of transition metal-substituted HPA catalysts with different addenda atoms, central atoms, contents, and structures were prepared, characterized, and applied to the model reactions in order to elucidate the redox properties and catalytic activities in oxidation catalysis. Reliabilities of absorption edge energy and NDR peak voltage as alternative parameters for the redox properties were also examined. It was found that redox properties were easily tunable by changing the constituent elements. In addition, it could be concluded that redox properties of HPAs, which is closely related to the electronic structure, play an important role to determine the catalytic activities in the oxidation catalysis and absorption edge energy and NDR peak voltage can be utilized as alternative parameters to estimate the reducibility of HPAs.

Keywords: Heteropolyacids, Transition metal, Redox property, Oxidation catalysis, Electronic structure

Student Number: 2010-21019

Contents

Chapter 1. Introduction 1

1.1. Heteropolyacids (HPAs)..... 1

1.2. Characteristics of HPAs 5

1.2.1. General properties and applications 5

1.2.2. Redox properties 10

1.3. Oxidation catalysis over HPAs..... 13

Chapter 2. Experimental..... 16

2.1. Mo(VI)-substituted Wells-Dawson-type tungstophosphates 16

2.1.1. Preparation 16

2.1.2. Characterization 17

2.1.2.1. Formation of HPA structure 17

2.1.2.2. Electrochemical analysis 17

2.1.2.3. UV-visible spectroscopy.....18

2.1.2.4. Scanning tunneling microscopy 18

2.1.3. Catalytic test (oxidative dehydrogenation of ethanol) 20

2.2. V(V) and Nb(V)-substituted Wells-Dawson-type tungstophosphates 21

2.2.1. Preparation 21

2.2.1.1. Preparation of tungstophosphate (α-$K_6P_2W_{18}O_{62}$) .21

2.2.1.2. Preparation of mono-lacunary tungstophosphate (α_2-$K_{10}P_2W_{17}O_{61}$).....22

2.2.1.3. Preparation of α_2-$K_7P_2W_{17}M_1O_{62}$ (M=V and Nb) ..22

2.2.2. Characterization 24

2.2.2.1. Formation of HPA structure 24

2.2.2.2. Electrochemical analysis 24
2.2.2.3. UV-visible spectroscopy 25
2.2.2.4. Scanning tunneling microscopy 25
2.2.3. Catalytic test
(oxidative dehydrogenation of benzylamine) 27

2.3. Keggin-type heteropolytungstates with
different central atom 28
2.3.1. Preparation 28
2.3.1.1. Preparation of α-$H_3PW_{12}O_{40}$ and α-$H_4SiW_{12}O_{40}$ 28
2.3.1.2. Preparation of α-$H_5BW_{12}O_{40}$ 28
2.3.1.3. Preparation of α-$H_6CoW_{12}O_{40}$ 29
2.3.2. Characterization 30
2.3.2.1. Formation of HPA structure 30
2.3.2.2. Electrochemical analysis 30
2.3.2.3. UV-visible spectroscopy 31
2.3.2.4. Scanning tunneling microscopy 31

2.4. Mo(VI)-substituted Wells-Dawson-type tungstoarsenates .. 32
2.4.1. Preparation 32
2.4.1.1. Preparation of α-$K_6As_2W_{18}O_{62}$ 32
2.4.1.2. Preparation of mono-lacunary tungstoarsenate
(α_2-$K_{10}As_2W_{17}O_{61}$) 33
2.4.1.3. Preparation of di-lacunary tungstoarsenate
(α-$K_{11}HAs_2W_{16}O_{59}$) 33
2.4.1.4. Preparation of tri-lacunary tungstoarsenate
(α-$Na_{12}As_2W_{15}O_{56}$) 33
2.4.1.5. Preparation of α-$K_6As_2W_{18-x}Mo_xO_{62}$ (x=1-3) 34
2.4.2. Characterization 35

2.4.2.1. Formation of HPA structure 35
2.4.2.2. Electrochemical analysis 35
2.4.2.3. UV-visible spectroscopy.....36
2.4.2.4. Scanning tunneling microscopy 36
2.4.3. Catalytic test
(oxidative dehydrogenation of benzyl alcohol).....38

2.5. V(V) and Nb(V)-substituted Wells-Dawson-type tungstoarsenates 39
2.5.1. Preparation 39
2.5.1.1. Preparation of α_2-$K_7As_2W_{17}V_1O_{62}$ 39
2.5.1.2. Preparation of α_2-$K_7As_2W_{17}Nb_1O_{62}$.....39
2.5.2. Characterization 41
2.5.2.1. Formation of HPA structure 41
2.5.2.2. Electrochemical analysis 41
2.5.2.3. UV-visible spectroscopy.....42
2.5.3. Catalytic test
(oxidative dehydrogenation of benzyl amine).....43

Chapter 3. Results and Discussion 44

3.1. Mo(VI)-substituted Wells-Dawson-type tungstophosphates 44
3.1.1. Formation of HPA structure 44
3.1.2. Characterization 50
3.1.2.1. Cyclic voltammetry.....50
3.1.2.2. UV-visible spectroscopy.....53
3.1.2.3. Scanning tunneling microscopy 56
3.1.3. Catalytic test.....64

3.2. V(V) and Nb(V)-substituted Wells-Dawson-type tungstophosphates 67
3.2.1. Formation of HPA structure 67
3.2.2. Characterization 74
3.2.2.1. Cyclic voltammetry 74
3.2.2.2. UV-visible spectroscopy 76
3.2.2.3. Scanning tunneling microscopy 79
3.2.3. Catalytic test 85

3.3. Keggin-type heteropolytungstates with different central atom 89
3.3.1. Formation of HPA structure 89
3.3.2. Characterization 93
3.3.2.1. Cyclic voltammetry 93
3.3.2.2. UV-visible spectroscopy 96
3.3.2.3. Scanning tunneling microscopy 98

3.4. Mo(VI)-substituted Wells-Dawson-type tungstoarsenates 101
3.4.1. Formation of HPA structure 101
3.4.2. Characterization 107
3.4.2.1. Cyclic voltammetry 107
3.4.2.2. UV-visible spectroscopy 109
3.4.2.3. Scanning tunneling microscopy 111
3.4.3. Catalytic test 117

3.5. V(V) and Nb(V)-substituted Wells-Dawson-type tungstoarsenates 119
3.5.1. Formation of HPA structure 119
3.5.2. Characterization 125
3.5.2.1. Cyclic voltammetry 125

3.5.2.2. UV-visible spectroscopy.....127
3.5.3. Catalytic test.....132

Chapter 4. Conclusions 134

Bibliography..... 139

초 록..... 146

List of Tables

Table 1.1 General characteristics of several HPAs....8
Table 1.2 Other applications of HPAs....9
Table 1.3 Examples of type I (reducible) and type II (irreducible) heteropolyanions....12
Table 1.4 Oxidation catalysis over HPAs....15
Table 3.1 Detailed assignment of each band of $H_6P_2W_{18-x}Mo_xO_{62}$ (x=0, 3, 9, 15, 18) Wells-Dawson HPAs....48
Table 3.2 Chemical compositions of phosphorous, tungsten, and molybdenum in the $H_6P_2W_{18-x}Mo_xO_{62}$ (x=0, 3, 9, 15, 18) Wells-Dawson HPAs....49
Table 3.3 First electron reduction potentials, absorption edge energies, and NDR peak voltages of $H_6P_2W_{18-x}Mo_xO_{62}$ (x=0, 3, 9, 15, 18) Wells-Dawson HPAs....62
Table 3.4 Detailed assignment of each characteristic band....71
Table 3.5 Chemical compositions of phosphorous, tungsten, and substituted-metal (M) in the α-$K_6P_2W_{18}O_{62}$, α_2-$K_6P_2W_{17}Mo_1O_{62}$, α_2-$K_7P_2W_{17}V_1O_{62}$, and α_2-$K_7P_2W_{17}Nb_1O_{62}$ Wells-Dawson HPAs ...73
Table 3.6 First electron reduction potentials, absorption edge energies, and NDR peak voltages of α-$K_6P_2W_{18}O_{62}$, α_2-$K_6P_2W_{17}Mo_1O_{62}$, α_2-$K_7P_2W_{17}V_1O_{62}$, and α_2-$K_7P_2W_{17}Nb_1O_{62}$ Wells-Dawson HPAs....83
Table 3.7 Chemical compositions of central atom (X) and tungsten in the α-$H_nXW_{12}O_{40}$ (X=Co^{2+}, B^{3+}, Si^{4+}, and P^{5+}) Keggin HPAs....92
Table 3.8 First electron reduction potentials, absorption edge energies, and NDR peak voltages of α-$H_nXW_{12}O_{40}$ (X=Co^{2+}, B^{3+}, Si^{4+}, and P^{5+}) Keggin HPAs....99
Table 3.9 Detailed assignment of each characteristic band....105
Table 3.10 Chemical compositions of arsenic, tungsten, and molybdenum in the α-$K_6As_2W_{18-x}Mo_xO_{62}$ (x=0-3) Wells-Dawson HPAs 106
Table 3.11 First electron reduction potentials, absorption edge energies, and NDR peak voltages of α-$K_6As_2W_{18-x}Mo_xO_{62}$ (x=0-3) Wells-Dawson HPAs....115

Table 3.12 Detailed assignment of each characteristic band.....123
Table 3.13 Chemical compositions of arsenic, tungsten, and substituted-metal (M) in the α-$K_6As_2W_{18}O_{62}$, α_2-$K_6As_2W_{17}Mo_1O_{62}$, α_2-$K_7As_2W_{17}V_1O_{62}$, and α_2-$K_7As_2W_{17}Nb_1O_{62}$ Wells-Dawson HPAs.....124
Table 3.14 First electron reduction potentials and absorption edge energies of α-$K_6As_2W_{18}O_{62}$, α_2-$K_6As_2W_{17}Mo_1O_{62}$, α_2-$K_7As_2W_{17}V_1O_{62}$, and α_2-$K_7As_2W_{17}Nb_1O_{62}$ Wells-Dawson HPAs.....130

List of Figures

Fig. 1.1 Schematic representations of (a) primary structure, (b) secondary structure, and (c) tertiary structure of Keggin-type HPAs.....3

Fig. 1.2 Several structures that can be derived from the Keggin- and Wells-Dawson-type heteropolyanions.....4

Fig. 3.1 Schematic diagram for the preparation procedures of $H_6P_2W_{18-x}Mo_xO_{62}$ (x=0, 3, 9, 15, 18) Wells-Dawson HPAs.....46

Fig. 3.2 DRIFT spectra of $H_6P_2W_{18-x}Mo_xO_{62}$ (x=0, 3, 9, 15, 18) Wells-Dawson HPAs.....47

Fig. 3.3 Cyclic voltammograms of (a) $H_6P_2W_{18}O_{62}$ and (b) $H_6P_2Mo_{18}O_{62}$ Wells-Dawson HPAs.....52

Fig. 3.4 $[F(R_\infty) \cdot h\nu]^{1/2}$ curves of $H_6P_2W_{18-x}Mo_xO_{62}$ (x=0, 3, 9, 15, 18) Wells-Dawson HPAs.....55

Fig. 3.5 STM images of (a) $H_6P_2W_{18}O_{62}$ and (b) $H_6P_2Mo_{18}O_{62}$ Wells-Dawson HPAs.....59

Fig. 3.6 Typical current-voltage responses of (a) $H_6P_2W_{18}O_{62}$ and (b) $H_6P_2Mo_{18}O_{62}$ Wells-Dawson HPAs taken at two different sites (bright corrugation and interstitial space between bright corrugations) in Figure 3.5.....60

Fig. 3.7 Resonant tunneling model through a double barrier quantum well structure: (a) schematic representations and (b) corresponding spectra.....61

Fig. 3.8 Absorption edge energy and NDR peak voltage plotted as a function of reduction potential.....63

Fig. 3.9 (a) Catalytic performance of $H_6P_2Mo_{18}O_{62}$ during a 5 h-reaction and (b) yield for acetaldehyde after a 5 h-reaction plotted as a function of molybdenum content.....66

Fig. 3.10 Schematic diagram for the preparation procedures of α-$K_6P_2W_{18}O_{62}$, α_2-$K_6P_2W_{17}Mo_1O_{62}$, α_2-$K_7P_2W_{17}V_1O_{62}$, and α_2-$K_7P_2W_{17}Nb_1O_{62}$ Wells-Dawson HPAs.....69

Fig. 3.11 DRIFT spectra of α-$K_6P_2W_{18}O_{62}$, α_2-$K_6P_2W_{17}Mo_1O_{62}$, α_2-$K_7P_2W_{17}V_1O_{62}$, and α_2-$K_7P_2W_{17}Nb_1O_{62}$ Wells-Dawson HPAs....70

Fig. 3.12 ^{31}P NMR spectra of α-$K_6P_2W_{18}O_{62}$, α_2-$K_6P_2W_{17}Mo_1O_{62}$, α_2-$K_7P_2W_{17}V_1O_{62}$, and α_2-$K_7P_2W_{17}Nb_1O_{62}$ Wells-Dawson HPAs dissolved in D_2O.....72

Fig. 3.13 Cyclic voltammograms of (a) α-$K_6P_2W_{18}O_{62}$, (b) α_2-$K_6P_2W_{17}Mo_1O_{62}$, (c) α_2-$K_7P_2W_{17}V_1O_{62}$, and (d) α_2-$K_7P_2W_{17}Nb_1O_{62}$ Wells-Dawson HPAs 75

Fig. 3.14 $[F(R_\infty) \cdot h\nu]^{1/2}$ curves of α-$K_6P_2W_{18}O_{62}$, α_2-$K_6P_2W_{17}Mo_1O_{62}$, α_2-$K_7P_2W_{17}V_1O_{62}$, and α_2-$K_7P_2W_{17}Nb_1O_{62}$ Wells-Dawson HPAs....78

Fig. 3.15 STM images of (a) α_2-$K_7P_2W_{17}V_1O_{62}$ and (b) α_2-$K_7P_2W_{17}Nb_1O_{62}$ Wells-Dawson HPAs 81

Fig. 3.16 Typical tunneling spectra of (a) α_2-$K_7P_2W_{17}V_1O_{62}$ and (b) α_2-$K_7P_2W_{17}Nb_1O_{62}$ Wells-Dawson HPAs catalyst taken at two different sites (bright corrugation and interstitial space between bright corrugations) in Figure 3.15.....82

Fig. 3.17 Absorption edge energy and NDR peak voltage plotted as a function of reduction potential 84

Fig. 3.18 Plausible reaction mechanism for the oxidative dehydrogenation of benzylamine 87

Fig. 3.19 (a) Catalytic performance of α_2-$K_7P_2W_{17}V_1O_{62}$ during the 5 h-reaction and (b) yield for dibenzylimine after a 5 h-reaction.....88

Fig. 3.20 DRIFT spectra of α-$H_nXW_{12}O_{40}$ ($X=Co^{2+}$, B^{3+}, Si^{4+}, and P^{5+}) Keggin HPAs 91

Fig. 3.21 Cyclic voltammograms of α-$H_nXW_{12}O_{40}$ ($X=Co^{2+}$, B^{3+}, Si^{4+}, and P^{5+}) Keggin HPAs.....95

Fig. 3.22 $[F(R_\infty)\cdot h\nu]^{1/2}$ curves of α-$H_nXW_{12}O_{40}$ ($X=Co^{2+}$, B^{3+}, Si^{4+}, and P^{5+}) Keggin HPAs.....97

Fig. 3.23 Absorption edge energy and NDR peak voltage plotted as a function of reduction potential 100

Fig. 3.24 Schematic diagram for the preparation procedures of α-$K_6As_2W_{18-x}Mo_xO_{62}$ (x=0-3) Wells-Dawson HPAs.....103

Fig. 3.25 DRIFT spectra of α-$K_6As_2W_{18-x}Mo_xO_{62}$ (x=0-3) Wells-Dawson HPAs.....104

Fig. 3.26 Cyclic voltammograms of α-$K_6As_2W_{18-x}Mo_xO_{62}$ (x=0-3) Wells-Dawson HPAs.....108

Fig. 3.27 $[F(R_\infty)\cdot h\nu]^{1/2}$ curves of α-$K_6As_2W_{18-x}Mo_xO_{62}$ (x=0-3) Wells-Dawson HPAs.....110
Fig. 3.28 STM images of α-$K_6As_2W_{18}O_{62}$ Wells-Dawson HPA; (a) 20 x 20 nm and (b) 10 x 10 nm.....113
Fig. 3.29 Typical tunneling spectra of α-$K_6As_2W_{18}O_{62}$ Wells-Dawson HPA taken at two different sites (bright corrugation and interstitial space between bright corrugations) in Figure 3.28. 114
Fig. 3.30 Absorption edge energy and NDR peak voltage plotted as a function of reduction potential 116
Fig. 3.31 (a) Catalytic performance of α-$K_6As_2W_{18}O_{62}$ during a 5 h-reaction and (b) yield for acetaldehyde after a 5 h-reaction plotted as a function of molybdenum content 118
Fig. 3.32 Schematic diagram for the preparation procedures of α-$K_6As_2W_{18}O_{62}$, α_2-$K_6As_2W_{17}Mo_1O_{62}$, α_2-$K_7As_2W_{17}V_1O_{62}$, and α_2-$K_7As_2W_{17}Nb_1O_{62}$ Wells-Dawson HPAs.....121
Fig. 3.33 DRIFT spectra of α-$K_6As_2W_{18}O_{62}$, α_2-$K_6As_2W_{17}Mo_1O_{62}$, α_2-$K_7As_2W_{17}V_1O_{62}$, and α_2-$K_7As_2W_{17}Nb_1O_{62}$ Wells-Dawson HPAs.....122
Fig. 3.34 Cyclic voltammograms of α-$K_6As_2W_{18}O_{62}$, α_2-$K_6As_2W_{17}Mo_1O_{62}$, α_2-$K_7As_2W_{17}V_1O_{62}$, and α_2-$K_7As_2W_{17}Nb_1O_{62}$ Wells-Dawson HPAs.....126
Fig. 3.35 $[F(R_\infty)\cdot h\nu]^{1/2}$ curves of α-$K_6As_2W_{18}O_{62}$, α_2-$K_6As_2W_{17}Mo_1O_{62}$, α_2-$K_7As_2W_{17}V_1O_{62}$, and α_2-$K_7As_2W_{17}Nb_1O_{62}$ Wells-Dawson HPAs.....129
Fig. 3.36 Absorption edge energy plotted as a function of reduction potential 131
Fig. 3.37 (a) Catalytic performance of α_2-$K_7As_2W_{17}V_1O_{62}$ during the 5 h-reaction and (b) yield for dibenzylimine after a 5 h-reaction....133

Chapter 1. Introduction

1.1. Heteropolyacids (HPAs)

Heteropolyacids (HPAs) are polymeric oxoanion clusters with diverse range of molecular structures and compositions that exhibit the unique acid-base and redox nature. As shown in Eq. (1), acidic elements such as W, Mo, V, and Nb generally forms the oxoanions in the aqueous solution. These oxoanions polymerize at certain pH, temperature, and concentration. Polymerization proceeds until the strong inward polarization of exterior oxygen atoms terminates further polymerizations, resulting in small discrete metal-oxygen clusters. Polyanions comprising only a kind of oxoanion are called isopolyanion. Polyanions comprising more than two kinds of oxoanions are called heteropolyanion.

$$12WO_4^{2-} + HPO_4^{2-} + 23H^+ \rightarrow PW_{12}O_{40}^{3-} + 12H_2O \qquad (1)$$

Schematic representations of primary, secondary, and tertiary structures of Keggin-type HPAs are shown in Figure 1.1. Keggin-type heteropolyanion, which has a general formula of $XM_{12}O_{40}^{n-}$, comprises central atom (X), addenda atom (M), and framework oxygen. A central tetrahedral XO_4 unit is surrounded by four octahedral M_3O_{13} units, resulting in soccer ball-shaped Keggin-type heteropolyanion.

Heteropolyanions are generally coordinated with charge-compensating counter-cations (e.g. protonated water dimer, $H_5O_2^+$) and other polar molecules to form the secondary structures. Heteropolyanions are linked each other by hydrogen bonding at the terminal or bridged oxygen. Other elements such as Na^+, NH_4^+, or Cs^+ are also available as a counter-cation. Tertiary structure is the structure of solid heteropoly compounds as assemble. Counter-cation plays an important role to determine the tertiary structure. The salts of small cation (e.g. Na^+) are generally highly water-soluble and possess low surface. On the other hand, the salts of large cation (e.g. Cs^+) are generally insoluble in water and possess high surface area [1].

Since Keggin-type heteropoly compounds had been discovered by Berzelius, a number of structural types of heteropoly compounds such as Wells-Dawson- [2], Finke-Droege- [3], and Preyssler-type [4] have been discovered and structurally defined. Several geometrical isomers have also been discovered. Many structural classes of HPAs with a variation of molecular sizes, compositions, and structures are now investigated in the various fields of applications. Figure 1.2 shows the several structures that can be derived from Keggin- and Wells-Dawson-type heteropolyanions.

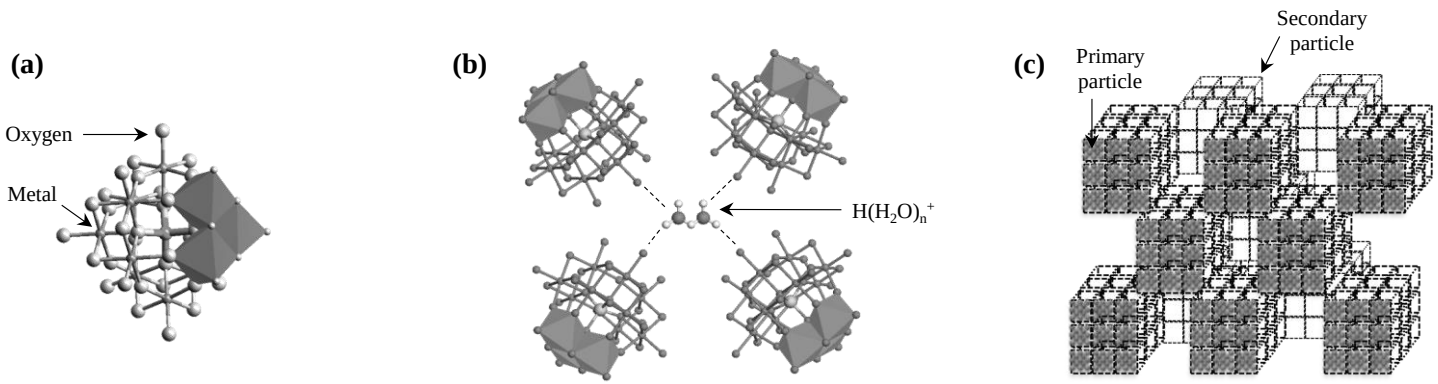

Fig. 1.1. Schematic representations of (a) primary structure, (b) secondary structure, and (c) tertiary structure of Keggin-type HPAs.

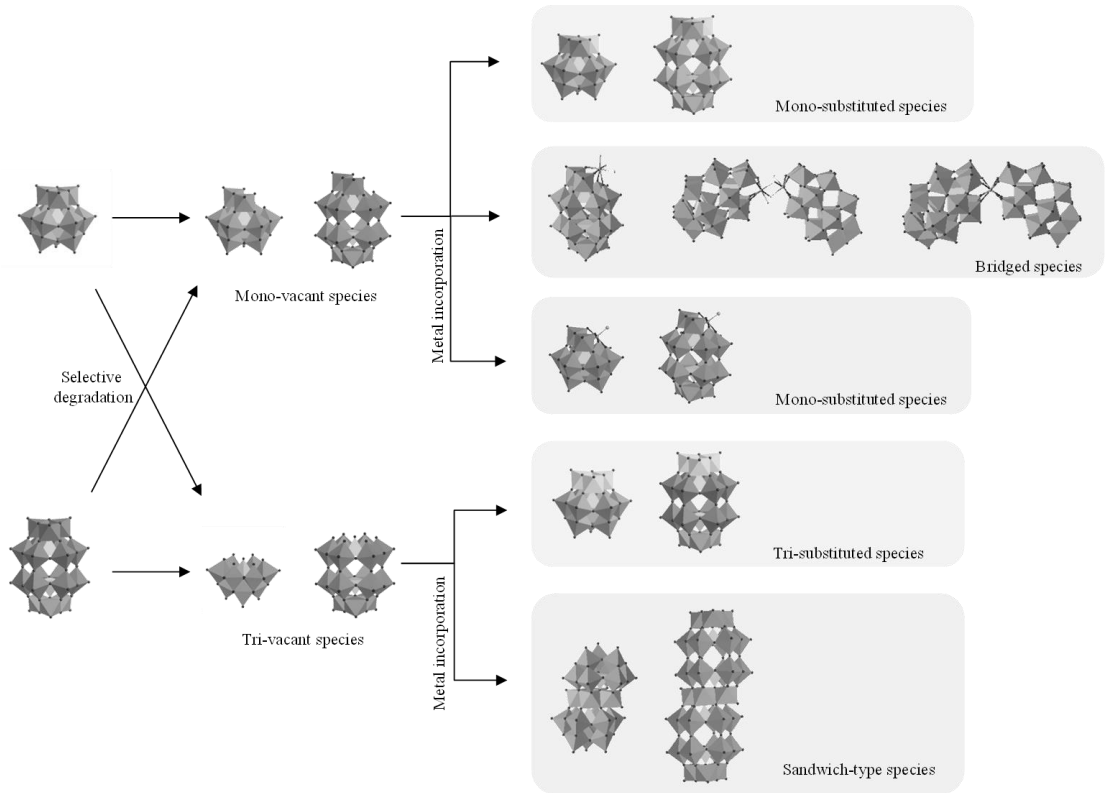

Fig. 1.2. Several structures that can be derived from Keggin- and Wells-Dawson-type heteropolyanions.

1.2. Characteristics of HPAs

1.2.1. General properties and applications

Physicochemical characteristics of HPAs that make them well suitable for the various fields of applications are listed as followings [5].

- Metal oxide-like material
- Stable under water/air and thermally stable
- Large size of heteropolyanion
- Discrete structure
- Anionic charge
- High ionic weight
- Fully oxidizable/reducible
- Variety in oxidation numbers for the addenda atoms
  ($E_{1/2}$ = +0.5 to -1.0 V vs. SCE)
- Color of oxidized forms/color of reduced forms
- Photoreducible
- Arrehenius acids ($pK_a < 0$)
- Can be incorporated more than 70 elements and form large number of structures
- Soluble in water and other oxygen carrying solvents (ethers, alcohols, ketones); also soluble or transferable into nonpolar solvents
- Hydrolysable to form deficient structures

The major applications of HPAs are found in the fields of catalysis. About 80-85 % of patents and applied literatures are related to the catalysis. The remaining 15-20 % of applications include coatings, analytical chemistry, membranes, sensors, dye, electrochemistry, capacitors, dopants, and clinical analysis (Table 1.2).

Most of all, excellent acid property is one of the most representative characteristics of HPAs. "Heteropolyacids", which are acid form of heteropoly compounds, are known to considerably stronger Brønsted acid than other mineral acids and solid acids. Therefore, most of the early researches on HPAs are focused on their acid properties. Free acids of Keggin-type and Wells-Dawson-type heteropolyanions could be isolated from aqueous solution by the "etherate method" introduced by Drechsel [6]. Recently, another route for the conversion of heteropolyanion salts to the corresponding free acids using ion exchange resins was also reported [7]. Large-scale industrial processes using HPAs as acid catalysts were already developed. Several examples are hydration of isobutene to *tert*-butyl alcohol and polymerization of tetrahydrofuran (THF) to polyoxytetramethyleneglycol (PTMEG), developed by Asahi Chemical Co. [8].

Another important characteristic of HPAs is the robust structure. Both chemical and thermal stabilities are very important in the catalytic applications. HPAs are highly stable in the most of oxidation states and exhibit inherent stability under oxidizing environments. Some HPAs are thermally stable up to ca. 600 ^{o}C and applicable in gas-phase reactions required harsh environments. It has been reported that thermal stability showed a variation with respect to counter-

cations in case of $PMo_{12}O_{40}^{3-}$; Ba^{2+}, Co^{2+} (673 K, decomposition temperature) < Cu^{2+}, Ni^{2+} (683 K) < H^{+}, Cd^{2+} (693 K) < Ca^{2+}, Mn^{2+} (700 K) < Mg^{2+} (710 K) < La^{2+}, Ce^{3+} (730 K) [9]. It was known that thermal changes in structures proceeds stepwise. Loss of water of crystallization occurs at the temperature below 473 K. At the higher temperature, acidic protons bound to the framework oxygen are released as a water (constitutional water) and HPAs finally decomposed to oxides.

Table 1.1

General characteristics of several HPAs [10]

HPAs	Soluble	Hydrolytic stability	Thermal stability
$H_6P_2W_{18}O_{62}$	H_2O, organic	pH ≤ 6	≤ 600 °C
$H_6P_2Mo_{18}O_{62}$	H_2O, organic	-	375 °C
$(NH_4)_6P_2W_{18}O_{62}$, $K_6P_2W_{18}O_{62}$, $(NH_4)_6As_2W_{18}O_{62}$,	H_2O, hot H_2O for K^+ salt	pH = 3-6 for oxidized species pH = 0-13 for reduced species	≤ 500 °C for $(NH_4)_6P_2W_{18}O_{62}$, ≤ 570 °C for $K_6P_2W_{18}O_{62}$
$(NH_4)_6P_2W_{18}O_{62}/TiO_2$	-	-	≤ 400 °C
$(NH_4)_6As_2Mo_{18}O_{62}$	H_2O	pH < 5.3	-
$P_2W_{18}M_4(H_2O)_2O_{68}^{10-}$ ($M = Co^{2+}$, Cu^{2+}, Zn^{2+})	H_2O	-	-
$Z_xP_2W_{17}O_{61}(M^{n+}{\cdot}L)$, ($Z = K^+$, Bu_4N^+) ($M^{n+} = Mn^{3+}$, Fe^{3+}, Co^{2+}, Ni^{2+}, Cu^{2+}) ($L = Br^-$, H_2O)	H_2O for ($Z = K^+$, $L = H_2O$) Organic ($Z = Bu_4N^+$, $L = Br^-$)	6.0 ≤ pH ≤ 7.0, 5.5 ≤ pH ≤ 9.0 for $M^{n+} = Co^{2+}$	-
$P_2W_{15}Nb_3O_{62}X_9$ ($X = K^+$, Li^+, Cs^+, Na^+, Bu_4N^+)	H_2O (K^+, Li^+, Cs^+, Na^+ salts)	-	473 °C, 492 °C, 529 °C, 534 °C for Li^+, Na^+, K^+, Cs^+, respectively
$Na_{16}[M_4(H_2O)_2(P_2W_{15}O_{56})_2]$ ($M = Mn^{2+}$, Ni^{2+}, Co^{2+}, Cu^{2+}, Zn^{2+})	H_2O	-	-
$[n\text{-}(C_4H_9)_6N]_6[C_5H_5TiP_2W_{15}V_3O_{62}]$	Organic solvent	-	-

Table 1.2

Other applications of HPAs [5]

HPAs	Applications
$H_4PMo_{11}V_1O_{40,}$ $H_5PMo_{10}V_2O_{40}$	Electrodes, capacitors
$H_3PMo_{12}O_{40}$, $H_3PW_{12}O_{40}$	Electrolytic capacitors
$(NH_4)_{10}H_2W_{12}O_{42}$, $(NH_4)_6P_2W_{12}O_{62}$	Corrosion inhibitors of Al alloys
$H_3PMo_{12}O_{40}$, $H_4SiW_{12}O_{40}$	Colorants for pigmenting paints, Printing inks and plastics
$H_4SiMo_{12}O_{40}$, $H_4SiW_{12}O_{40}$	Dyes for polyester and polyacrylonitrile
$H_4SiW_{12}O_{40}$	Dopants of polyaniline and polypyrrole
$H_3PW_{12}O_{40}$	Liquid H_2-O_2 fuel cell
$H_3PW_{12}O_{40}$	Photochromic coatings for copiers
$K_5SiW_{11}V_1O_{40}$, $Na_xH_{5-x}PMo_{10}V_2O_{40}$	Wood pulp bleaching
$PW_{11}O_{39}Fe^{III}(OH_2)^{4-}$	Electrode for NO determination
$H_3PMo_6W_6O_{40}$	Porous support for the purification of vent air
$H_5PMo_{10}V_2O_{40}$	Decontamination of mustard (HD) analogues
$H_4SiW_{12}O_{40}$ disk/SnO_2	Electrochromic display device

1.2.2. Redox properties

The addenda atoms in heteropolyanion frameworks are in their highest oxidation states. Therefore, HPAs are suitable for acting as an oxidizing agent. It is well known that Keggin-type molybdophosphates are easily reduced to heteropoly blue species and their reducibility can be rationalized by considering the local environments of the metal centers [11].

Metal centers in heteropolyanion frameworks occupy octahedral sites with one or two terminal oxygen atoms and represent as a mono nuclear coordination complexes, $\{MOL_5\}$ or $\{MO_2L_4\}$. The ideal local symmetry of a metal center with mono-oxo metal centers, is C_{4v}. Occupation of b_2 by one or two electrons have no significant effect on the metal-ligand bond orders. The lowest unoccupied molecular orbital (LUMO) of Keggin-type HPAs are symmetry-adapted sets of d_{xy}-like metal orbitals of E symmetry. In brief, the LUMO is a non-bonding metal-centered orbital. In contrast, *cis*-di-oxo metal center do not have "non-bonding" d orbital, but anti-bonding with respect to the terminal M=O bonds. Therefore, stable d^1-complexes are not available. Some examples of reducible and irreducible heteropolyanions are summarized in Table 1.3.

In general, type I heteropolyanions are reduced easily and reversibly to form mixed-valence species (heteropoly blues). However, type II heteropolyanions are hard to be reduced. For this reason, only type I heteropoly compounds, have attracted great attention as catalysts for the redox reactions.

There were lots of efforts to elucidate the redox mechanism of HPAs. Followings are reduction mechanisms of HPAs proposed by Mizuno et al. [12].

The reduction of $H_3PM_{12}O_{40}$ (M=Mo, W) by hydrogen proceeds in the following three steps:

$$xH_2\ (gas) + PM_{12}O_{40}^{3-}\ (surface) \leftrightarrow 2xH^+\ (bulk) + PM_{12}O_{40}^{(3+2x)-}(bulk) \quad (I)$$

$$2xH^+\ (bulk) + PM_{12}O_{40}^{(3+2x)-}(bulk) \leftrightarrow PM_{12}O_{40-x}^{3-}(bulk) + xH_2O\ (bulk) \quad (II)$$

$$xH_2O\ (bulk) \leftrightarrow xH_2O\ (gas) \quad (III)$$

First, a hydrogen is dissociated to protons and electrons: $H_2 \rightarrow 2H^+ + 2e^-$. Electrons are trapped by heteropolyanions, converting M(VI) ions into M(V) ions. In the second step, protons react with framework oxygen of heteropolyanion and are evolved as water. Further reduction brings about irreversibly reduced species. However, redox behaviors of HPAs can be affected by a number of variables (structures, compositions, or nature of metal ions) and redox behaviors of several HPAs still remain question marks.

Table 1.3

Examples of type I (reducible) and type II (irreducible) heteropolyanions [11]

Type I	Type II
$M_6O_{19}^{6-}$	$Mo_7O_{24}^{6-}$
$XM_{12}O_{40}^{n-}$	$ThMo_{12}O_{42}^{8-}$
$P_2M_{18}O_{62}^{6-}$	$NiW_6O_{24}H_6^{4-}$
$NaP_5W_{30}O_{110}^{14-}$	$H_2W_{12}O_{42}^{10-}$

1.3. Oxidation catalysis over HPAs

HPAs are known to suitable materials for the catalyst design because of their several unique properties. First, acid-base and redox properties can be easily tuned by changing the constituent elements such as counter-cations, central atoms, or addenda atoms. Second, their structures are well defined than conventional metal-oxides. This indicates that catalytic properties can be designed at atomic/molecular level and theoretical cluster modeling is feasible. Catalytic oxidations over HPAs have been extensively studied over the past few decades [1]. Especially, the mixed-addenda HPAs have attracted recent attention because of their variety in stoichiometric combination and outstanding catalytic performance in oxidation reactions.

Examples of oxidation catalysis over HPAs are summarized in Table 1.5. Liquid-phase reactions include electrocatalytic oxidation of NADH [13], Photocatalytic dehydrogenation of alcohols [14], and aerobic oxidation of alkyl aromatics [15]. Gas-phase reactions include oxidative dehydrogenation of alkanes [16,17] and selective oxidation of methanol [18].

It has been suggested that the aerobic oxidation of aromatics occurs via Mars-van Krevelen mechanism and the rate-determining step involves oxygen-transfer reaction from HPA to the intermediate radical cation [19]. In addition, a previous study [20] on the oxidative dehydrogenation of 2-propanol has demonstrated that the rate-determining step involves the reduction of HPA with β-hydrogen eliminated from the substrate and the intrinsic reaction rate is well correlated with the reducibility of HPA. In both cases, redox transitions of HPAs

were observed during the oxidation reactions and the rate-determining steps involved the reduction of HPAs. It is obvious that comprehensive understandings about redox properties of HPAs are of great importance in designing HPAs as oxidation catalysts.

Due to the importance of redox properties of HPAs in oxidation catalysis, comprehensive researches including quantum chemical molecular orbital study [21], hydrogen-temperature programmed reduction (TPR) measurements [22], and electrochemical analysis [23] have been conducted to examine the redox properties of HPAs. Among these, the most conventional experimental methods to probe redox properties of HPAs are electrochemical analysis and TPR measurements. Unfortunately, electrochemical analysis is strongly affected by a number of experimental conditions (pH, electrolyte, and electrode) and HPAs are not generally suitable for the dissociative adsorption of hydrogen in the TPR measurements. For this reason, only limited information on the redox properties of several HPAs is available. It is obvious that there is a need for the systematic studies about redox properties of HPAs using reliable experimental techniques.

Table 1.5

Oxidation catalysis over HPAs [10,24]

Reaction	Catalyst	Reaction conditions
Toluene and nitrobenzene oxidation with H_2O_2	$K_7P_2W_{15}Mo_2VO_{62}$	Acetonitrile as solvent, 298 K
Aerobic oxidation of aldehydes	$Cs_6H_2P_2W_{17}$	Dichloromethane as solvent,
to carboxylic acids	$(Co{\cdot}OH_2)O_{61}/SiO_2$	refluxing for 30 h under O_2
Aerobic oxidation of alkyl aromatics	$K_8H_2F_6NaVW_{17}O_{56}$	Biphasic reaction media
		pH =5 under O_2 (5 atm), 393 K
Electrocatalytic oxidation of	$P_2Mo_2W_{15}O_{61}^{10-}$	pH = 8
NADH to NAD^+	derivatives	
Photochemical degradation of thiothers	$(NH_4)_6P_2W_{18}O_{62}$	298 K, acetonitrile as solvent
		hν=550-10^3 W
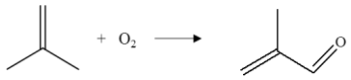	$PbFeBiPMo_{12}O_X$	673 K
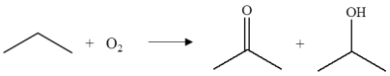	$H_7PW_9Fe_2NiO_{37}$	423 K
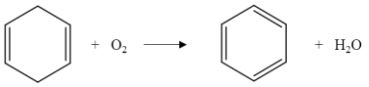	$H_5PMo_{10}V_2O_{40}$	343 K
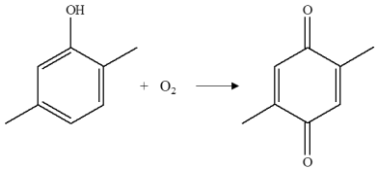	$H_5PMo_{10}V_2O_{40}$	333 K

Chapter 2. Experimental

2.1. Mo(VI)-substituted Wells-Dawson-type tungstophosphates

2.1.1. Preparation

$H_6P_2W_{18-x}Mo_xO_{62}$ (x=0, 3, 9, 15, 18) Wells-Dawson HPAs were prepared by "etherate method" according to the method reported in the previous literature [25] using $Na_2MoO_4{\cdot}2H_2O$, $Na_2HPO_4{\cdot}2H_2O$, $Na_2WO_4{\cdot}2H_2O$, diethyl ether, H_2SO_4, and HNO_3.

In case of $H_6P_2W_3Mo_{15}O_{62}$, 150 g of $Na_2MoO_4{\cdot}2H_2O$ and 40 g of $Na_2WO_4{\cdot}2H_2O$ were separately dissolved in 320 ml and 50 ml of distilled water, respectively. After complete dissolution, two solutions were mixed. Equivalent $Na_2HPO_4{\cdot}2H_2O$ aqueous solution were subsequently added to the mixed solution containing molybdenum and tungsten precursors. The mixed solution was treated with 80 ml of H_2SO_4 and it was refluxed for 8 h to form the heteropolyanion frameworks. After cooling the solution, it was extracted with diethyl ether. The "etherate" was dried in a convection oven to obtain a crude solid product. The yellow-colored solid was recrystallized from boiling water (small amounts of HNO_3 was added to avoid the formation of reduced species) to obtain the $H_6P_2W_3Mo_{15}O_{62}$. All the catalysts were thermally treated at 300 ^oC in a stream of nitrogen prior to characterization and catalytic reaction.

2.1.2. Characterization

2.1.2.1. Formation of HPA structure

Successful formation of $H_6P_2W_{18-x}Mo_xO_{62}$ (x=0, 3, 9, 15, 18) Wells-Dawson HPAs frameworks was confirmed by diffuse reflectance infrared Fourier transform (DRIFT) spectroscopy using a Nicolet 6700 (Nicolet) spectrometer. Chemical compositions were confirmed by inductively coupled plasma-atomic emission spectroscopy (ICP-AES) analyses using an ICPS-1000IV (Shimadzu) instrumentation.

2.1.2.2. Electrochemical analysis

Cyclic voltammograms of $H_6P_2W_{18-x}Mo_xO_{62}$ (x=0, 3, 9, 15, 18) Wells-Dawson HPAs were obtained by an electrochemical method in solution. Electrochemical measurements were performed using a conventional three-electrode system (Autolab 302N, Eco Chemie). Glassy carbon with diameter of 3.0 mm was used as a working electrode. Platinum rod and saturated calomel electrode (KCl saturated) were used as a counter electrode and a reference electrode, respectively. 0.5 M Na_2SO_4 aqueous solution was used as electrolyte. Each HPA sample (1 mM) was dissolved in electrolyte and cyclic voltammograms were acquired at a scan rate of 50 mV/s. Samples were purged for 20 min under He flow prior to electrochemical measurements.

2.1.2.3. UV-visible spectroscopy

UV-visible spectra of $H_6P_2W_{18-x}Mo_xO_{62}$ (x=0, 3, 9, 15, 18) Wells-Dawson HPAs were obtained using a Lambda-35 (Perkin-Elmer) spectrometer. 1 mM of sample solution was prepared for UV-visible spectroscopy measurement. The Kubelka-Munk function [26] was used to convert reflectance into equivalent absorption spectrum using $BaSO_4$ as a standard. Absorption edge energy was directly obtained from the $[F(R_\infty)\cdot h\nu]^{1/2}$ curve.

2.1.2.4. Scanning tunneling microscopy

Scanning tunneling microscopy (STM) and tunneling spectroscopy measurements were carried out in air using an Autoprobe CP (Thermomicroscope) instrument with mechanically formed Pt/Ir (90/10) tip. Samples for STM studies were prepared as followings. A certain amount of each HPA was dissolved in water to prepare 0.01 M aqueous HPA solution. A drop of sample solution was then deposited on freshly cleaved highly oriented pyrolytic graphite (HOPG) surface and it was allowed to dry in atmosphere for 1 h.

STM image was acquired in the constant current mode at a tunneling current of 1-2 nA and a sample bias of 100 mV. Tip was calibrated by imaging bare HOPG and measuring periodicity of bare HOPG. The image presented in this work was not filtered, and the reported preodicity and included angle are average values determined by performing 2-dimensional fast Fourier transform (2D FFT) analyses. For tunneling spectroscopy measurement, STM probe was

positioned above the HPA molecule of interest and the tunneling current was monitored while the bias voltage was ramped from -2.0 to +2.0 V. The voltage axis in the tunneling spectrum represents the potential applied to the sample relative to that of tip.

2.1.3. Catalytic test (oxidative dehydrogenation of ethanol)

Gas-phase oxidative dehydrogenation of ethanol over $H_6P_2W_{18-x}Mo_xO_{62}$ (x=0, 3, 6, 9, 15, 18) Wells-Dawson HPA catalysts was carried out in a continuous flow fixed-bed reactor at atmospheric pressure. Each catalyst (0.5 g) was charged into a tubular quartz reactor, and pretreated with a mixed stream of nitrogen (10 ml/min) and oxygen (10 ml/min) at 260 ^oC for 1 h. Ethanol (3.43×10^{-3} mol/h) was sufficiently vaporized by passing through the pre-heating zone and continuously fed into the reactor together with oxygen and nitrogen carrier. The feed composition (molar ratio) was fixed at ethanol (0.2): oxygen (1.0): nitrogen (1.0). The catalytic reaction was carried out at 240 ^oC for 5 h under steady-state conditions. The products were periodically sampled and analyzed with a gas chromatograph (HP 5890II), equipped with a capillary column (Supelco, VOCOL, 60 m × 1.5 μm × 0.25 mm). The conversion of ethanol and yield for acetaldehyde were calculated based on carbon balance.

2.2. V(V) and Nb(V)-substituted Wells-Dawson-type tungstophosphates

2.2.1. Preparation

α_2-$K_7P_2W_{17}M_1O_{62}$ (M=V and Nb) Wells-Dawson HPAs were prepared according to the method reported in the literature [27]. For the comparison, α-$K_6P_2W_{18}O_{62}$ and α_2-$K_6P_2W_{17}Mo_1O_{62}$ Wells-Dawson HPAs were also prepared. The catalysts were prepared by direct incorporation of transition metal into the framework of mono-lacunary heteropolyanions, α_2-$P_2W_{17}O_{61}^{10-}$. This method is proper than "etherate method" to prepare the structurally well-defined heteropolyanion because only uniform site (cap site) is available for metal-substitution in the mono-lacunary heteropolyanions.

2.2.1.1. Preparation of tungstophosphate (α-$K_6P_2W_{18}O_{62}$)

α-$K_6P_2W_{18}O_{62}$ Wells-Dawson HPA was prepared according to the method reported in the literature [28]. 300 g of $Na_2WO_4 \cdot 2H_2O$ dissolved in 350 ml deioinized water was acidified by addition of 50 ml of 4 M HCl aqueous solution. After complete dissolution, 250 ml of 4 M H_3PO_4 aqueous solution was slowly added. The pale yellow and limpid solution was refluxed for 24 h. The resulting solution was cooled and treated with excess amounts of KCl. The precipitate was filtered and air-dried to obtain the crude product. The crude product was dissolved in 650 ml deionized water and it was heated to 80 ^oC. After heating for

72 h, the resulting solution was cooled and placed in refrigerator at 4 ^{o}C overnight. After few days, yellow crystals of α-$K_6P_2W_{18}O_{62}$ Wells-Dawson HPA were collected and air-dried.

2.2.1.2. Preparation of mono-lacunary tungstophosphate (α_2-$K_{10}P_2W_{17}O_{61}$)

Wells-Dawson-type mono-laculary tungstophosphate (α_2-$K_{10}P_2W_{17}O_{61}$) was prepared according to the reported method [29]. 70 g of α-$K_6P_2W_{18}O_{62}\cdot 14H_2O$ was dissolved in 250 ml of deionized water. 1 M aqueous solution of $KHCO_3$ was added dropwise into α-$K_6P_2W_{18}O_{62}$ solution, and pH of the solution adjusted to 7.5. After 30 minutes stirring, white precipitate was collected and dried. The crude white crystal was then recrystallized from boiling water. The white crystal was washed with deionized water, ethanol, and diethyl ether. The resulting solid was dried at 50 ^{o}C overnight, and α_2-$K_{10}P_2W_{17}O_{61}\cdot 15H_2O$ was obtained.

2.2.1.3. Preparation of α_2-$K_7P_2W_{17}M_1O_{62}$ (M=V and Nb)

Typical procedures for the preparation of α_2-$K_7P_2W_{17}M_1O_{62}$ (M=V and Nb) Wells-Dawson HPAs are similar. For example, α_2-$K_7P_2W_{17}Nb_1O_{62}$ was prepared as followings. 0.360 g of $NbCl_5$ was dissolved in 150 ml of oxalic acid aqueous solution. 5 g of α_2-$K_{10}P_2W_{17}O_{61}$ was dissolved in 100 ml of boiling water. After complete dissolution, two solutions were then mixed. 35% HCl was added to the mixed solution until pH of the solution becomes <1.0. The mixed solution

was refluxed for 4 h. The resulting solution was cooled down to room temperature and treated with excess amounts of KCl. The white precipitates were collected and washed with deionized water several times to obtain the crude product. The crude product were recrystallized from boiling water to obtain α_2-$K_7P_2W_{17}Nb_1O_{62}$. α_2-$K_7P_2W_{17}V_1O_{62}$ Wells-Dawson HPA was prepared by similar method using $NaVO_3$ as a vanadium source. For the comparison, α_2-$K_6P_2W_{17}Mo_1O_{62}$ Wells-Dawson HPA was prepared similar method using $Na_2MoO_4 \cdot 2H_2O$ as a molybdenum source. All the catalysts were thermally treated at 300 ^oC in a stream of nitrogen prior to characterization and catalytic reaction.

2.2.2. Characterization

2.2.2.1. Formation of HPA structure

Successful formation of α_2-$K_7P_2W_{17}M_1O_{62}$ (M=V and Nb) Wells-Dawson HPAs were confirmed by diffuse reflectance infrared Fourier transform (DRIFT) spectroscopy using a Nicolet 6700 (Nicolet) spectrometer. Chemical compositions were confirmed by inductively coupled plasma-atomic emission spectroscopy (ICP-AES) analyses using an ICPS-1000IV (Shimadzu) instrumentation. ^{31}P NMR measurement (AVANCE 600, Bruker) was also performed using D_2O as a solvent, and 85% aqueous H_3PO_4 was used as an external standard.

2.2.2.2. Electrochemical analysis

Reduction potentials of α_2-$K_7P_2W_{17}M_1O_{62}$ (M=V and Nb) Wells-Dawson HPAs were measured by an electrochemical method in solution. 1 mM sample solutions were prepared by dissolving each catalyst in 0.5 M Na_2SO_4 solution. The sample solutions were then purged with He for 20 min, prior to the cyclic voltammetry measurements. Electrochemical experiments were performed using a Potentiostat/Galvanostat (Eco Chemie, Autolab 302N) instrument with a computer-controlled cyclic voltammetry system. The working electrode consisted of glassy carbon with an electrode diameter of 3.0 mm. A Pt rod and saturated calomel electrode (KCl saturated) were used as a counter electrode and

a reference electrode, respectively. The cyclic voltammograms were obtained at a scan rate of 25, 50, 100, 150, and 200 mV/s.

2.2.2.3. UV-visible spectroscopy

UV-visible spectroscopy of α_2-$K_7P_2W_{17}M_1O_{62}$ (M=V and Nb) Wells-Dawson HPAs was performed at room temperature using a Lambda-35 spectrometer (Perkin-Elmer). 1 mM aqueous solution of each catalyst was used for UV-visible spectroscopy measurement. The Kubelka-Munk function ($F(R_\infty)$) [26] was used to convert reflectance measurements into equivalent absorption spectra using the reflectance of $BaSO_4$ as a reference. Absorption edge energies was directly obtained from the $[F(R_\infty)\cdot hv]^{1/2}$ curves.

2.2.2.4. Scanning tunneling microscopy

0.01 M aqueous solutions of α_2-$K_7P_2W_{17}M_1O_{62}$ (M=V and Nb) Wells-Dawson HPAs were prepared. A drop of solution was deposited on HOPG surface and allowed to dry in air for 1 h. STM and tunneling spectroscopy were carried out in air using an Autoprobe CP (Thermomicroscope) instrument. Mechanically formed Pt/Ir (90/10) tips were used as a probe. STM tips were calibrated by imaging bare HOPG and confirming its standard periodicity (2.46 Å). Scanning was done in the constant current mode at a tunneling current of 1-2 nA and a sample bias of +100 mV. Lattice constants of unit cell represented average values determined by performing two-dimensional fast Fourier transform (2D FFT)

analyses.

To acquire the tunneling spectrum, sample bias voltage was ramped from -2.0 to +2.0 V with respect to the tip and the tunneling current was monitored. The voltage axis in the tunneling spectrum represented the potential applied to the sample relative to that of the tip. Current-voltage spectra were measured several times with three different tips to obtain more accurate and reproducible results, and to provide a basis for statistical analyses.

2.2.3. Catalytic test (oxidative dehydrogenation of benzylamine)

Gas-phase oxidative dehydrogenation of benzylamine over α_2-$K_7P_2W_{17}M_1O_{62}$ (M=V and Nb) was carried out in a fixed-bed reactor under atmospheric pressure. The reaction was also carried out over α-$K_6P_2W_{18}O_{62}$ and α_2-$K_6P_2W_{17}Mo_1O_{62}$ Wells-Dawson HPAs. 0.4 g of each HPA was charged into a tubular pyrex reactor and pretreated with a mixed stream of nitrogen (30 ml/min) and oxygen (10 ml/min) at 300 ^oC for 1 h. Benzylamine (0.5 ml/h) was sufficiently vaporized by passing through a preheating zone and it was continuously fed into the reactor together with nitrogen (30 ml/min) and oxygen (10 ml/min). Catalytic reaction was carried out at 300 ^oC for 5 h. Reaction products were periodically sampled and analyzed using a gas chromatograph (YL6100 GC, Younglin) equipped with a flame ionization detector. DB-5 (Agilent, 60 m × 0.32 mm) capillary column was used for product separation. The conversion of benzylamine and yield for products were calculated based on carbon balance.

2.3. Keggin-type heteropolytungstates with different central atom

2.3.1. Preparation

2.3.1.1. Preparation of α-$H_3PW_{12}O_{40}$ and α-$H_4SiW_{12}O_{40}$

Commercially available α-$H_3PW_{12}O_{40}$ (Kanto Chem.) and α-$H_4SiW_{12}O_{40}$ (Fluka) were purchased. The catalysts were thermally treated at 300 ^oC in a stream of nitrogen prior to characterization and catalytic reaction.

2.3.1.2. Preparation of α-$H_5BW_{12}O_{40}$

α-$K_5BW_{12}O_{40}$ was prepared by according to the method as described in the literature [30]. 100 g of $Na_2WO_4 \cdot 2H_2O$ was dissolved in the 100 ml of deionized water. 5 g of boric acid and 60 ml of 6 M HCl aqueous solution was added to the solution containing tungsten precursor. After complete dissolution, the solution was refluxed for 4 h and allowed to cool down. The solution was filtered and the filtrate was acidified by 6 M HCl aqueous solution until pH becomes 2.0. The solution was refluxed for 0.5 h and treated by 20 g of KCl. The white precipitate of α-$K_5BW_{12}O_{40}$ was obtained after the filteration, washing with ether, and recrystallization. Potassium salt was converted to acid form by etherate method or ion exchange process using ion exchange resin (Dowex HCR-W2 hydrogen form, Sigma-Aldrich). The catalyst was thermally treated at 300 ^oC in a stream

of nitrogen prior to characterization and catalytic reaction.

2.3.1.3. Preparation of α-$H_6CoW_{12}O_{40}$

α-$H_6CoW_{12}O_{40}$ was prepared to the methods as described in the literature [31]. 99 g of $Na_2WO_4 \cdot 2H_2O$ was dissolved in the 200 ml of deionized water. The solution was treated by 20 ml of acetic acid (The pH of solution was adjusted to 6.5~7.5.). 12.35 g of $Co(CH_3CO_2)_2 \cdot 4H_2O$ was dissolved in 65 ml of deionized water. The solution containing Co precursor was slowly added to the solution containing W precursor. The mixture solution was gently heated for 10 min and insoluble impurities were filtered. The filtrate was treated by excess amounts of KCl aqueous solution (85 g KCl in 150 ml deionized water) and stirred for an hour. The resulting solution was allowed to settle down for 24 h. The dark green precipitate (the mixture of dark blue and green crystals) was collected and treated by 200 ml of 2 M H_2SO_4. The solution turned into dark blue. The solution was concentrated by evaporation and green needles was filtered off. The solution was cooled in ice-bath. The dark blue crystals were collected after 24 h and allowed to dry in air. Potassium salt was converted to acid form by etherate method or ion exchange process using ion exchange resin (Dowex HCR-W2 hydrogen form, Sigma-Aldrich). The catalyst was thermally treated at 300 ^oC in a stream of nitrogen prior to characterization and catalytic reaction. The catalyst was thermally treated at 300 ^oC in a stream of nitrogen prior to characterization and catalytic reaction.

2.3.2. Characterization

2.3.2.1. Formation of HPA structure

Successful formation of α-$XW_{12}O_{40}^{n-}$ (X=Co^{2+}, B^{3+}, Si^{4+}, and P^{5+}) heteropolyanion frameworks was confirmed by diffuse reflectance infrared Fourier transform (DRIFT) spectroscopy using a Nicolet 6700 (Nicolet) spectrometer.

2.3.2.2. Electrochemical analysis

Cyclic voltammograms of α-$XW_{12}O_{40}^{n-}$ (X=Co^{2+}, B^{3+}, Si^{4+}, and P^{5+}) were measured by a conventional three-electrode system. Electrochemical measurements were carried out using a Potentiostat/Galvanostat (Eco Chemie, Autolab 302N) instrument. Glassy carbon electrode with diameter of 3.0 mm and platinum rod were used as a working electrode and a counter electrode, respectively. Saturated calomel electrode (KCl saturated) was used as a reference. Each HPA catalyst (1 mM) was dissolved in 0.5 M Na_2SO_4 aqueous solution and purged for 20 min under He flow (20 ml/min) prior to electrochemical measurement. Cyclic voltammograms were acquired at a scan rate of 25, 50, 100, 150, and 200 mV/s.

2.3.2.3. UV-visible spectroscopy

UV-visible spectra of α-$XW_{12}O_{40}^{n-}$ ($X=Co^{2+}$, B^{3+}, Si^{4+}, and P^{5+}) were obtained using a Lambda-35 (Perkin-Elmer) spectrometer. 1 mM of sample solutions were prepared for UV-visible spectroscopy measurements. The Kubelka-Munk function ($F(R_\infty)$) [26] was used to convert reflectance measurement into equivalent absorption spectrum.

2.3.2.4. Scanning tunneling microscopy

Scanning tunneling microscopy and tunneling spectroscopy studies for α-$XW_{12}O_{40}^{n-}$ ($X=Co^{2+}$, B^{3+}, Si^{4+}, and P^{5+}) were previously reported [32]. Data were taken from the previous literature [32]

2.4. Mo(VI)-substituted Wells-Dawson-type tungstoarsenates

2.4.1. Preparation

Wells-Dawson tungstoarsenate (α-$K_6As_2W_{18}O_{62}$) was prepared according to the modified method in the previous literature [33]. Molybdenum-substituted Wells-Dawson tungstoarsenates (α-$K_6As_2W_{18-x}Mo_xO_{62}$ (x=1-3)) were prepared by direct incorporation of molybdenum into mono-, di-, and tri-vacant lacunary species according to the methods described in the previous literature [34].

2.4.1.1. Preparation of α-$K_6As_2W_{18}O_{62}$

66 g of $Na_2WO_4 \cdot 2H_2O$ and excess amount of $Na_2HAsO_4 \cdot 7H_2O$ were separately dissolved in 90 ml of deionized water. 30 ml of 4 M HCl was added into the sodium tungstate solution. Sodium hydrogen arsenate solution was then introduced into the sodium tungstate solution. The pH of the mixed solution was adjusted to ca. 1.3 using HCl. The solution was subsequently refluxed at 80 ^oC for 4 h with vigorous stirring. The solution was then cooled down to room temperature and treated with 40 g of KCl. The resulting precipitate was filtered, washed with saturated KCl solution, and dried under atmospheric conditions.

2.4.1.2. Preparation of mono-lacunary tungstoarsenate (α_2-$K_{10}As_2W_{17}O_{61}$)

118.5 g (24 mmol) of α-$K_6As_2W_{18}O_{62}$ was dissolved in 360 ml of boiling water. 360 ml of 1 M $KHCO_3$ aqueous solution was added to the solution. The resulting solution was stirred for 40 min and filtered. The crude solid was recrystallized from 500 ml of boiling water to obtain α_2-$K_{10}As_2W_{17}O_{61}$.

2.4.1.3. Preparation of di-lacunary tungstoarsenate (α-$K_{11}HAs_2W_{16}O_{59}$)

39.5 g (8 mmol) of α-$K_6As_2W_{18}O_{62}$ was dissolved in 150 ml of water. 100 ml of 2 M tris(hydroxymethyl)aminomethane was quickly added to the solution. After stirring for 5 min, the resulting solution was treated with 150 ml of saturated KCl solution. The solution was further stirred for 10 min. The white precipitates were collected by filteration, washing with 50 ml of ethanol, and drying.

2.4.1.4. Preparation of tri-lacunary tungstoarsenate (α-$Na_{12}As_2W_{15}O_{56}$)

99 g (20 mmol) of α-$K_6As_2W_{18}O_{62}$ was dissolved in 250 ml water. 89 g of $NaClO_4$ was added to the solution. After 1 h, the solution was cooled down to 10 ^oC. The white precipitates ($KClO_4$) were removed by filteration. The pH of filtrate was adjusted to 9.0 using 1 M Na_2CO_3 aqueous solution and it was maintained for 1 h. The resulting precipitates were collected by filteration, washing with 100 ml ethanol, and drying.

2.4.1.5. Preparation of α-$K_6As_2W_{18-x}Mo_xO_{62}$ (x=1-3)

α-$K_6As_2W_{18-x}Mo_xO_{62}$ (x=1-3) were prepared by similar methods *via* direct incorporation of molybdenum into mono-, di-, and tri-vacant lacunary species according to the modified methods described in the previous literature [34]. 5 g of mono-, di-, or tri-lacunary tungstoarsenates were dissolved in 20 ml of boiling water. Equivalent $Na_2MoO_4 \cdot 2H_2O$ was added to the solution. After complete dissolution, the pH of solution was adjusted to < 1.0 using 35% HCl aqueous solution. After stirring for 1 h, the resulting solution was treated with 4 g of KCl. The yellow precipitates were collected by filteration and recrystallized in boiling water (pH < 2.0).

2.4.2. Characterization

2.4.2.1. Formation of HPA structure

Successful formation of α-$As_2W_{18-x}Mo_xO_{62}^{6-}$ (x=0-3) heteropolyanion frameworks was confirmed by diffuse reflectance infrared Fourier transform (DRIFT) spectroscopy using a Nicolet 6700 (Nicolet) spectrometer. Chemical compositions of the catalysts were confirmed by inductively coupled plasma-atomic emission spectroscopy (ICP-AES) analyses using an ICPS-1000IV (Shimadzu) instrumentation.

2.4.2.2. Electrochemical analysis

Cyclic voltammograms of α-$K_6As_2W_{18-x}Mo_xO_{62}$ (x=0-3) were obtained by an electrochemical method in solution. Electrochemical measurements were performed using a conventional three-electrode system (Autolab 302N, Eco Chemie). Glassy carbon with diameter of 3.0 mm was used as a working electrode. Platinum rod and saturated calomel electrode (KCl saturated) were used as a counter electrode and a reference electrode, respectively. 0.5 M Na_2SO_4 aqueous solution was used as electrolyte. Each HPA sample (1 mM) was dissolved in electrolyte and cyclic voltammograms were acquired at a scan rate of 10, 25, 50, 100, 150, and 200 mV/s. Samples were purged for 20 min under He flow (20 ml/min) prior to electrochemical measurements.

2.4.2.3. UV-visible spectroscopy

UV-visible spectra of α-$K_6As_2W_{18-x}Mo_xO_{62}$ (x=0-3) were obtained using a Lambda-35 (Perkin-Elmer) spectrometer. 1 mM of sample solution was prepared for UV-visible spectroscopy measurement. The Kubelka-Munk function [26] was used to convert reflectance into equivalent absorption spectrum using $BaSO_4$ as a standard. Absorption edge energy was directly obtained from the $[F(R_\infty)\cdot h\nu]^{1/2}$ curve.

2.4.2.4. Scanning tunneling microscopy

Each α-$K_8As_2W_{18-x}Mo_xO_{62}$ (x=0-3) catalyst was dissolved in deionized water (1 mM). Each HPA solution was physically deposited on the freshly cleaved HOPG. The sample was allowed to dry under atmosphere. STM investigations were performed using a XE-100E instrument (Park Systems) equipped with mechanically formed Pt/Ir (90/10) tip. The tip was calibrated by imaging bare HOPG surface and confirming its standard periodicity (2.46 Å) prior to imaging process. STM images of nano-structured HPAs were acquired in the constant-current mode. STM image presented in this work was not filtered, and dimension of unit cell was determined from two-dimensional fast Fourier transform (2-D FFT) analysis. Tunneling spectrum of each bright corrugation in the STM image was also measured. Current-voltage response was monitored as ramping the bias from -2.0 to +2.0 V. The voltage axis in the tunneling spectra represented the potential applied to the sample relative to that of the tip.

Tunneling spectra were measured several times with three different tips to provide more reproducible and accurate results, and to provide a basis for statistical analyses.

2.4.3. Catalytic test (oxidative dehydrogenation of benzyl alcohol)

Gas-phase oxidative dehydrogenation of benzyl alcohol was carried out over α-$K_6As_2W_{18-x}Mo_xO_{62}$ (x=0-3) catalysts. 0.5 g of HPA was charged into the tubular glass reactor and pretreated with a mixed stream of oxygen (10 ml/min) and nitrogen (20 ml/min) at 300 ^oC for 1 h. Vaporized benzyl alcohol (0.15 ml/h) was fed into the reactor together with a mixed stream of oxygen (10 ml/min) and nitrogen (20 ml/min). Catalytic reaction was performed at 300 ^oC for 5 h. Reaction products were periodically sampled and analyzed using a gas chromatograph (YL6100 GC, Younglin) equipped with a flame ionization detector. DB-5 (Agilent, 60 m × 0.32 mm) capillary column was used for product separation.

2.5. V(V) and Nb(V)-substituted Wells-Dawson-type tungstoarsenates

2.5.1. Preparation

2.5.1.1. Preparation of α_2-$K_7As_2W_{17}V_1O_{62}$

α_2-$K_7As_2W_{17}V_1O_{62}$ was prepared by similar methods *via* direct incorporation of vanadium into mono-lacunary species according to the modified method described in the previous literature [34]. 5 g of α_2-$K_{10}As_2W_{17}O_{61}$ was dissolved in 25 ml of boiling water. Equivalent $NaVO_3$ was added to the solution. After complete dissolution, the pH of solution was adjusted to < 1.0 using 35% HCl aqueous solution. After stirring for 1 h, the resulting solution was treated with 5 g of KCl. The orange precipitates were collected by filteration and recrystallized in boiling water. For the comparison, α-$K_6As_2W_{18}O_{62}$ and α_2-$K_6As_2W_{17}Mo_1O_{62}$ were also prepared

2.5.1.2. Preparation of α_2-$K_7As_2W_{17}Nb_1O_{62}$

α_2-$K_7As_2W_{17}Nb_1O_{62}$ was prepared by direct incorporation of niobium into mono-lacunary species. 0.110 g of $NbCl_5$ was dissolved in 30 ml of oxalic acid aqueous solution. 1.7 g of α_2-$K_{10}P_2W_{17}O_{61}$ was dissolved in 20 ml of boiling water. After complete dissolution, two solutions were then mixed. 35% HCl was added to mixed solution until pH of the solution becomes <1.0. The mixed

solution was refluxed for 4 h and it was cooled down to room temperature. The resulting solution was cooled and transfer to 300 ml of methanol. Then mixed solution was treated with excess amounts of KCl. The white precipitates were collected and washed with methanol to obtain α_2-$K_7P_2W_{17}Nb_1O_{62}$.

2.5.2. Characterization

2.5.2.1. Formation of HPA structure

Successful formation of α_2-$K_7As_2W_{17}M_1O_{62}$ (M=V and Nb) heteropolyanion frameworks was confirmed by diffuse reflectance infrared Fourier transform (DRIFT) spectroscopy using a Nicolet 6700 (Nicolet) spectrometer. Chemical compositions of the catalysts were confirmed by inductively coupled plasma-atomic emission spectroscopy (ICP-AES) analyses using an ICPS-1000IV (Shimadzu) instrumentation.

2.5.2.2. Electrochemical analysis

Cyclic voltammograms of α_2-$K_7As_2W_{17}M_1O_{62}$ (M=V and Nb) were obtained by an electrochemical method in solution. Electrochemical measurements were performed using a conventional three-electrode system (Autolab 302N, Eco Chemie). Glassy carbon with diameter of 3.0 mm was used as a working electrode. Platinum rod and saturated calomel electrode (KCl saturated) were used as a counter electrode and a reference electrode, respectively. 0.5 M Na_2SO_4 aqueous solution was used as electrolyte. Each HPA sample (1 mM) was dissolved in electrolyte and cyclic voltammograms were acquired at a scan rate of 10, 25, 50, 100, 150, and 200 mV/s. Samples were purged for 20 min under He flow (20 ml/min) prior to electrochemical measurements.

2.5.2.3. UV-visible spectroscopy

UV-visible spectra of α_2-$K_7As_2W_{17}M_1O_{62}$ (M=V and Nb) were obtained using a Lambda-35 (Perkin-Elmer) spectrometer. 1 mM of sample solution was prepared for UV-visible spectroscopy measurement. The Kubelka-Munk function [26] was used to convert reflectance into equivalent absorption spectrum using $BaSO_4$ as a standard. Absorption edge energy was directly obtained from the $[F(R_\infty)\cdot h\nu]^{1/2}$ curve.

2.5.3. Catalytic test (oxidative dehydrogenation of benzylamine)

Gas-phase oxidative dehydrogenation of benzyl amine was carried out over α_2-$K_7As_2W_{17}M_1O_{62}$ (M=V and Nb) catalysts. The reaction was also carried out over α-$K_6As_2W_{18}O_{62}$ and α_2-$K_6As_2W_{17}Mo_1O_{62}$ Wells-Dawson HPAs. 0.4 g of each HPA was charged into a tubular pyrex reactor and pretreated with a mixed stream of nitrogen (30 ml/min) and oxygen (10 ml/min) at 300 ^oC for 1 h. Benzylamine (0.5 ml/h) was sufficiently vaporized by passing through a preheating zone and it was continuously fed into the reactor together with nitrogen (30 ml/min) and oxygen (10 ml/min). Catalytic reaction was carried out at 300 ^oC for 5 h. Reaction products were periodically sampled and analyzed using a gas chromatograph (YL6100 GC, Younglin) equipped with a flame ionization detector. DB-5 (Agilent, 60 m × 0.32 mm) capillary column was used for product separation. The conversion of benzylamine and yield for products were calculated based on carbon balance.

Chapter 3. Results and Discussion

3.1. Mo(VI)-substituted Wells-Dawson-type tungstophosphates

3.1.1. Formation of HPA structure

Figure 3.1 shows the schematic diagram for the preparation procedures of $H_6P_2W_{18-x}Mo_xO_{62}$ (x=0, 3, 9, 15, 18) Wells-Dawson HPAs. Wells-Dawson heteropolyanion, $[X_2M_{18}O_{62}]^{6-}$ (X=central atom, M=addenda atom), is a polymeric oxoanion formed by condensation of more than two different oxoanions. The molecular structure of Wells-Dawson heteropolyanion could be considered as a combination of two defected Keggin units, $[XM_9O_{34}]^{9-}$; Two defected units were linked through six metal-oxygen-metal bonds. In this work, $H_6P_2W_{18-x}Mo_xO_{62}$ with x=0, 3, 9, 15, and 18 were denoted as P_2W_{18}, $P_2W_{15}Mo_3$, $P_2W_9Mo_9$, $P_2W_3Mo_{15}$, and P_2Mo_{18}, respectively.

Figure 3.2 shows the DRIFT spectra of $H_6P_2W_{18-x}Mo_xO_{62}$ (x=0, 3, 9, 15, 18) Wells-Dawson HPAs. Four characteristic bands attributed to P-O, M=O, and M-O-M (M=W or Mo) were clearly observed in the range of 700 - 1200 cm^{-1}. Detailed assignment of each band of $H_6P_2W_{18-x}Mo_xO_{62}$ (x=0, 3, 9, 15, 18) Wells-Dawson HPAs is summarized in Table 3.1. A single band for P-O stretching vibration was observed at 1067 - 1081 cm^{-1}. Three bands for $M=O_t$ (O_t: terminal oxygen), $M-O_c-M$ (O_c: corner-shared oxygen), and $M-O_e-M$ (O_e: edge-shared oxygen) stretching vibrations were observed at 959 - 984 cm^{-1}, 871 - 889 cm^{-1},

and 789 - 808 cm^{-1}, respectively. The characteristic bands of molybdenum-substituted Wells-Dawson tungstophosphates slightly shifted to lower wavenumber with increasing molybdenum content. Band positions were in good agreement with the previous results [25].

Chemical compositions of $H_6P_2W_{18-x}Mo_xO_{62}$ (x=0, 3, 9, 15, 18) Wells-Dawson HPAs was further confirmed by ICP-AES analyses. Chemical compositions of phosphorous, tungsten, and molybdenum in the $H_6P_2W_{18-x}Mo_xO_{62}$ (x=0, 3, 9, 15, 18) Wells-Dawson HPAs determined by ICP-AES analyses are summarized in Table 3.2. The measured P:W:Mo ratios in the $H_6P_2W_{18-x}Mo_xO_{62}$ were in good agreement with the theoretical values, indicating successful formation of heteropolyanion framework.

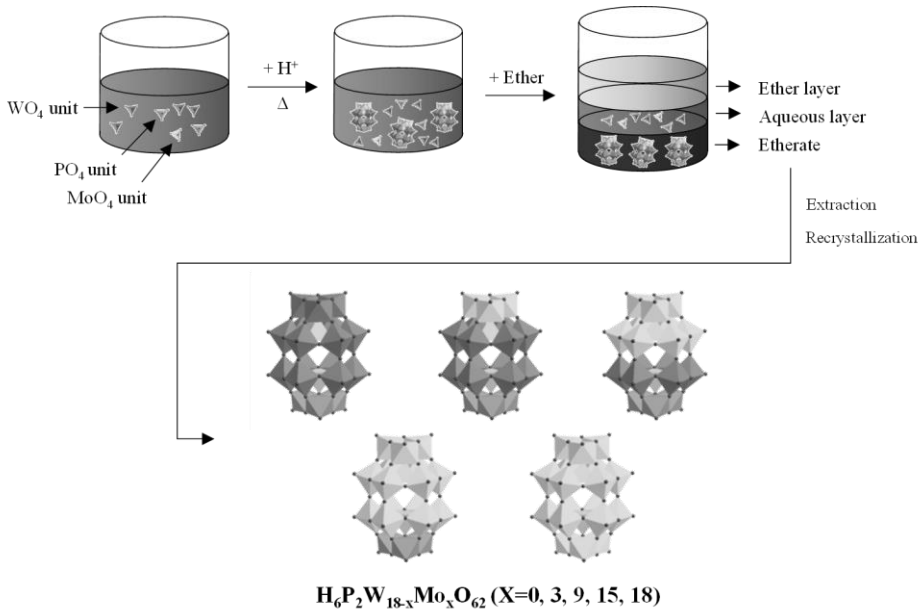

Fig. 3.1. Schematic diagram for the preparation procedures of $H_6P_2W_{18-x}Mo_xO_{62}$ (x=0, 3, 9, 15, 18) Wells-Dawson HPAs.

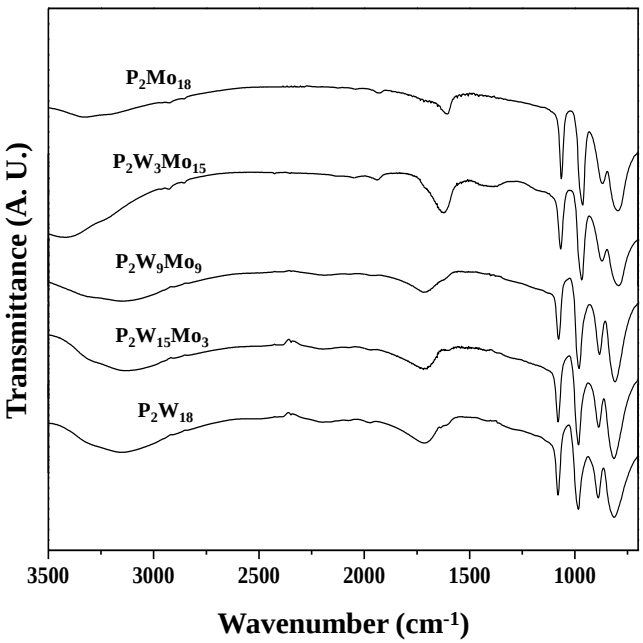

Fig. 3.2. DRIFT spectra of $H_6P_2W_{18-x}Mo_xO_{62}$ (x=0, 3, 9, 15, 18) Wells-Dawson HPAs.

Table 3.1

Detailed assignment of each band of $H_6P_2W_{18-x}Mo_xO_{62}$ (x=0, 3, 9, 15, 18) Wells-Dawson HPAs

Catalyst	Wavenumber (cm^{-1})			
	P-O	M=O_t	M-O_c-M	M-O_e-M
P_2Mo_{18}	1067	959	871	789
$P_2W_3Mo_{15}$	1068	963	873	792
$P_2W_9Mo_9$	1075	973	880	795
$P_2W_{15}Mo_3$	1078	982	886	804
P_2W_{18}	1081	984	889	808

*O_t: terminal oxygen, O_c: corner-shared oxygen, O_e: edge-shared oxygen

Table 3.2

Chemical compositions of phosphorous, tungsten, and molybdenum in the $H_6P_2W_{18-x}Mo_xO_{62}$ (x=0, 3, 9, 15, 18) Wells-Dawson HPAs

Catalyst	Ratio of P:W:Mo	
	Theoretical value	Measured value
P_2Mo_{18}	2.0 : 0.0 : 18.0	1.6 : 0.0 : 18.0
$P_2W_3Mo_{15}$	2.0 : 3.0 : 15.0	1.6 : 2.8 : 15.2
$P_2W_9Mo_9$	2.0 : 9.0 : 9.0	1.6 : 9.4 : 8.6
$P_2W_{15}Mo_3$	2.0 : 15.0 : 3.0	2.4 : 14.9 : 3.1
P_2W_{18}	2.0 : 18.0 : 0.0	1.8 : 18.0 : 0.0

3.1.2. Characterization

3.1.2.1. Cyclic voltammetry

Electrochemical measurement is one of the most conventional techniques to measure the redox properties of bulk HPAs. Figure 3.3 shows the cyclic voltammograms of $H_6P_2W_{18}O_{62}$ and $H_6P_2Mo_{18}O_{62}$ Wells-Dawson HPAs. They exhibited well-defined reversible and stepwise redox transitions during the electrochemical measurements. Overall shapes of cyclic voltammograms were retained at a scan rate up to 200 mV/s (maximum scan rate in this work, not shown here) and the peak currents increased monotonically. Each peak current was proportional to the square root of scan rate, indicating diffusion-controlled process which can be expressed by the Randles-Sevcik equation:

$$I_p = 2.69 \cdot 10^5 \cdot n^{3/2} \cdot D_o^{1/2} \cdot \nu^{1/2} \cdot C_o \cdot A \qquad (2)$$

where I_p, n, D_o, ν, C_o, and A denote peak current, number of electron involved in the redox event, diffusion coefficient, scan rate, concentrations, and electrode surface area, respectively.

Several tungsten-based redox transitions were observed in the cyclic voltammogram of $H_6P_2W_{18}O_{62}$, while $H_6P_2Mo_{18}O_{62}$ exhibited molybdenum-based redox transitions. Interestingly, molybdenum-substituted Wells-Dawson HPAs showed an additional molybdenum-based redox transition. This indicates that molybdenum centers were more electrochemically accessible and reducible

than tungsten centers in the heteropolyanion framework. Because the highest potential represented the reducibility of HPAs, the first electron reduction potential was taken as the representative reduction potential of HPAs [35]. First electron reduction potentials are summarized in Table 3.3. Reduction potential increased with increasing molybdenum-substitution.

The variation of reduction potential of HPAs could be understood by taking into account of their enthalpy, entropy, and electronic properties. However, enthalpy and entropy contributions on the redox properties could be neglected in the series of $H_6P_2W_{18-x}Mo_xO_{62}$ (x=0, 3, 9, 15, 18) Wells-Dawson HPAs because of their identical molecular size. Therefore, it is inferred that the difference in redox properties of $H_6P_2W_{18-x}Mo_xO_{62}$ (x=0, 3, 9, 15, 18) Wells-Dawson HPAs was mainly due to the difference in electronic structure caused by molybdenum-substitution.

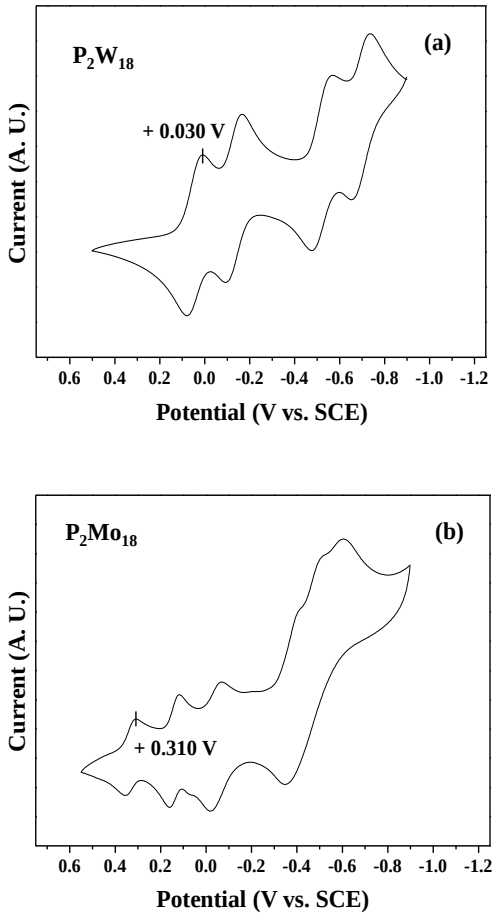

Fig. 3.3. Cyclic voltammograms of (a) $H_6P_2W_{18}O_{62}$ and (b) $H_6P_2Mo_{18}O_{62}$ Wells-Dawson HPAs.

3.1.2.2. UV-visible spectroscopy

UV-visible spectroscopy measurements were conducted to probe the electronic structure of $H_6P_2W_{18-x}Mo_xO_{62}$ (x=0, 3, 9, 15, 18) Wells-Dawson HPAs. It has been demonstrated that absorption edge energy determined by UV-visible spectroscopy was well correlated with catalytic activity and reducibility in the series of supported metal oxide clusters and metatungstate [36]. In the metal oxide, it is known that absorption edge energy is generally sensitive to average size of metal oxide domains. However, HPAs in solution are molecularly discrete clusters with nearly identical size and have an advantage for applying UV-visible spectroscopy. Therefore, UV-visible spectroscopy were performed as a simple diagnostic method for energy state and reducibility of HPAs.

Absorption edge energy (energy gap) was calculated from the following Tauc equation using Kubelka-Munk function ($F(R_\infty)$) to convert the reflectance to corresponding absorption spectrum.

$$(\alpha h\nu)^{1/2} = A\,(h\nu - E_g) \qquad (3)$$

where α, h, ν, A, and E_g denote absorption coefficient, Plank constant, scan rate, constant, and optical energy gap, respectively. Figure 3.4 shows the $[F(R_\infty)\cdot h\nu]^{1/2}$ curves of $H_6P_2W_{18-x}Mo_xO_{62}$ (x=0, 3, 9, 15, 18) Wells-Dawson HPAs. Absorption edge energies are summarized in Table 3.3. Absorption edge energy decreased with increasing molybdenum content. The trend of absorption edge energy is well consistent with that of reduction potential. Absorption edge energy represents the

energy required for electron promotion from the highest occupied molecular orbital (HOMO) to the lowest unoccupied molecular orbital (LUMO) [37]. By UV-visible irradiation, electrons are promoted from 2p-orbitals on the oxygens (the HOMO) to the low-lying high-energy states which comprise a combination of d-orbitals on the framework metal centers and 2p-orbitals on the framework oxygens (the LUMO). Thus, the energy gap between the HOMO and the LUMO decreased with increasing molybdenum content in the series of $H_6P_2W_{18-x}Mo_xO_{62}$. It is obvious that the HOMO is little affected by molybdenum-substitution because the HOMO mostly comprises 2p-orbitals on the framework oxygens. This indicates that the smaller absorption edge energy represents the lower energy level of the LUMO.

A previous density functional theory (DFT) study [38] about vanadium-substituted Wells-Dawson tungstophosphate showed that redox properties were closely related to energy state and composition of the LUMO, comprising an combination of d-orbitals on the metal centers and p-orbitals on the framework oxygens. In case of Wells-Dawson tungstophosphate, added electrons are generally delocalized over twelve tungsten centers at equatorial sites. In case of vanadium-substituted heteropolyanion, however, the energy state of metal centers at cap sites was stabilized by more reducible vanadium and the electrochemical reduction of vanadium centers at cap sites became available. The effect of molybdenum-substitution might be understood in a similar manner by considering the fact that molybdenum center is more reducible and contribution of molybdenum to the LUMO increases with increasing molybdenum content.

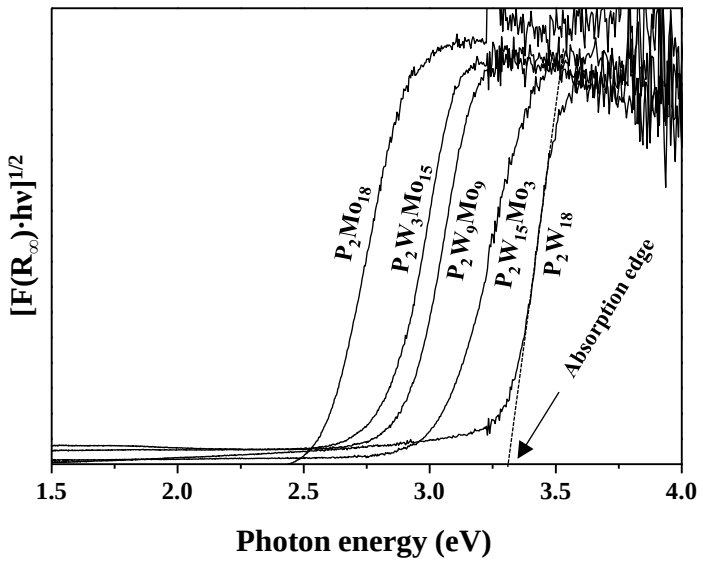

Fig. 3.4. $[F(R_\infty)\cdot hv]^{1/2}$ curves of $H_6P_2W_{18-x}Mo_xO_{62}$ (x=0, 3, 9, 15, 18) Wells-Dawson HPAs

3.1.2.3. Scanning tunneling microscopy

Scanning tunneling microscopy measurements were performed for the further investigation about the local electronic structure of $H_6P_2W_{18-x}Mo_xO_{62}$ (x=0, 3, 9, 15, 18) Wells-Dawson HPAs. In the STM measurements, STM image represents convolution of geometric and electronic structures rather than purely geometric structure of the specimen [39]. For adsorbate-substrate system, STM imaging would be more complex due to the presence of interaction between adsorbate and substrate. This indicates that STM image of adsorbate-covered surface may contain the electronic contributions of substrate and may not reflect the actual topography of surface. In this work, therefore, chemically inert graphite was employed as a substrate for HPA deposition and HPAs were physically deposited by solvent evaporation in order to minimize the interaction.

Figure 3.5 shows the STM images of $H_6P_2W_{18}O_{62}$ and $H_6P_2Mo_{18}O_{62}$ Wells-Dawson HPAs. Two-dimensional self-assembled HPA array was observed in the STM measurement. Each bright corrugation in the STM image represents individual heteropolyanion. The periodicity of $H_6P_2W_{18}O_{62}$ unit cell constructed on the basis of lattice constants determined from two-dimensional fast Fourier transform analysis (2-D FFT) was 11.2 Å × 14.4 Å with included angle of 57.2 °. The periodicity of $H_6P_2Mo_{18}O_{62}$ unit cell was found to 14.4 Å × 10.5 Å with included angle of 85.8 °. The dimensions of unit cells determined from STM images were in good agreement with the lattice constant determined by X-ray crystallography [2].

Figure 3.6 shows the typical current-voltage responses of $H_6P_2W_{18}O_{62}$ and

$H_6P_2Mo_{18}O_{62}$ Wells-Dawson HPAs taken at two different sites (bright corrugation and interstitial space between bright corrugations) in Figure 3.5. Current-voltage response at bare graphite was also measured for the comparison. It is noteworthy that each current-voltage response taken at interstitial space between bright corrugations was almost identical to that of bare graphite, indicating that two-dimensional HPA arrays shown in Figure 3.5 were monolayer. On the other hand, tunneling spectrum taken at bright corrugation showed a distinctive current-voltage response, referred to as negative differential resistance (NDR) phenomenon.

NDR phenomenon often explained by resonant tunneling model through a double barrier quantum well structure; tunneling electrons can pass through the molecular well without any attenuation when energy state of incident electron is in resonance with a virtual empty state in the molecular well (Figure 3.7) [40,41]. This resonance tunneling contains sequential electron transfer from negative potential to positive potential via framework oxygen and metal ions of heteropolyanion [42]. It is inferred that HPA molecule might serve as a quantum well, and resonant tunneling occurs when electrons pass through the frontier orbitals of HPA molecule [32].

The average values of NDR peak voltage were summarized in Table 3.3. It is interesting that NDR peak voltage appeared at less negative voltage with increasing the molybdenum content. This results is well consistent with the results of UV-visible spectroscopy, by considering the fact that absorption edge energy (energy gap between the HOMO and the LUMO) decreased with increasing the molybdenum content and NDR peak voltage reflects the frontier

orbital (the LUMO) of the HPAs.

Figure 3.8 shows the absorption edge energy and NDR peak voltage plotted as a function of reduction potential. It is inferred that the most stabilized energy level of the LUMO in the $H_6P_2Mo_{18}O_{62}$ (due to the contribution of reducible molybdenum metal centers) provided the electrochemically accessible metal centers and resulted in the highest reduction potential. The correlation also suggested that absorption edge energy and NDR peak voltage could be utilized as alternative correlating parameters for reduction potential of bulk HPAs in the series of $H_6P_2W_{18-x}Mo_xO_{62}$ (x=0, 3, 9, 15, 18) Wells-Dawson HPAs.

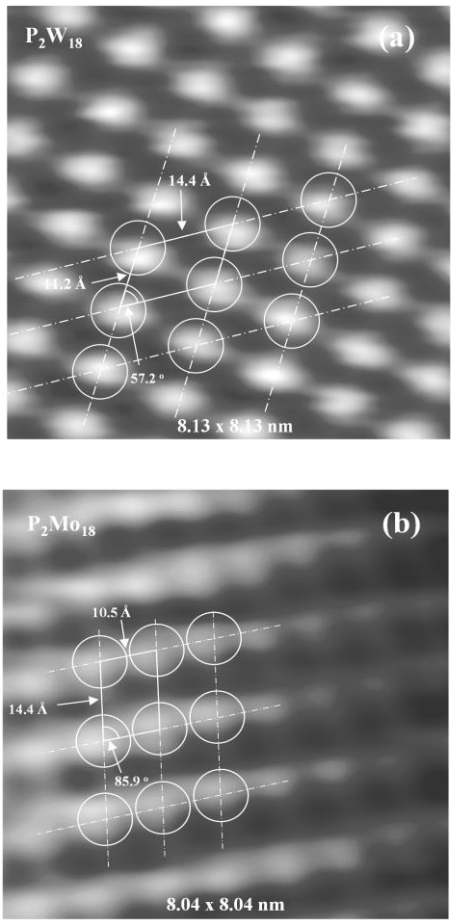

Fig. 3.5. STM images of (a) $H_6P_2W_{18}O_{62}$ and (b) $H_6P_2Mo_{18}O_{62}$ Wells-Dawson HPAs

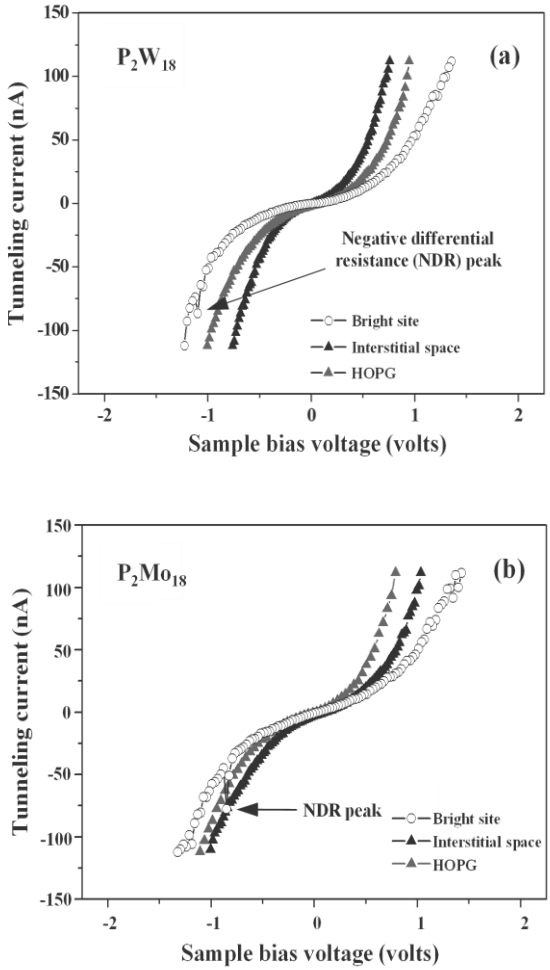

Fig. 3.6. Typical current-voltage responses of (a) $H_6P_2W_{18}O_{62}$ and (b) $H_6P_2Mo_{18}O_{62}$ Wells-Dawson HPAs taken at two different sites (bright corrugation and interstitial space between bright corrugations) in Figure 3.5.

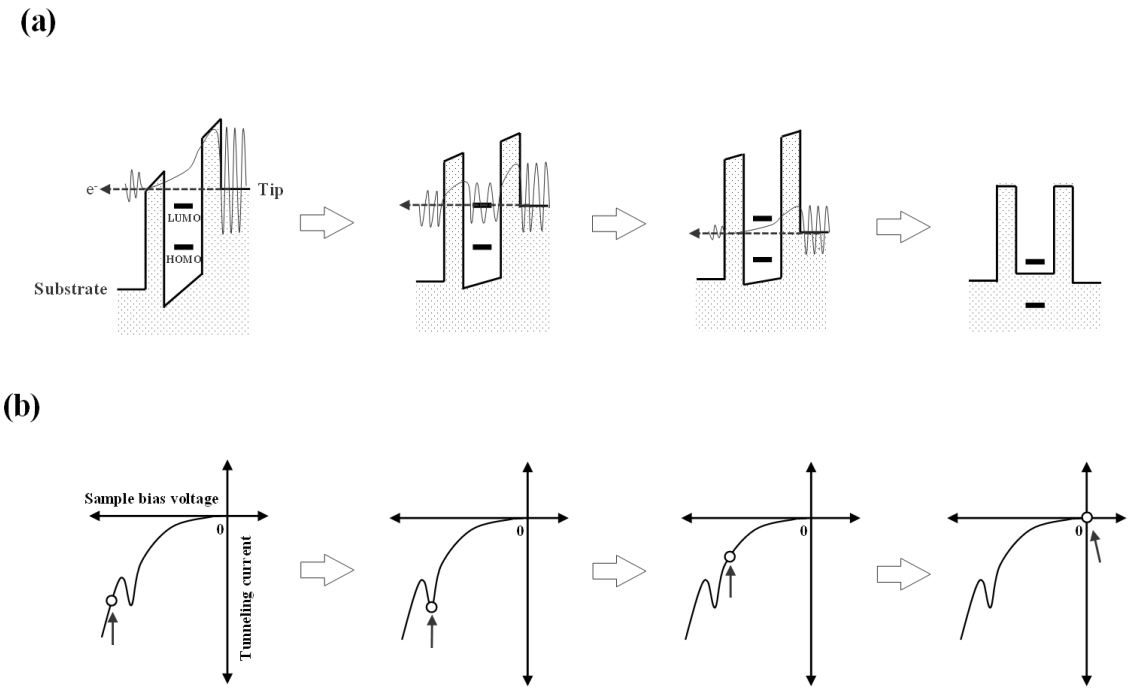

Fig. 3.7. Resonant tunneling model through a double barrier quantum well structure: (a) schematic representations and (b) corresponding spectra [41].

Table. 3.3.

First electron reduction potentials, absorption edge energies, and NDR peak voltages of $H_6P_2W_{18-x}Mo_xO_{62}$ (x=0, 3, 9, 15, 18) Wells-Dawson HPAs

Catalyst	1^{st} electron reduction potential (volts vs. SCE)	UV-visible absorption edge energy (eV)	NDR peak voltage (volts)
P_2Mo_{18}	+0.310	2.58	-0.85
$P_2W_3Mo_{15}$	+0.278	2.82	-0.94
$P_2W_9Mo_9$	+0.216	2.90	-1.00
$P_2W_{15}Mo_3$	+0.209	3.05	-1.08
P_2W_{18}	+0.030	3.31	-1.13

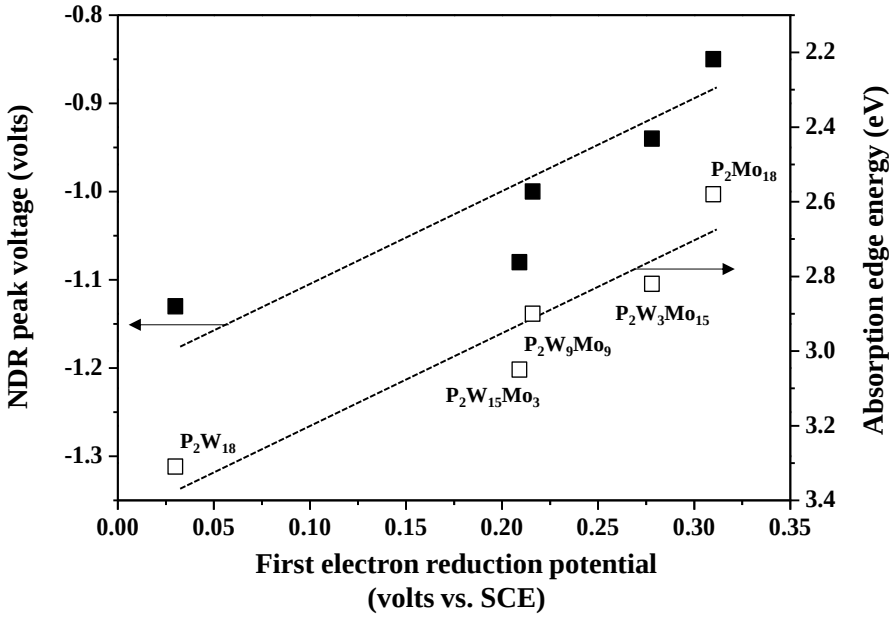

Fig. 3.8. Absorption edge energy and NDR peak voltage plotted as a function of reduction potential.

3.1.3. Catalytic test

Gas-phase oxidative dehydrogenation of ethanol to acetaldehyde was carried out as a model reaction to probe oxidation catalysis of $H_6P_2W_{18-x}Mo_xO_{62}$ (x=0, 3, 9, 15, 18) Wells-Dawson HPAs. Figure 3.9 shows the catalytic performance of $H_6P_2Mo_{18}O_{62}$ during a 6 h-reaction and yield for acetaldehyde plotted as a function of molybdenum content. The catalysts exhibited a stable catalytic performance during a 5 h-reaction. Acetaldehyde was mainly formed as an oxidation product, and ethylene/diethyl ether was produced as acid-catalyzed products. It is noteworthy that yield for acetaldehyde (oxidation product) increased with increasing molybdenum content. Among the tested catalysts, $H_6P_2Mo_{18}O_{62}$ which exhibited the highest reduction potential showed the best catalytic performance.

The previous extended Hűckel calculation for HPA [21] suggested that hydrogen was initially transferred to reducible metal center and rate-determining step involved direct interaction between hydrogen and reducible metal center during the oxidative dehydrogenation reaction. Furthermore, the adjacent metal center has a effect on the activation energy of reaction and may affect the pre-exponential factor of rate constant by contributing to the density of accessible electronic states (unoccupied orbitals). This result suggests that reducibility and composition of the metal centers in the HPA framework play an important role in the oxidative dehydrogenation reaction.

Similarly, a previous study [20] on the oxidative dehydrogenation of 2-propanol showed that the rate-determining step involved reduction of HPA with

β-hydrogen eliminated from the substrate and the intrinsic reaction rate was well correlated with the reducibility of HPA. When considering the fact that molybdenum center is easier to be reduced in the electrochemical measurement, it is inferred that molybdenum center provides efficient active sites for oxidative dehydrogenation by contributing to the density of accessible electronic states (unoccupied orbitals).

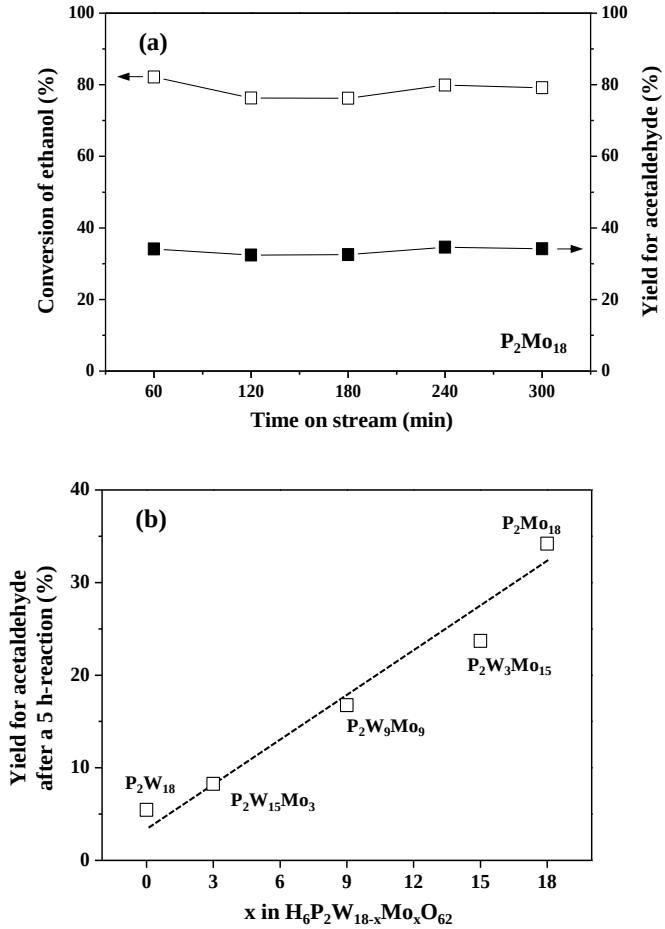

Fig. 3.9. (a) Catalytic performance of $H_6P_2Mo_{18}O_{62}$ during a 5 h-reaction and (b) yield for acetaldehyde after a 5 h-reaction plotted as a function of molybdenum content.

3.2. V(V) and Nb(V)-substituted Wells-Dawson-type tungstophosphates

3.2.1. Formation of HPA structure

Figure 3.10 shows the schematic diagram for the preparation procedures of α-$K_6P_2W_{18}O_{62}$, α_2-$K_6P_2W_{17}Mo_1O_{62}$, α_2-$K_7P_2W_{17}V_1O_{62}$, and α_2-$K_7P_2W_{17}Nb_1O_{62}$ Wells-Dawson HPAs. α_2-$K_7P_2W_{17}V_1O_{62}$ and α_2-$K_7P_2W_{17}Nb_1O_{62}$ were prepared to elucidate the effect of group 5-metal-substitution on the redox properties and the electronic structure. α-$K_6P_2W_{18}O_{62}$ and α_2-$K_6P_2W_{17}Mo_1O_{62}$ were also prepared for the comparison. In this work, mono-transition metal-substituted Wells-Dawson HPAs were prepared by direct incorporation of transition metal into the mono-lacunary α_2-$K_{10}P_2W_{17}O_{61}^{10-}$. Removal of a cap WO_6 unit in the α-$K_6P_2W_{18}O_{62}$ by pH control yields mono-lacunary heteropolyanion, α_2-$P_2W_{17}O_{61}^{10-}$. Mono-lacunary heteropolyanion generally acts as a tetradentate ligand for lanthanides and actinides, and as a pentadentate ligand for transition metals [43]. As a results, a tungsten center could be selectively replaced by a transition metal. This preparation method is very useful to yield the uniformly-substituted Wells-Dawson structure, rather than "etherate method (randomly-substituted structure)".

Figure 3.11 shows the DRIFT spectra of α-$K_6P_2W_{18}O_{62}$, α_2-$K_6P_2W_{17}Mo_1O_{62}$, α_2-$K_7P_2W_{17}V_1O_{62}$, and α_2-$K_7P_2W_{17}Nb_1O_{62}$ Wells-Dawson HPAs. Successful formations of the heteropolyanions can be confirmed by four characteristic bands in the range of 1200-700 cm^{-1} which represent P-O, M=O_t, inter-octahedral M-O_c-M, and intra-octahedral M-O_e-M bonds (M=metal).

Detailed assignment of each characteristic band was summarized in Table 3.4. Four characteristic bands were clearly observed in DRIFT spectra, indicating the successful formation of the heteropolyanions.

The HPAs were also confirmed by ^{31}P NMR analyses. Figure 3.12 shows the ^{31}P NMR spectra of α-$K_6P_2W_{18}O_{62}$, α_2-$K_6P_2W_{17}Mo_1O_{62}$, α_2-$K_7P_2W_{17}V_1O_{62}$, and α_2-$K_7P_2W_{17}Nb_1O_{62}$ Wells-Dawson HPAs dissolved in D_2O. In ^{31}P NMR spectra, α-$K_6P_2W_{18}O_{62}$ HPAs showed a single peak at -12.6 ppm which arise from two identical central phosphorous heteroatoms. However, other HPAs showed two different peaks. Two different peaks arise from two inequivalent central phosphorous heteroatoms due to the metal-substitution. In niobium-substituted Wells-Dawson tungstophosphate, for example, a peak at -10.8 ppm corresponds to a phosphorous atom near the niobium center. Another peak at -13.1 ppm corresponds to a phosphorous atom far from the niobium center. Any other noticeable peaks were not observed except small peaks of impurity in the ^{31}P NMR spectra.

Chemical compositions of phosphorous, tungsten, and substituted-metal in the HPAs were further confirmed by ICP-AES analyses. Chemical compositions of phosphorous, tungsten, and substituted-metal in the α-$K_6P_2W_{18}O_{62}$, α_2-$K_6P_2W_{17}Mo_1O_{62}$, α_2-$K_7P_2W_{17}V_1O_{62}$, and α_2-$K_7P_2W_{17}Nb_1O_{62}$ Wells-Dawson HPAs were summarized in table 3.5. The molar ratios of P:W:M were in good agreement with the theoretical values, suggesting the successful formation of HPA structure.

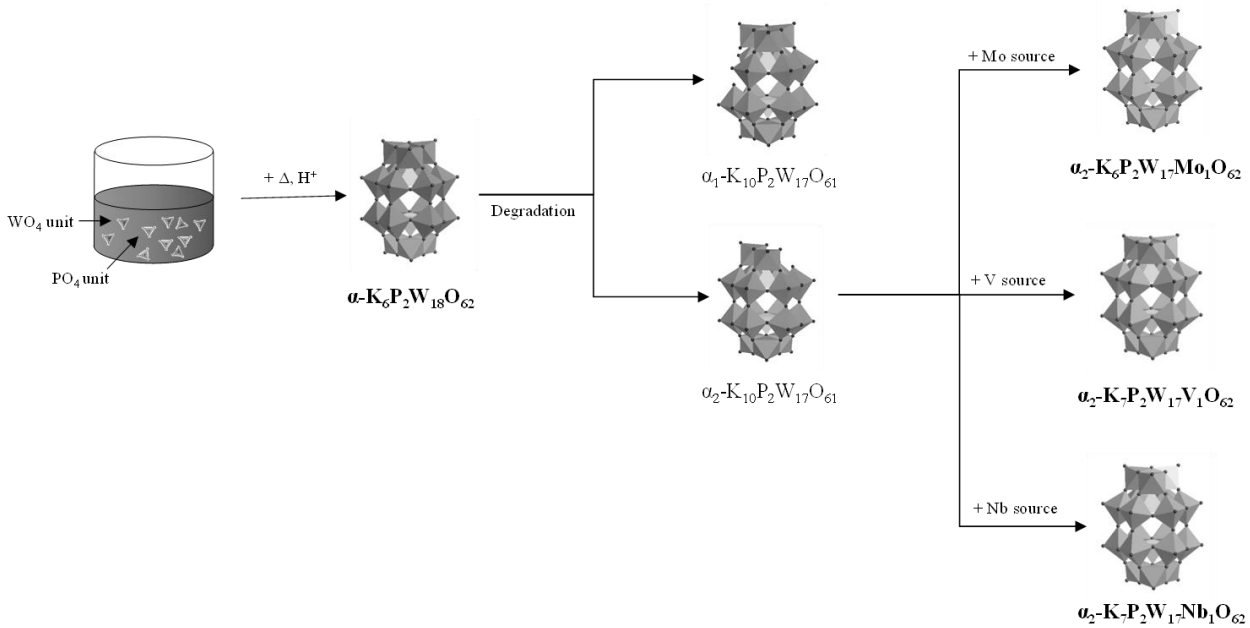

Fig. 3.10. Schematic diagram for the preparation procedures of α-$K_6P_2W_{18}O_{62}$, α_2-$K_6P_2W_{17}Mo_1O_{62}$, α_2-$K_7P_2W_{17}V_1O_{62}$, and α_2-$K_7P_2W_{17}Nb_1O_{62}$ Wells-Dawson HPAs.

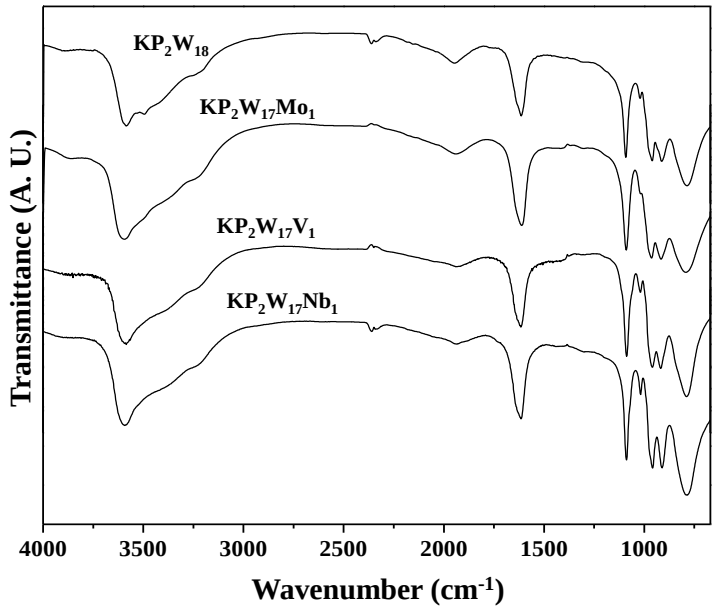

Fig. 3.11. DRIFT spectra of α-$K_6P_2W_{18}O_{62}$, α_2-$K_6P_2W_{17}Mo_1O_{62}$, α_2-$K_7P_2W_{17}V_1O_{62}$, and α_2-$K_7P_2W_{17}Nb_1O_{62}$ Wells-Dawson HPAs.

Table 3.4.

Detailed assignment of each characteristic band

Catalyst	Wavenumber (cm^{-1})			
	P-O	$M=O_t$	$M-O_c-M$	$M-O_e-M$
KP_2W_{18}	1092	962	915	787
$KP_2W_{17}Mo_1$	1089	961	916	786
$KP_2W_{17}V_1$	1091	958	909	790
$KP_2W_{17}Nb_1$	1089	960	913	785

*O_t: terminal oxygen, O_c: corner-shared oxygen, O_e: edge-shared oxygen

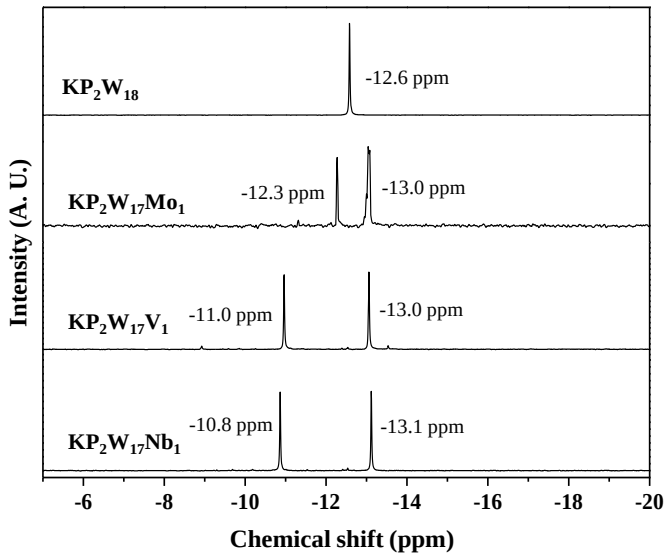

Fig. 3.12. ^{31}P NMR spectra of α-$K_6P_2W_{18}O_{62}$, α_2-$K_6P_2W_{17}Mo_1O_{62}$, α_2-$K_7P_2W_{17}V_1O_{62}$, and α_2-$K_7P_2W_{17}Nb_1O_{62}$ Wells-Dawson HPAs dissolved in D_2O.

Table 3.5.

Chemical compositions of phosphorous, tungsten, and substituted-metal (M) in the α-$K_6P_2W_{18}O_{62}$, α_2-$K_6P_2W_{17}Mo_1O_{62}$, α_2-$K_7P_2W_{17}V_1O_{62}$, and α_2-$K_7P_2W_{17}Nb_1O_{62}$ Wells-Dawson HPAs

Catalyst	Ratio of P:W:M	
	Theoretical value	Measured value
KP_2W_{18}	2.0 : 18.0 : 0	2.0 : 18.0 : 0
$KP_2W_{17}Mo_1$	2.0 : 17.0 : 1.0	1.9 : 17.0 : 1.0
$KP_2W_{17}V_1$	2.0 : 17.0 : 1.0	1.9 : 17.0 : 1.1
$KP_2W_{17}Nb_1$	2.0 : 17.0 : 1.0	2.2 : 17.0 : 1.1

3.2.2. Characterization

3.2.2.1. Cyclic voltammetry

Figure 3.13 shows the cyclic voltammograms of α-$K_6P_2W_{18}O_{62}$, α_2-$K_6P_2W_{17}Mo_1O_{62}$, α_2-$K_7P_2W_{17}V_1O_{62}$, and α_2-$K_7P_2W_{17}Nb_1O_{62}$ Wells-Dawson HPAs. Four tungsten-based redox transitions were observed in the cyclic voltammogram of α-$K_6P_2W_{18}O_{62}$. In case of molybdenum- and vanadium-substituted Wells-Dawson tungstophosphates showed an additional molybdenum- and vanadium-based redox transitions, respectively. However, niobium-substituted Wells-Dawson tungstophosphates showed significantly shifted redox couple. This indicates vanadium or molybdenum center in the heteropolyanion framework was more electrochemically accessible and easier to be reduced than tungsten centers. Otherwise, the niobium-substitution has negative effect to the reducibility of Wells-Dawson tungstophosphates. The first electron reduction potentials are summarized in Table 3.6. Reduction potential increased in the order of α_2-$K_7P_2W_{17}Nb_1O_{62}$ < α-$K_6P_2W_{18}O_{62}$ < α_2-$K_6P_2W_{17}Mo_1O_{62}$ < α_2-$K_7P_2W_{17}V_1O_{62}$.

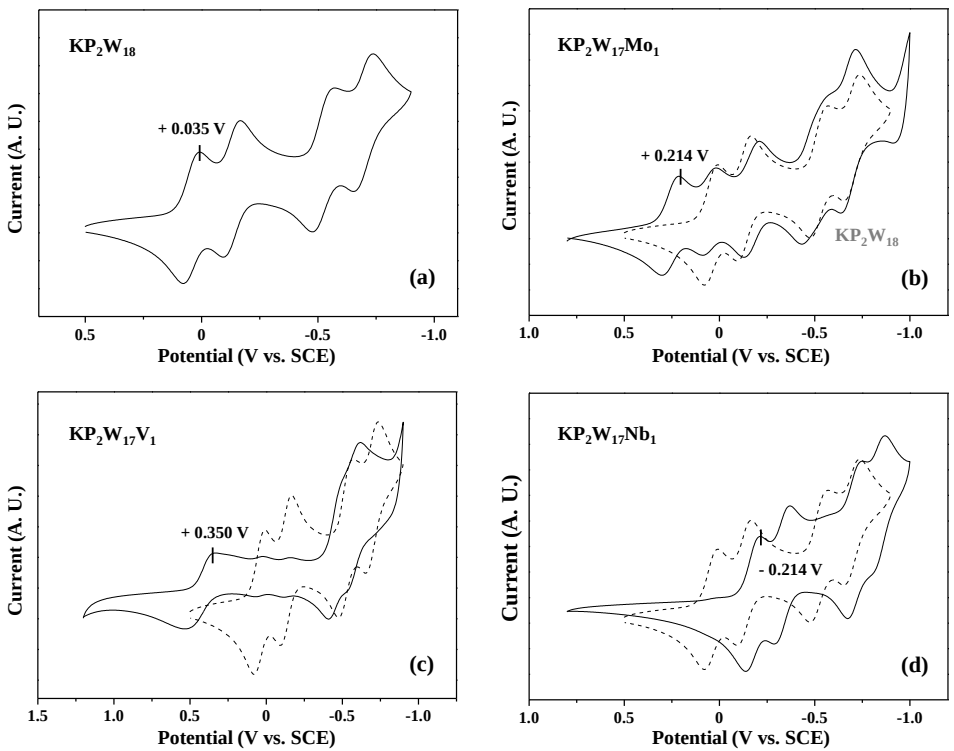

Fig. 3.13. Cyclic voltammograms of (a) α-$K_6P_2W_{18}O_{62}$, (b) α_2-$K_6P_2W_{17}Mo_1O_{62}$, (c) α_2-$K_7P_2W_{17}V_1O_{62}$, and (d) α_2-$K_7P_2W_{17}Nb_1O_{62}$ Wells-Dawson HPAs.

3.2.2.2. UV-visible spectroscopy

UV-visible spectroscopy measurements were conducted to probe the bulk electronic structures of α-$K_6P_2W_{18}O_{62}$, α_2-$K_6P_2W_{17}Mo_1O_{62}$, α_2-$K_7P_2W_{17}V_1O_{62}$, and α_2-$K_7P_2W_{17}Nb_1O_{62}$ Wells-Dawson HPAs. Figure 3.14 shows the $[F(R_\infty)\cdot h\nu]^{1/2}$ curves of α-$K_6P_2W_{18}O_{62}$, α_2-$K_6P_2W_{17}Mo_1O_{62}$, α_2-$K_7P_2W_{17}V_1O_{62}$, and α_2-$K_7P_2W_{17}Nb_1O_{62}$ Wells-Dawson HPAs. UV-visible absorption edge energies are summarized in Table 3.6. Absorption edge energy decreased in the order of α_2-$K_7P_2W_{17}Nb_1O_{62}$ > α-$K_6P_2W_{18}O_{62}$ > α_2-$K_6P_2W_{17}Mo_1O_{62}$ > α_2-$K_7P_2W_{17}V_1O_{62}$. As mentioned above, absorption edge energy determined from the linear fit of $[F(R_\infty)\cdot h\nu]^{1/2}$ represents the energy required for electron promotion from the HOMO to the LUMO [37]. Thus, the energy gap between the HOMO and the LUMO decreased in the order of α_2-$K_7P_2W_{17}Nb_1O_{62}$ > α-$K_6P_2W_{18}O_{62}$ > α_2-$K_6P_2W_{17}Mo_1O_{62}$ > α_2-$K_7P_2W_{17}V_1O_{62}$. It could be inferred that α_2-$K_7P_2W_{17}V_1O_{62}$ with the smallest absorption edge energy has the lowest energy level of the LUMO, because the HOMO is little perturbed by metal-substitution in the series of α-$K_6P_2W_{18}O_{62}$, α_2-$K_6P_2W_{17}Mo_1O_{62}$, α_2-$K_7P_2W_{17}V_1O_{62}$, and α_2-$K_7P_2W_{17}Nb_1O_{62}$ Wells-Dawson HPAs,.

A previous density functional theory (DFT) study [44] about the tri-substituted Keggin-type tungstosilicates showed the similar results. Theoretically calculated energy gap between the HOMO and the LUMO decreased when molybdenum/vanadium is substituted but increased when niobium is substituted in the Keggin-type tungstosilicates. They also reported that the relative energy and composition of the LUMO was well correlated with the electron affinity of

metal center. The niobium center shows the greater predisposition than vanadium center to lose its electrons (hard to be reduced). Otherwise, vanadium-center largely contributes and stabilizes the energy level of the LUMO and an additional electron is delocalized over the three vanadium centers in the mono-reduced vanadium-substituted Keggin-type tungstosilicate. The differences in reduction potentials and absorption edge energies could be understood in a similar manner. For Wells-Dawson tungstophosphate, the energy of metal centers at cap sites was stabilized by more reducible vanadium and the electrochemical reduction of vanadium centers at cap sites became available. Therefore, electrochemically added electrons are preferentially localized on the vanadium center. In case of α_2-$K_7P_2W_{17}Nb_1O_{62}$, it could be inferred that niobium center could not stabilize but elevate the energy level of metal centers. Therefore, reduction of metal centers at cap site was not available and showed negatively-shifted reduction potential The difference in absorption edge energy could be understood by considering the differences in electron affinity of metal center, contribution of metal center to the LUMO, and symmetry of HPA structure (the symmetries of HPA structures are almost identical as a α_2-type isomer). It is noteworthy that α_2-$K_7P_2W_{17}V_1O_{62}$ with the smallest band gap showed the highest reduction potential.

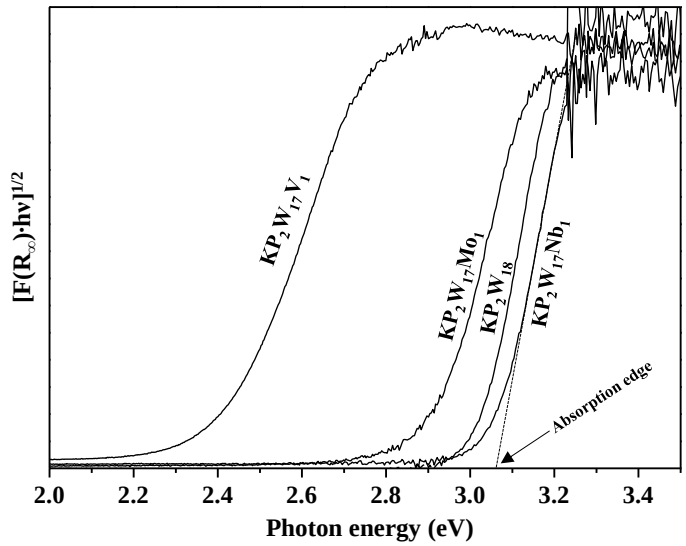

Fig. 3.14. $[F(R_\infty)\cdot h\nu]^{1/2}$ curves of α-$K_6P_2W_{18}O_{62}$, α_2-$K_6P_2W_{17}Mo_1O_{62}$, α_2-$K_7P_2W_{17}V_1O_{62}$, and α_2-$K_7P_2W_{17}Nb_1O_{62}$ Wells-Dawson HPAs.

3.2.2.3. Scanning tunneling microscopy

Figure 3.15 shows the STM images of α_2-$K_7P_2W_{17}V_1O_{62}$ and α_2-$K_7P_2W_{17}Nb_1O_{62}$ Wells-Dawson HPAs deposited on graphite surface. Each bright corrugation represents individual heteropolyanion. STM images clearly showed the formation of self-assembled and well-ordered HPA arrays on HOPG surface. The periodicity and included angle of unit cell constructed on the basis of lattice constants determined from two-dimensional fast Fourier transformation (2D FFT) are also shown in Figure 3.15. The periodicity of α_2-$K_7P_2W_{17}V_1O_{62}$ unit cell was found to 0.85 Å × 13.1 Å with included angle of 83.2 °. The periodicity of α_2-$K_7P_2W_{17}Nb_1O_{62}$ unit cell was found to 11.1 Å × 11.5 Å with included angle of 61.0 °. Periodicity of unit cell was well consistent with lattice constants of Wells-Dawson HPAs determined by X-ray crystallography [2].

Tunneling spectroscopy was conducted in order to elucidate the local surface electronic structures of α-$K_6P_2W_{18}O_{62}$, α_2-$K_6P_2W_{17}Mo_1O_{62}$, α_2-$K_7P_2W_{17}V_1O_{62}$, and α_2-$K_7P_2W_{17}Nb_1O_{62}$ Wells-Dawson HPAs. Figure 3.16 shows the typical tunneling spectra of α_2-$K_7P_2W_{17}V_1O_{62}$ and α_2-$K_7P_2W_{17}Nb_1O_{62}$ Wells-Dawson HPAs catalyst taken at two different sites (bright corrugation and interstitial space between bright corrugations) in Figure 3.15. The tunneling spectra taken at bright corrugation showed a distinctive current-voltage behavior referred to as negative differential resistance (NDR), which was known to be a characteristic of HPAs. On the other hands, tunneling spectra taken at interstitial space between bright corrugations showed almost the same current-voltage behavior with that of bare HOPG. This indicates that the self-assembled and well-ordered HPA arrays shown in Figure 3.15 are a monolayer.

The average value of NDR peak voltage was taken as the representative NDR peak voltage. The average values of NDR peak voltage were summarized in Table 3.6. It is interesting that the trend of NDR peak voltage is well consistent with that of UV-visible spectroscopy. As mentioned, it can be inferred that less negative NDR voltage of HPA catalysts corresponds to lower energy state of the LUMO. Because energy gap only depends on energy state of LUMO in the series of α-$K_6P_2W_{18}O_{62}$, α_2-$K_6P_2W_{17}Mo_1O_{62}$, α_2-$K_7P_2W_{17}V_1O_{62}$, and α_2-$K_7P_2W_{17}Nb_1O_{62}$ Wells-Dawson HPAs, smaller absorption edge energy corresponds to lower energy state of the LUMO, leading to less negative NDR peak voltage.

Figure 3.17 shows the absorption edge energy and NDR peak voltage plotted as a function of reduction potential. The correlations suggested that reduction potential could be estimated from the electronic structure and absorption edge energy/NDR peak voltage could be utilized as alternative correlating parameters for reduction potential of bulk HPAs in the series of α-$K_6P_2W_{18}O_{62}$, α_2-$K_6P_2W_{17}Mo_1O_{62}$, α_2-$K_7P_2W_{17}V_1O_{62}$, and α_2-$K_7P_2W_{17}Nb_1O_{62}$ Wells-Dawson HPAs. Among the tested, vanadium center is the most effective to enhance the reducibility of heteropolyanion by the stabilization of energy state of the LUMO.

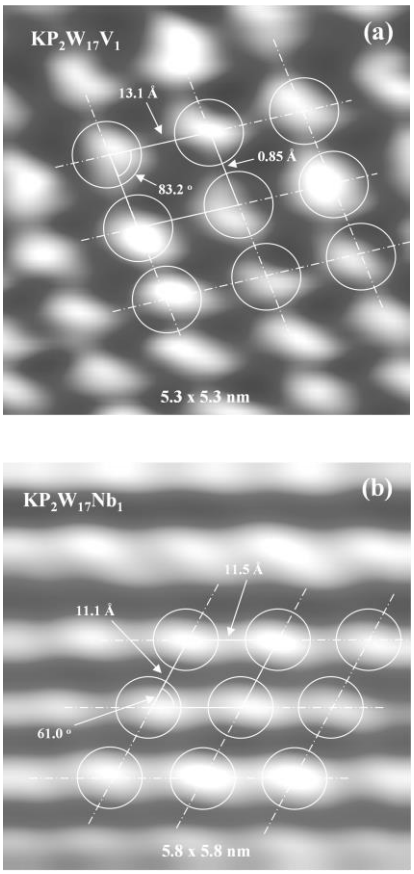

Fig. 3.15. STM images of (a) α_2-$K_7P_2W_{17}V_1O_{62}$ and (b) α_2-$K_7P_2W_{17}Nb_1O_{62}$ Wells-Dawson HPAs.

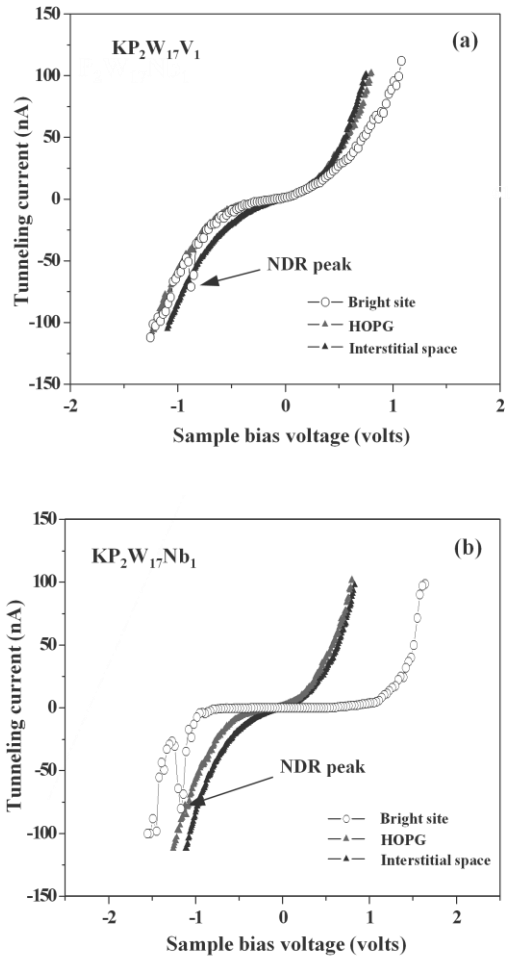

Fig. 3.16. Typical tunneling spectra of (a) α_2-$K_7P_2W_{17}V_1O_{62}$ and (b) α_2-$K_7P_2W_{17}Nb_1O_{62}$ Wells-Dawson HPAs catalyst taken at two different sites (bright corrugation and interstitial space between bright corrugations) in Figure 3.15.

Table. 3.6.

First electron reduction potentials, absorption edge energies, and NDR peak voltages of α-$K_6P_2W_{18}O_{62}$, α_2-$K_6P_2W_{17}Mo_1O_{62}$, α_2-$K_7P_2W_{17}V_1O_{62}$, and α_2-$K_7P_2W_{17}Nb_1O_{62}$ Wells-Dawson HPAs

Catalyst	1st electron reduction potential (volts vs. SCE)	UV-visible absorption edge energy (eV)	NDR peak voltage (volts)
KP_2W_{18}	+0.035	3.01	-1.00
$KP_2W_{17}Mo_1$	+0.214	2.91	-0.98
$KP_2W_{17}V_1$	+0.350	2.40	-0.88
$KP_2W_{17}Nb_1$	-0.214	3.06	-1.02

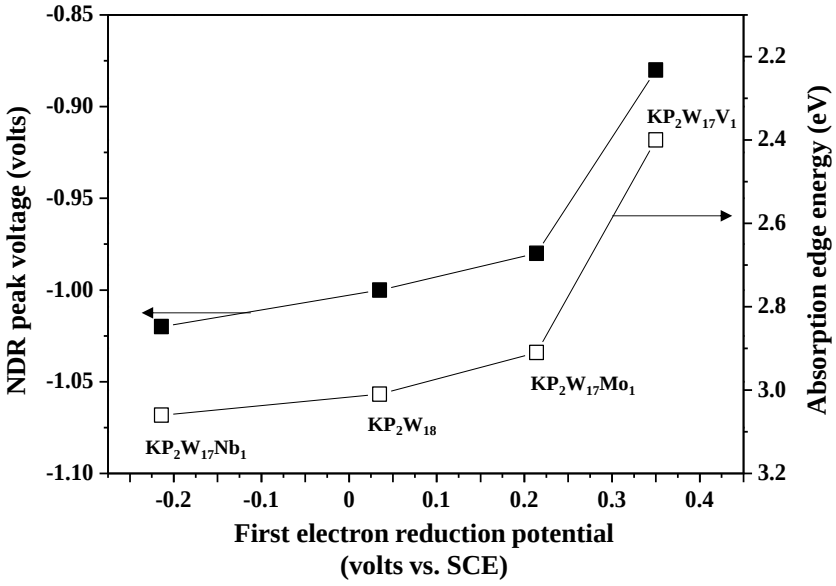

Fig. 3.17. Absorption edge energy and NDR peak voltage plotted as a function of reduction potential

3.2.3. Catalytic test

Gas-phase oxidative dehydrogenation of benzylamine was carried out over α-$K_6P_2W_{18}O_{62}$, α_2-$K_6P_2W_{17}Mo_1O_{62}$, α_2-$K_7P_2W_{17}V_1O_{62}$, and α_2-$K_7P_2W_{17}Nb_1O_{62}$ Wells-Dawson HPAs. The catalysts exhibited a stable catalytic performance during a 5 h-reaction. It was reported that dibenzylimine, benzonitrile, and benzaldehyde could be formed from the dehydrogenated intermediates, phenylmethanimine as shown in Figure 3.18 [45]. Unstable phenylmethanimine reacts with another molecule benzylamine to form aminal and then release an NH_3 to form the dibenzylimine. Benzonitrile is formed by further oxidative dehydrogenation of phynylmethanimine. Benzaldehyde is formed by hydrolysis of phenylmethanimine.

In this work, dibenzylimine was mainly formed and trace amounts of benzonitrile and benzaldehyde were detected. It is noteworthy that none of them was detected without oxygen, supporting that dibenzylimine, benzonitrile, benzaldehyde is formed via oxidative dehydrogenation reaction. It was also found that benzylamine readily reacted with benzaldehyde to form dibenzylimine even at room temperature, indicating that as-produced benzaldehyde could react with benzylamine to form dibenzylimine. Figure 3.19 shows the catalytic performance of α_2-$K_7P_2W_{17}V_1O_{62}$ during the 5 h-reaction and yield for dibenzylimine after a 5 h-reaction. Interestingly, yield for dibenzylimine increased in the order of α_2-$K_7P_2W_{17}Nb_1O_{62}$ < α-$K_6P_2W_{18}O_{62}$ < α_2-$K_6P_2W_{17}Mo_1O_{62}$ < α_2-$K_7P_2W_{17}V_1O_{62}$.

When considering the fact that vanadium center is easier to be reduced

than other metal centers in the electrochemical measurement, it is inferred that vanadium-substitution provided efficient active sites for oxidative dehydrogenation by contributing to the density of accessible electronic states (unoccupied orbitals). This result also suggests that reducibility of mono-transition metal-substituted HPAs plays an important role in the oxidative dehydrogenation of benzylamine.

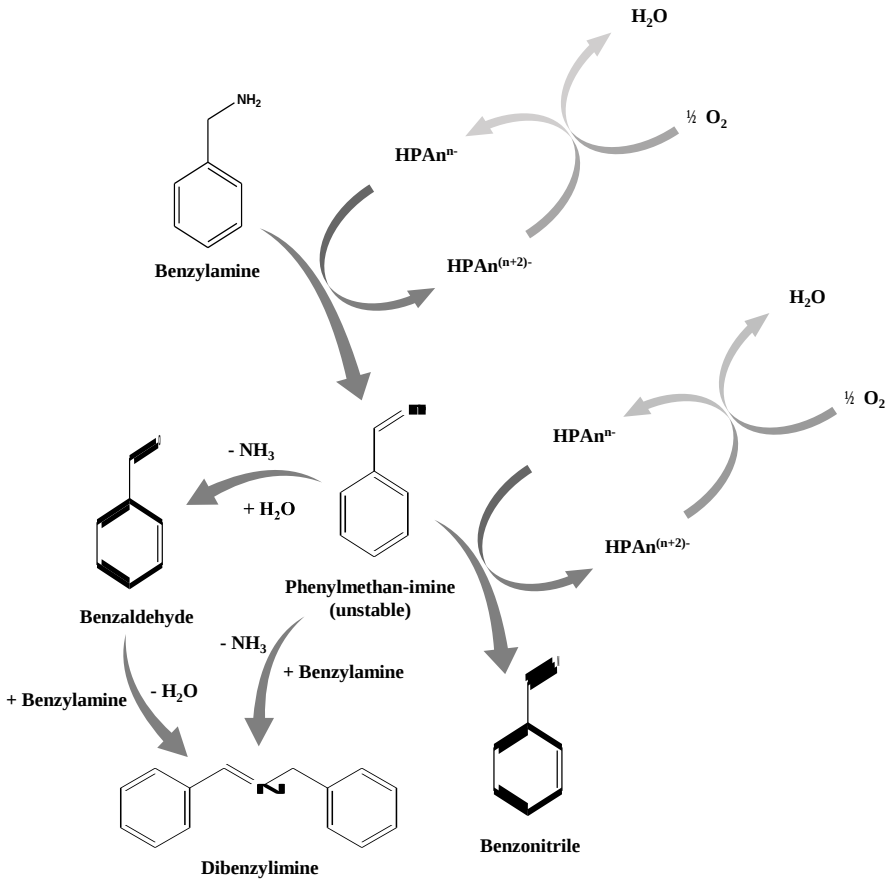

Fig. 3.18. Plausible reaction mechanism for the oxidative dehydrogenation of benzylamine [45].

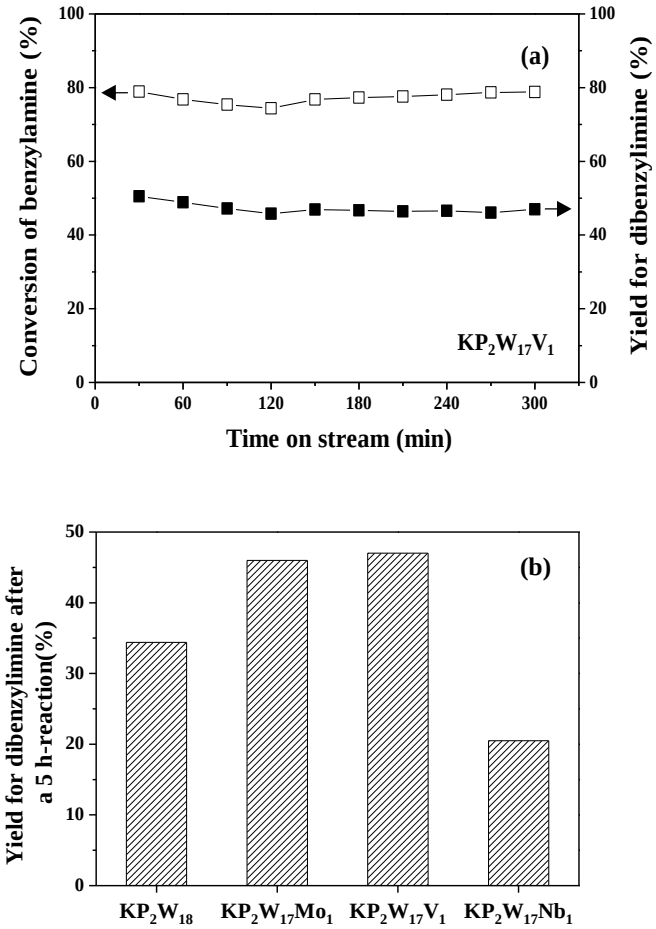

Fig. 3.19. (a) Catalytic performance of α_2-$K_7P_2W_{17}V_1O_{62}$ during the 5 h-reaction and (b) yield for dibenzylimine after a 5 h-reaction.

3.3. Keggin-type heteropolytungstates with different central atom

3.3.1. Formation of HPA structure

Figure 3.20 shows the DRIFT spectra of α-$H_nXW_{12}O_{40}$ ($X=Co^{2+}$, B^{3+}, Si^{4+}, and P^{5+}) Keggin HPAs. The spectrum of α-$H_6CoW_{12}O_{40}$ catalyst exhibited characteristic bands at 960, 889, and 761 cm^{-1}, which were assigned to $W=O_t$, $W-O_c-W$, and $W-O_e-W$ stretching vibrations, respectively. The characteristic band for Co-O stretching vibration (445 cm^{-1}) was not presented in this figure. The spectrum of α-$H_5BW_{12}O_{40}$ catalyst exhibited characteristic bands at 955, 904, 814, and 753 cm^{-1}, which were assigned to $W=O_t$, W-O, $W-O_c-W$, and $W-O_e-W$ stretching vibrations, respectively. The characteristic band at 1001 cm^{-1} corresponded to the maximum of W-O-B stretching mode for α-$H_5BW_{12}O_{40}$. The characteristic band for B-O stretching vibration (1410 cm^{-1}) was not presented in this figure. The spectrum of α-$H_4SiW_{12}O_{40}$ catalyst exhibited characteristic bands at 979, 924, 885, and 787 cm^{-1}, which were assigned to $W=O_t$, Si-O, $W-O_c-W$, and $W-O_e-W$ stretching vibrations, respectively. The spectrum of α-$H_3PW_{12}O_{40}$ catalyst exhibited characteristic bands at 1080, 984, 888, and 810 cm^{-1}, which were assigned to P-O, $W=O_t$, $W-O_c-W$, and $W-O_e-W$ stretching vibrations, respectively. X-O bands of α-$H_nXW_{12}O_{40}$ HPA catalysts did not show any band splitting, indicating the existence of T_d local symmetry of a central XO_4 unit that is a characteristic feature of α-Keggin structure. All positions of characteristic IR bands of α-$H_nXW_{12}O_{40}$ HPA catalysts were in good agreement with the results of

previous works [1,46,47], indicating successful formation of heteropolyanion frameworks.

Elemental compositions of α-$H_nXW_{12}O_{40}$ ($X=Co^{2+}$, B^{3+}, Si^{4+}, and P^{5+}) Keggin HPAs were calculated from the results of ICP-AES measurements. Chemical compositions of central atom and tungsten in the α-$H_nXW_{12}O_{40}$ ($X=Co^{2+}$, B^{3+}, Si^{4+}, and P^{5+}) Keggin HPAs were summarized in Table 3.7.

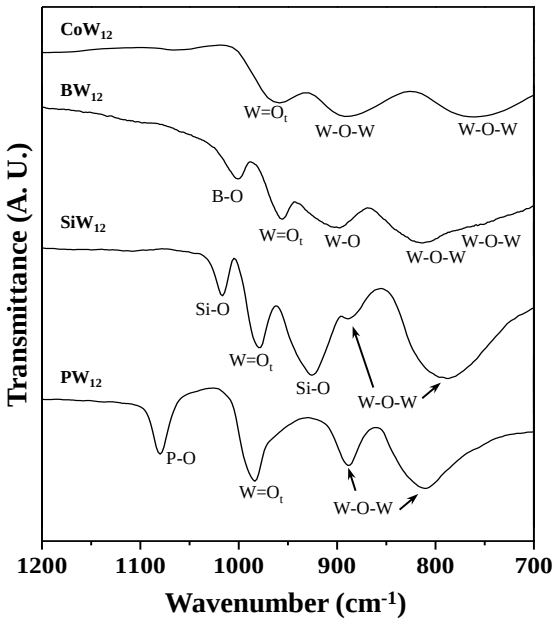

Fig. 3.20. DRIFT spectra of α-$H_nXW_{12}O_{40}$ (X=Co^{2+}, B^{3+}, Si^{4+}, and P^{5+}) Keggin HPAs

Table. 3.7.

Chemical compositions of central atom (X) and tungsten in the α-$H_nXW_{12}O_{40}$ ($X=Co^{2+}$, B^{3+}, Si^{4+}, and P^{5+}) Keggin HPAs

Catalyst	Ratio of X:W	
	Theoretical value	Measured value
PW_{12}	1.00 : 12.00	0.94 : 12.00
SiW_{12}	1.00 : 12.00	0.93 : 12.00
BW_{12}	1.00 : 12.00	1.08 : 12.00
CoW_{12}	1.00 : 12.00	1.05 : 12.00

3.3.2. Characterization

3.3.2.1. Cyclic voltammetry

Figure 3.21 shows the cyclic voltammograms of α-$H_nXW_{12}O_{40}$ (X=Co^{2+}, B^{3+}, Si^{4+}, and P^{5+}) Keggin HPAs. Electrochemical measurements were performed under consistent experimental conditions to provide the comparable results. All α-$H_nXW_{12}O_{40}$ HPA catalysts exhibited well-defined reversible and stepwise tungsten-centered redox transitions during the electrochemical measurements. Five couples of one-electron redox waves were observed for α-$H_3PW_{12}O_{40}$ catalyst. Three couples of redox waves were observed for α-$H_4SiW_{12}O_{40}$ catalyst with electron ratios of 1:1:2. Two couples of redox waves with electron ratios of 2:1 were observed for α-$H_5BW_{12}O_{40}$ catalyst. Three couples of one-electron redox waves were observed for α-$H_6CoW_{12}O_{40}$ catalyst.

First electron reduction potential was increased in the order of α-$H_6CoW_{12}O_{40}$ < α-$H_5BW_{12}O_{40}$ < α-$H_4SiW_{12}O_{40}$ < α-$H_3PW_{12}O_{40}$ catalysts. First electron reduction potential was summarized in Table 3.8. Among the tested HPA catalysts, α-$H_3PW_{12}O_{40}$ catalyst showed the most positive reduction potential. It is well known that added electrons to α-type Keggin heteropolytungstates were delocalized over tungsten sites. This indicates that each redox transition during the electrochemical measurements corresponded to electron transfer related to tungsten sites and nature of central atom would not directly affect the reduction potential, but indirectly [48].

Previous density functional theory (DFT) calculations [49,50] has been

reported the effect of heteroatom charge and size on electronic structure using a clathrate model, in which tetrahedral XO_4^{n-} units are encapsulated within neutral $W_{12}O_{40}$ cage ($XO_4^{n-}@W_{12}O_{40}$). It has been demonstrated that Keggin-type heteropolyanion with larger negative charge and smaller size resulted in poor reducibility due to the smaller capacity to accept electrons, in good agreement with the results of this work.

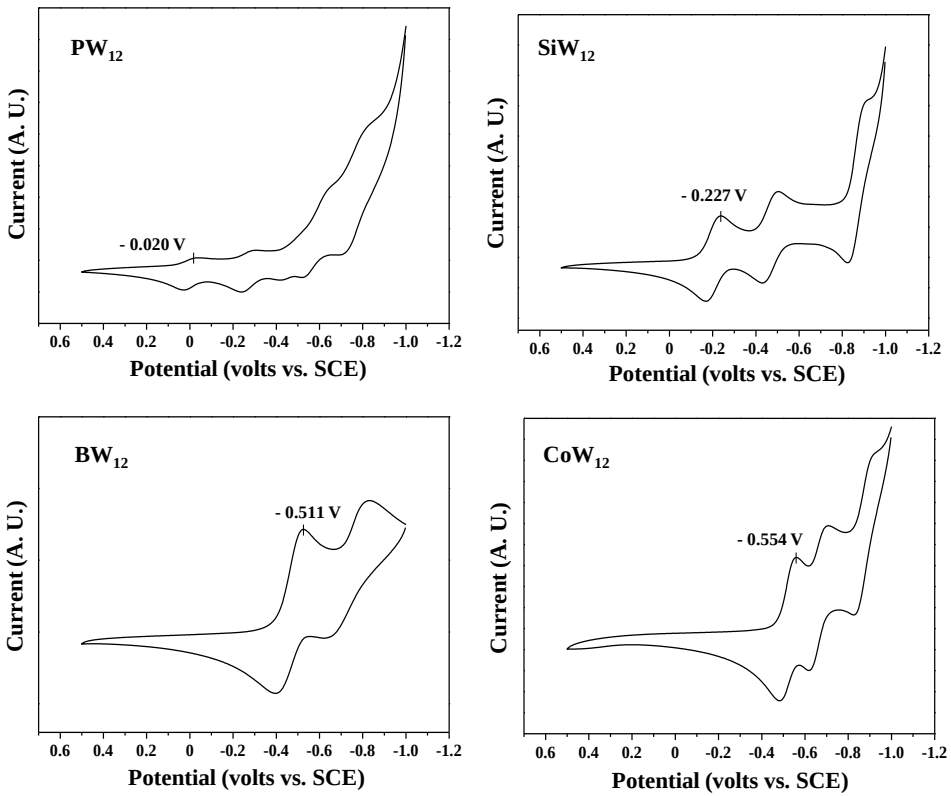

Fig. 3.21. Cyclic voltammograms of α-$H_nXW_{12}O_{40}$ (X=Co^{2+}, B^{3+}, Si^{4+}, and P^{5+}) Keggin HPAs.

3.3.2.2. UV-visible spectroscopy

Fig. 3.22 shows the $[F(R_\infty)\cdot h\nu]^{1/2}$ curves of α-$H_nXW_{12}O_{40}$ ($X=Co^{2+}$, B^{3+}, Si^{4+}, and P^{5+}) Keggin HPAs. Because absorption edge energy of HPA catalysts are typically sensitive to number of crystalline water molecules, UV-visible spectroscopy measurements were carried out in solution to be fully solvated by water, giving rise to consistent number of crystalline water. Absorption edge energy of α-$H_nXW_{12}O_{40}$ HPA catalysts determined by UV-visible spectroscopy decreased in the order of α-$H_6CoW_{12}O_{40}$ > α-$H_5BW_{12}O_{40}$ > α-$H_4SiW_{12}O_{40}$ > α-$H_3PW_{12}O_{40}$ catalysts. Absorption edge energies were summarized in Table 3.8. The trend of absorption edge energy is well consistent with that of reduction potential.

Unlike the case of metal-substitution in the site of addenda atom, the central atom within neutral $W_{12}O_{40}$ cage ($XO_4^{n-}@W_{12}O_{40}$) significantly affect the both the HOMO and the LUMO [49]. Therefore, it is very hard to figure out the relative energy level of the LUMO. In the series of α-$H_nXW_{12}O_{40}$ ($X=Co^{2+}$, B^{3+}, Si^{4+}, and P^{5+}) Keggin HPAs, the only information estimated from the absorption edge energy was that the heteropolyanion with larger negative charge and smaller size resulted in large energy gap.

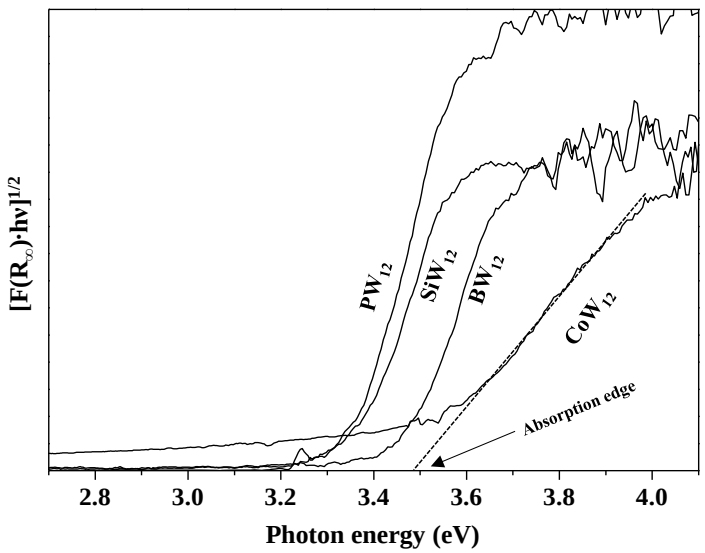

Fig. 3.22. $[F(R_\infty)\cdot hv]^{1/2}$ curves of α-$H_nXW_{12}O_{40}$ ($X=Co^{2+}$, B^{3+}, Si^{4+}, and P^{5+}) Keggin HPAs.

3.3.2.3. Scanning tunneling microscopy

NDR peak voltages of α-$H_nXW_{12}O_{40}$ (X=Co^{2+}, B^{3+}, Si^{4+}, and P^{5+}) Keggin HPAs determined by tunneling spectroscopy were taken from the previous literature [32]. The average values of NDR peak voltage were summarized in Table 3.8. The trend of NDR peak voltage is well consistent with that of absorption edge energy. As mentioned, it is very hard to figure out the relative energy level of the LUMO from absorption edge energy because the central atom within neutral $W_{12}O_{40}$ cage (XO_4^{n-}@$W_{12}O_{40}$) significantly affect the both the HOMO and the LUMO. However, it can be inferred from the trend of NDR peak voltages that energy level of the LUMO decreased in the order of α-$H_6CoW_{12}O_{40}$ > α-$H_5BW_{12}O_{40}$ > α-$H_4SiW_{12}O_{40}$ > α-$H_3PW_{12}O_{40}$.

Figure 3.23 shows the absorption edge energy and NDR peak voltage plotted as a function of reduction potential. The correlations suggested that reduction potential could be estimated from the electronic structure in the Keggin-type heteropolytungstates with different central atom. Among the tested, P^{5+} is the most effective to enhance the reducibility of heteropolyanion framework. The central PO_4^{3-} unit provided electrochemically accessible tungsten centers which is easier to be reduced (than other central XO_4^{n-} units), resulting in the highest reduction potential. The correlations also suggested that absorption edge energy and NDR peak voltage could be utilized as alternative correlating parameters for reduction potential in the series of α-$H_nXW_{12}O_{40}$ (X=Co^{2+}, B^{3+}, Si^{4+}, and P^{5+}) Keggin HPAs.

Table. 3.8.

First electron reduction potentials, absorption edge energies, and NDR peak voltages of α-$H_nXW_{12}O_{40}$ ($X=Co^{2+}$, B^{3+}, Si^{4+}, and P^{5+}) Keggin HPAs.

Catalyst	1^{st} electron reduction potential (volts vs. SCE)	UV-visible absorption edge energy (eV)	NDR peak voltage (volts)*
PW_{12}	-0.020	3.35	-1.14
SiW_{12}	-0.227	3.37	-1.19
BW_{12}	-0.511	3.47	-1.28
CoW_{12}	-0.554	3.48	-1.36

*Data were taken from the previous literature [32].

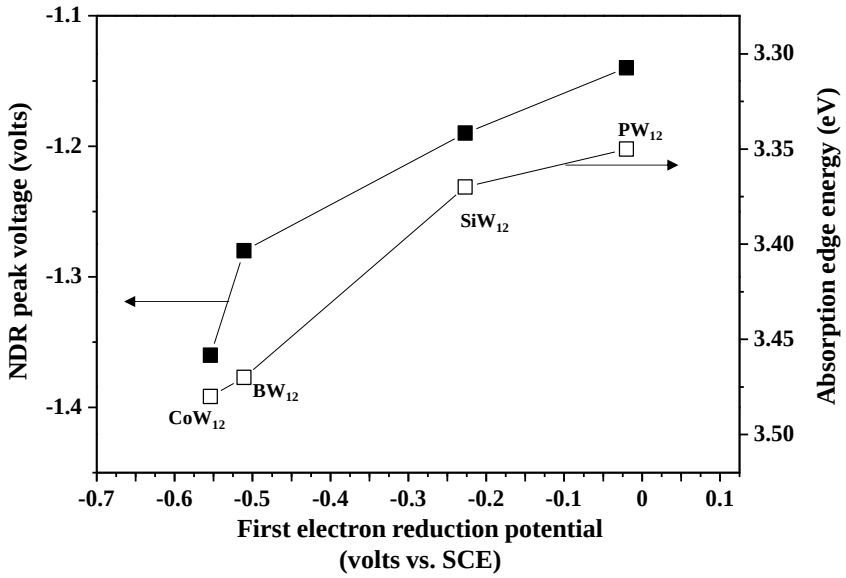

Fig. 3.23. Absorption edge energy and NDR peak voltage plotted as a function of reduction potential.

3.4. Mo(VI)-substituted Wells-Dawson-type tungstoarsenates

3.4.1. Formation of HPA structure

Figure 3.24 shows the schematic diagram for the preparation procedures of α-$K_6As_2W_{18-x}Mo_xO_{62}$ (x=0-3) Wells-Dawson HPAs. Removal of cap WO_6 units in the α-$K_6As_2W_{18}O_{62}$ by pH control yields mono-, di-, and tri-lacunary heteropolyanion. In this work, molybdenum-substituted Wells-Dawson tungstoarsenates were prepared by direct incorporation of molybdenum ions into mono-, di-, and tri-lacunary tungstoarsenates, derived from α-$K_6As_2W_{18}O_{62}$ via selective degradation. Therefore, molybdenum was selectively substituted on the cap sites of Wells-Dawson structure, giving the uniform molecular structure.

Successful formation of heteropolyanion frameworks was confirmed by DRIFT spectroscopy. Figure 3.25 shows the DRIFT spectra of α-$K_6As_2W_{18-x}Mo_xO_{62}$ (x=0-3) Wells-Dawson HPAs. Typical characteristic bands of Wells-Dawson heteropolyanion were observed in the range of 700-1000 cm^{-1}. For α-$K_6As_2W_{18}O_{62}$, the characteristic bands attributed to W-O-W asymmetric stretching vibrations were observed at 894, 868, 833, 770 cm^{-1}. The band attributed to $W=O_t$ asymmetric stretching was observed at 974 cm^{-1}. The single band attributed to As-O vibration appeared at the wavenumber (974 cm^{-1}) near W-O-W bands. Molybdenum-substituted tungstoarsenates (α-$K_6As_2W_{18-x}Mo_xO_{62}$ (x=1-3)) exhibited a little shifted bands with no significant difference compared to $K_6As_2W_{18}O_{62}$. Although the local T_d symmetry of central AsO_4 units might be

lowered by molybdenum-substitution, the bands attributed to vibration mode of As-O appeared as a single weak shoulder with no band splitting. Therefore, it is inferred that the bands corresponding to central AsO_4 were hidden under the broad and intense M-O-M bands, resulting in a single band for central AsO_4. This result was well consistent with the result of previous work [34], indicating that a series of molybdenum-substituted Wells-Dawson tungstoarsenates were successfully prepared. Successful preparation of the catalysts were further confirmed by ICP-AES analyses. The chemical compositions of arsenic, tungsten, and molybdenum in the α-$K_6As_2W_{18-x}Mo_xO_{62}$ (x=0-3) Wells-Dawson HPAs determined by ICP-AES measurements were summarized in Table 3.7. Chemical compositions were in good agreement with the designed values.

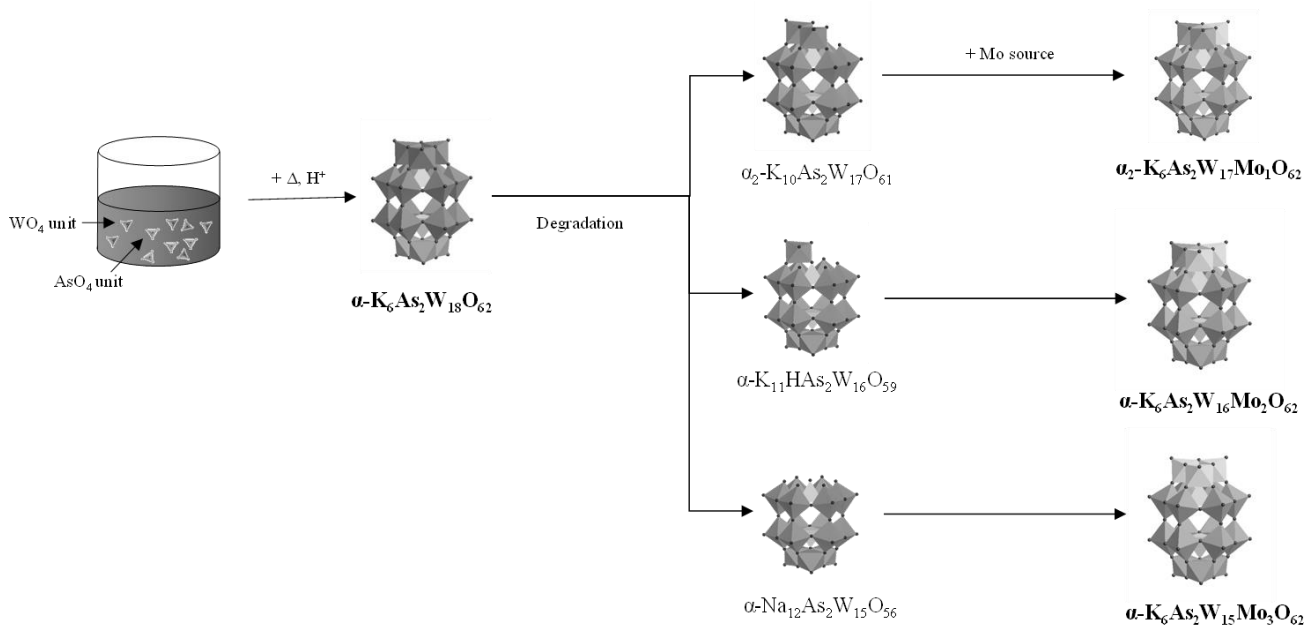

Fig. 3.24. Schematic diagram for the preparation procedures of α-$K_6As_2W_{18-x}Mo_xO_{62}$ (x=0-3) Wells-Dawson HPAs.

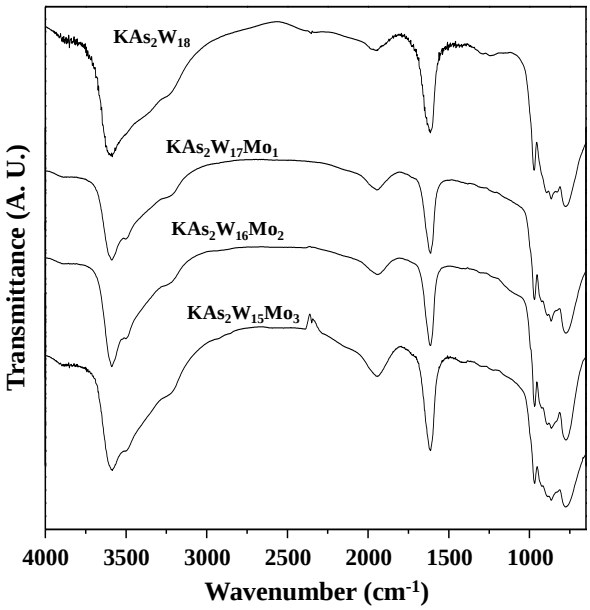

Fig. 3.25. DRIFT spectra of α-$K_6As_2W_{18-x}Mo_xO_{62}$ (x=0-3) Wells-Dawson HPAs.

Table 3.9.

Detailed assignment of each characteristic band

Catalyst	Wavenumber (cm^{-1})		
	As-O	$M=O_t$	M-O-M
KAs_2W_{18}	974	928	894, 868, 833, 770
$KAs_2W_{17}Mo_1$	970	924	891, 865, 837, 769
$KAs_2W_{16}Mo_2$	968	923	890, 862, 829, 770
$KAs_2W_{15}Mo_3$	968	925	893, 861, 831, 772

*O_t: terminal oxygen

Table 3.10.

Chemical compositions of arsenic, tungsten, and molybdenum in the α-$K_6As_2W_{18-x}Mo_xO_{62}$ (x=0-3) Wells-Dawson HPAs

Catalyst	Ratio of As:W:Mo	
	Theoretical value	Measured value
KAs_2W_{18}	2.0 : 18.0 : 0	2.0 : 18.0 : 0
$KAs_2W_{17}Mo_1$	2.0 : 17.0 : 1.0	1.9 : 17.0 : 0.9
$KAs_2W_{16}Mo_2$	2.0 : 16.0 : 2.0	1.9 : 16.0 : 1.9
$KAs_2W_{15}Mo_3$	2.0 : 15.0 : 3.0	1.9 : 15.0 : 2.9

3.4.2. Characterization

3.4.2.1. Cyclic voltammetry

Electrochemical measurements were carried out to examine the electrochemical redox transitions of α-$K_6As_2W_{18-x}Mo_xO_{62}$ (x=0-3) Wells-Dawson HPAs. Figure 3.26 shows the cyclic voltammograms of α-$K_6As_2W_{18-x}Mo_xO_{62}$ (x=0-3) Wells-Dawson HPAs. α-$K_6As_2W_{18-x}Mo_xO_{62}$ (x=0-3) showed reversible and stepwise redox transitions during the electrochemical measurements. Overall shapes of redox waves were maintained at the measured scan rates in this work (up to 200 mV/s). For all α-$K_6As_2W_{18-x}Mo_xO_{62}$ (x=0-3), the linear relationship between peak current and square root of scan rate was observed, suggesting that these redox transitions were diffusion-controlled process expressed by the Randles-Sevcik equation. α-$K_6As_2W_{18}O_{62}$ exhibited four tungsten-centered redox transitions in this scan range. However, molybdenum-substituted α-$K_6As_2W_{18-x}Mo_xO_{62}$ (x=1-3) exhibited an additional molybdenum-centered redox transition at more positive potential. This indicates that molybdenum center is electrochemically more accessible and added electrons are more easily localized on molybdenum sites than tungsten sites.

First electron reduction potentials determined by electrochemical analysis are summarized in Table 3.11. First electron reduction potential increased with increasing molybdenum content in the series of α-$K_6As_2W_{18-x}Mo_xO_{62}$ (x=0-3) Wells-Dawson HPAs.

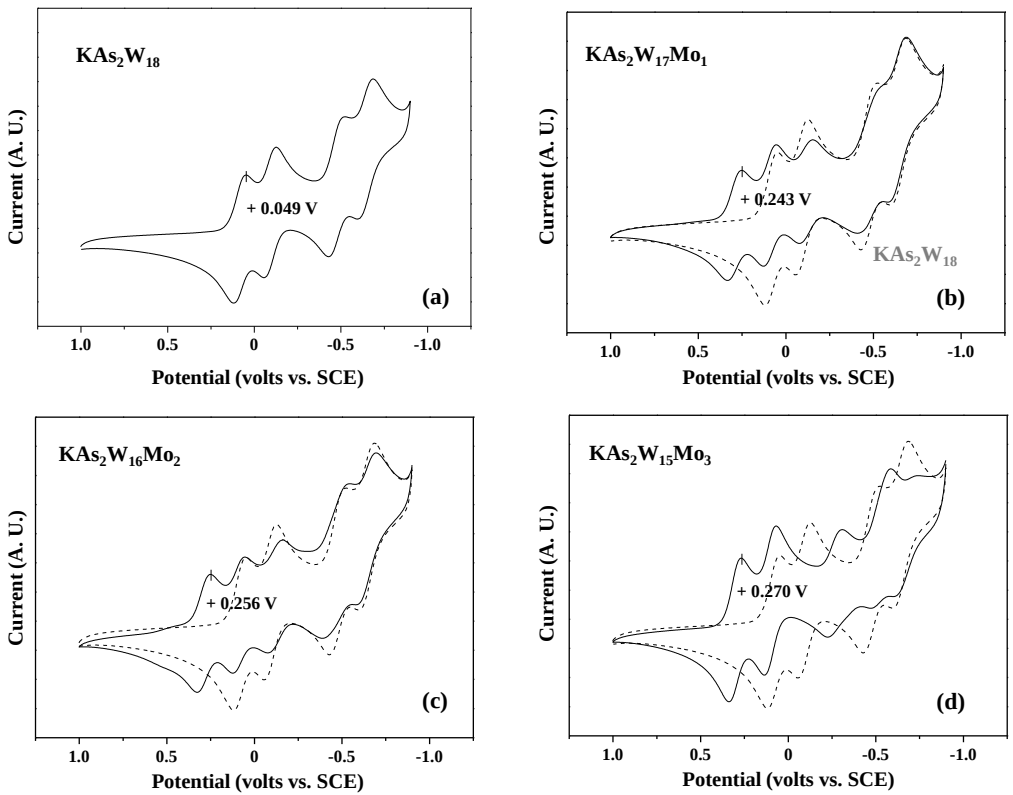

Fig. 3.26. Cyclic voltammograms of α-$K_6As_2W_{18-x}Mo_xO_{62}$ (x=0-3) Wells-Dawson HPAs.

3.4.2.2. UV-visible spectroscopy

Figure 3.27 shows the $[F(R_\infty)\cdot h\nu]^{1/2}$ curves of α-$K_6As_2W_{18-x}Mo_xO_{62}$ (x=0-3). Absorption edge energies were directly obtained from the linear fit of $[F(R_\infty)\cdot h\nu]^{1/2}$ curve and summarized in Table 3.11. Absorption edge energy (energy gap between the HOMO and the LUMO) determined by UV-visible spectroscopy decreased with increasing molybdenum content. The trend of absorption edge energy is well consistent with that of reduction potential. Like the case of transition metal-substituted Wells-Dawson tungstophosphates, it could be understood by considering the fact that molybdenum-substitution stabilized the energy level of metal centers at cap sites and reduction of metal centers at cap sites was available. Difference in energy gap of α-$K_6As_2W_{18-x}Mo_xO_{62}$ (x=1-3) can also be understood by considering the contribution of molybdenum to the LUMO. Because the HOMO mostly comprises 2p-orbitals on the framework oxygens, as mentioned, it is nearly unchanged by molybdenum-substitution and the energy gap only depends on the LUMO. This indicates that absorption edge energy can be utilized as an alternative diagnostic to estimate the energy state and reduction potential in the series of molybdenum-substituted Wells-Dawson tungstoarsenates.

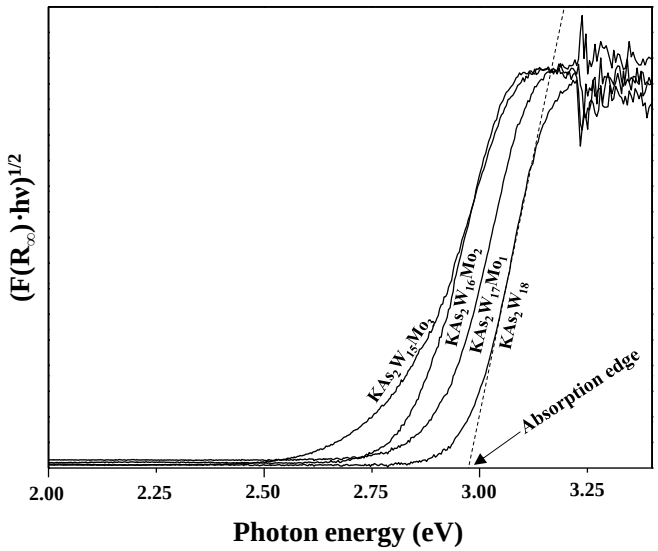

Fig. 3.27. $[F(R_\infty)\cdot h\nu]^{1/2}$ curves of α-$K_6As_2W_{18-x}Mo_xO_{62}$ (x=0-3) Wells-Dawson HPAs.

3.4.2.3. Scanning tunneling microscopy

Figure 3.28 shows the STM images of α-$K_6As_2W_{18}O_{62}$. Two-dimensional self-assembled HPA array was observed in the STM measurement. Each bright corrugation in the STM images represents individual heteropolyanion. The periodicity of unit cell constructed on the basis of lattice constants determined from two-dimensional fast Fourier transform analysis (2D FFT) was 20.9 Å × 21.9 Å with included angle of 60.2°. The dimension of unit cell determined from STM image was matched with the lattice constant determined by X-ray crystallography [2]. Figure 3.29 shows the typical current-voltage responses of α-$K_6As_2W_{18}O_{62}$ taken at two different sites (bright corrugation and interstitial space between bright corrugations) in Figure 3.28. Current-voltage response at bare graphite was also measured for comparison purpose. It is noteworthy that current-voltage response taken at interstitial space between bright corrugations was almost identical to that of bare graphite, indicating that two-dimensional HPA array shown in Figure 3.28 was monolayer. On the other hand, tunneling spectrum taken at bright corrugation showed a distinctive current-voltage response, referred to as negative differential resistance (NDR) phenomenon. The statistical average value of NDR peak voltage of α-$K_6As_2W_{18}O_{62}$ was found to be -1.01 V. The statistical NDR peak voltages of α-$K_6As_2W_{18-x}Mo_xO_{62}$ (x=0-3) are summarized in Table 3.11. It is interesting to note that NDR peak voltage of α-$K_6As_2W_{18-x}Mo_xO_{62}$ (x=0-3) shifted less negative voltage with increasing molybdenum content.

Figure 3.30 shows the absorption edge energy and NDR peak voltage plotted as a function of reduction potential. The correlation suggested that

reduction potential could be estimated from the electronic structure. As a results, molybdenum center is more effective to enhance the reducibility of heteropolyanion framework than tungsten center in the series of α-$K_6As_2W_{18-x}Mo_xO_{62}$ (x=0-3) Wells-Dawson HPAs. The molybdenum-substitution provided electrochemically accessible molybdenum centers which is easier to be reduced, resulting in the higher reduction potential. The correlations suggested that absorption edge energy and NDR peak voltage could be utilized as alternative correlating parameters for reduction potential of bulk HPAs in the series of α-$K_6As_2W_{18-x}Mo_xO_{62}$ (x=0-3) Wells-Dawson HPAs.

.

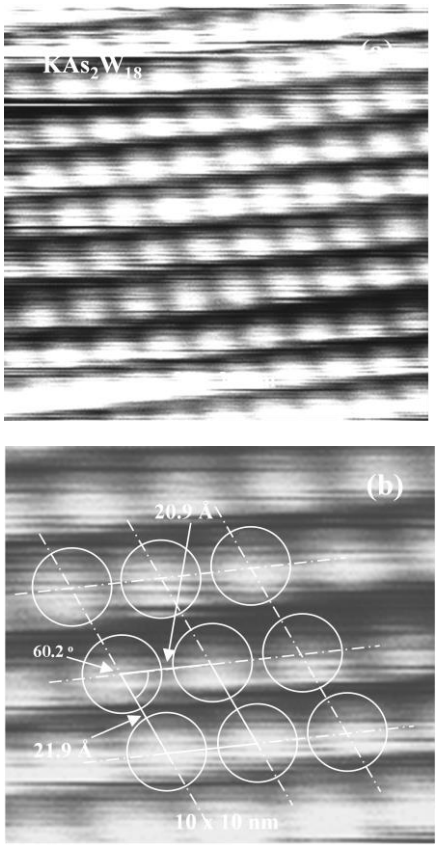

Fig. 3.28. STM images of α-$K_6As_2W_{18}O_{62}$ Wells-Dawson HPA: (a) 20 x 20 nm and (b) 10 x 10 nm.

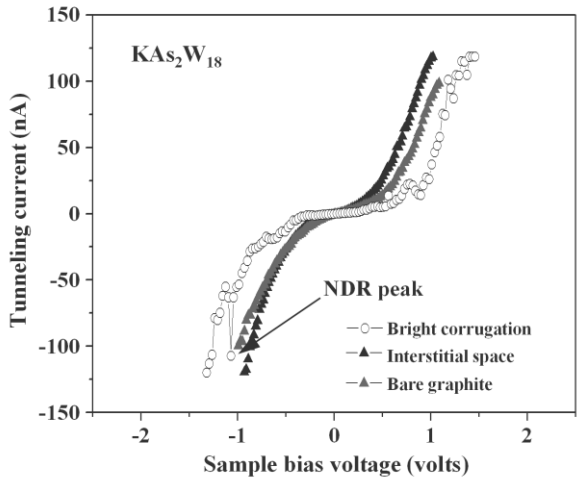

Fig. 3.29. Typical tunneling spectra of α-$K_6As_2W_{18}O_{62}$ Wells-Dawson HPA taken at two different sites (bright corrugation and interstitial space between bright corrugations) in Figure 3.28.

Table. 3.11.

First electron reduction potentials, absorption edge energies, and NDR peak voltages of α-$K_6As_2W_{18-x}Mo_xO_{62}$ (x=0-3) Wells-Dawson HPAs

Catalyst	1^{st} electron reduction potential (volts vs. SCE)	UV-visible absorption edge energy (eV)	NDR peak voltage (volts)
KAs_2W_{18}	+0.049	2.97	-1.01
$KAs_2W_{17}Mo_1$	+0.243	2.90	-0.99
$KAs_2W_{16}Mo_2$	+0.256	2.84	-0.98
$KAs_2W_{15}Mo_3$	+0.270	2.79	-0.95

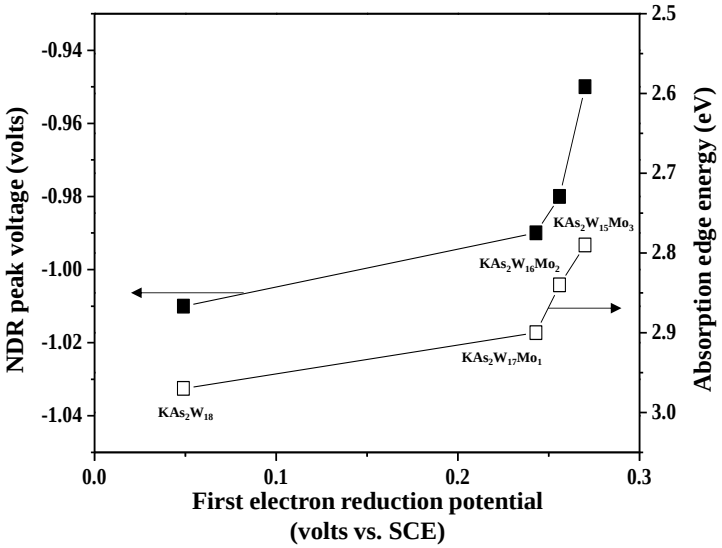

Fig. 3.30. Absorption edge energy and NDR peak voltage plotted as a function of reduction potential.

3.4.3. Catalytic test

Gas-phase oxidative dehydrogenation of benzyl alcohol was carried out over α-$K_6As_2W_{18-x}Mo_xO_{62}$ (x=0-3) Wells-Dawson HPAs. The catalysts exhibited a stable catalytic performance during a 5 h-reaction. Benzaldehyde was mainly formed as an oxidation product, and small amounts of toluene and benzyl ether were also detected [51]. Yield for benzaldehyde (oxidation product) increased with increasing molybdenum content. This supports that HPAs with reducible metal centers shows the excellent catalytic acidity in the oxidative dehydrogenation reaction. Similar results have been reported in the oxidative dehydrogenation of 2-propanol [20]. They showed that the rate-determining step involved reduction of HPA with β-hydrogen eliminated from the substrate and the intrinsic reaction rate was well correlated with reducibility of HPA.

When considering the fact that molybdenum center is easier to be reduced than other tungsten centers in the electrochemical measurement, it is inferred that molybdenum-substitution provided efficient active sites for oxidative dehydrogenation by contributing the accessible electronic state (unoccupied orbital). This result suggests that reducibility of the metal centers in the HPA framework plays an important role in the oxidative dehydrogenation reaction.

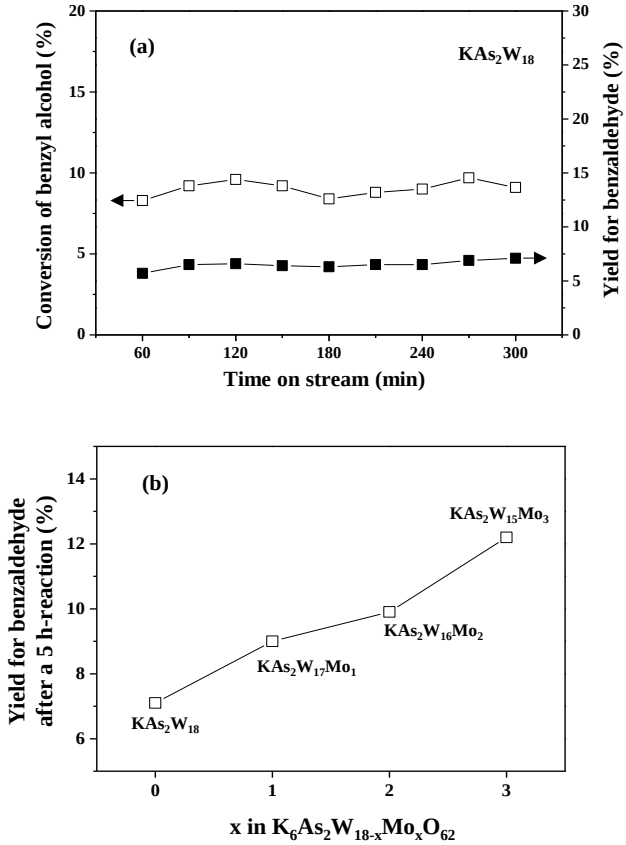

Fig. 3.31. (a) Catalytic performance of α-$K_6As_2W_{18}O_{62}$ during a 5 h-reaction and (b) yield for acetaldehyde after a 5 h-reaction plotted as a function of molybdenum content.

3.5. V(V) and Nb(V)-substituted Wells-Dawson-type tungstoarsenates

3.5.1. Formation of HPA structure

α_2-$K_7As_2W_{17}V_1O_{62}$ and α_2-$K_7As_2W_{17}Nb_1O_{62}$ were prepared to elucidate the effect of group 5-metal-substitution on the redox properties and electronic structure in the Wells-Dawson-type tungstoarsenate frameworks. α-$K_6As_2W_{18}O_{62}$ and α_2-$K_6As_2W_{17}Mo_1O_{62}$ were also prepared for the comparison. Figure 3.32 shows the schematic diagram for the preparation procedures of α-$K_6As_2W_{18}O_{62}$, α_2-$K_6As_2W_{17}Mo_1O_{62}$, α_2-$K_7As_2W_{17}V_1O_{62}$, and α_2-$K_7As_2W_{17}Nb_1O_{62}$ Wells-Dawson HPAs. Mono-transition metal-substituted Wells-Dawson tungstoarsenates were prepared by direct incorporation of transition metal into the mono-lacunary α_2-$K_{10}As_2W_{17}O_{61}^{10-}$. As a results, a tungsten center at cap site was selectively replaced by a transition metal.

Figure 3.33 shows the DRIFT spectra of α-$K_6As_2W_{18}O_{62}$, α_2-$K_6As_2W_{17}Mo_1O_{62}$, α_2-$K_7As_2W_{17}V_1O_{62}$, and α_2-$K_7As_2W_{17}Nb_1O_{62}$ Wells-Dawson HPAs. Successful formations of the heteropolyanions were confirmed by four characteristic bands in the range of 1000-700 cm^{-1}, which represents As-O, M=O_t, inter-octahedral M-O_c-M, and intra-octahedral M-O_e-M bonds (M=metal).. Detailed assignment of each characteristic band was summarized in Table 3.12. Unfortunately, α-$K_6As_2W_{18}O_{62}$, α_2-$K_6As_2W_{17}Mo_1O_{62}$, α_2-$K_7As_2W_{17}V_1O_{62}$, and α_2-$K_7As_2W_{17}Nb_1O_{62}$ Wells-Dawson HPAs showed no peaks in ^{75}As NMR analyses.

Chemical compositions of phosphorous, tungsten, and substituted-metal of the HPAs were further confirmed by ICP-AES analyses. Chemical compositions of arsenic, tungsten, and substituted-metal in the α-$K_6As_2W_{18}O_{62}$, α_2-$K_6As_2W_{17}Mo_1O_{62}$, α_2-$K_7As_2W_{17}V_1O_{62}$, and α_2-$K_7As_2W_{17}Nb_1O_{62}$ Wells-Dawson HPAs were summarized in table 3.13. The molar ratios of P:W:M were in good agreement with the theoretical values, suggesting the successful formation of HPA structures.

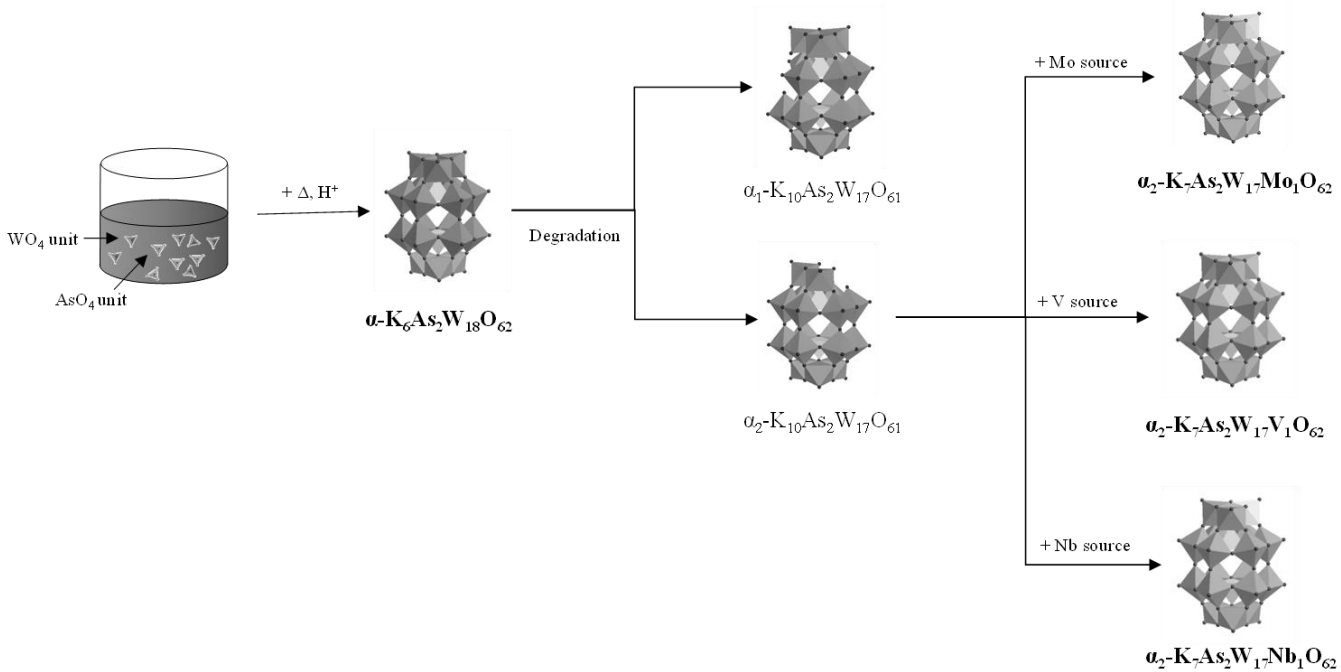

Fig. 3.32. Schematic diagram for the preparation procedures of α-$K_6As_2W_{18}O_{62}$, α_2-$K_6As_2W_{17}Mo_1O_{62}$, α_2-$K_7As_2W_{17}V_1O_{62}$, and α_2-$K_7As_2W_{17}Nb_1O_{62}$ Wells-Dawson HPAs.

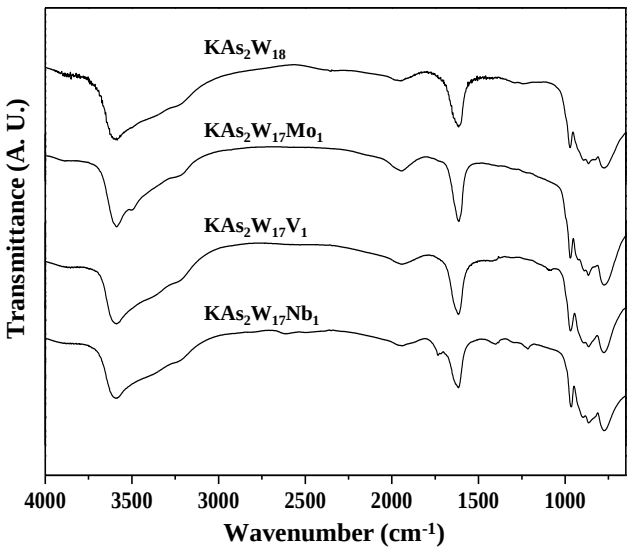

Fig. 3.33. DRIFT spectra of α-$K_6As_2W_{18}O_{62}$, α_2-$K_6As_2W_{17}Mo_1O_{62}$, α_2-$K_7As_2W_{17}V_1O_{62}$, and α_2-$K_7As_2W_{17}Nb_1O_{62}$ Wells-Dawson HPAs.

Table 3.12.

Detailed assignment of each characteristic band

Catalyst	Wavenumber (cm^{-1})		
	As-O	$M=O_t$	M-O-M
KAs_2W_{18}	974	928	894, 868, 833, 770
$KAs_2W_{17}Mo_1$	970	924	891, 865, 837, 769
$KAs_2W_{17}V_1$	968	-	892, 865, 830, 775
$KAs_2W_{17}Nb_1$	968	926	899, 864, 825, 776

*O_t: terminal oxygen

Table 3.13.

Chemical compositions of arsenic, tungsten, and substituted-metal (M) in the α-$K_6As_2W_{18}O_{62}$, α_2-$K_6As_2W_{17}Mo_1O_{62}$, α_2-$K_7As_2W_{17}V_1O_{62}$, and α_2-$K_7As_2W_{17}Nb_1O_{62}$ Wells-Dawson HPAs

Catalyst	Ratio of As:W:M	
	Theoretical value	Measured value
KAs_2W_{18}	2.0 : 18.0 : 0	2.0 : 18.0 : 0
$KAs_2W_{17}Mo_1$	2.0 : 17.0 : 1.0	1.9 : 17.0 : 0.9
$KAs_2W_{17}V_1$	2.0 : 17.0 : 1.0	2.0 : 17.0 : 1.0
$KAs_2W_{17}Nb_1$	2.0 : 17.0 : 1.0	2.0 : 17.0 : 1.0

3.5.2. Characterization

3.5.2.1. Cyclic voltammetry

Figure 3.34 shows the cyclic voltammograms of α-$K_6As_2W_{18}O_{62}$, α_2-$K_6PAs_2W_{17}Mo_1O_{62}$, α_2-$K_7As_2W_{17}V_1O_{62}$, and α_2-$K_7As_2W_{17}Nb_1O_{62}$ Wells-Dawson HPAs. Four tungsten-based redox transitions were observed in the cyclic voltammogram of α-$K_6As_2W_{18}O_{62}$. In case of molybdenum- and vanadium-substituted Wells-Dawson tungstoarsenates showed an additional molybdenum- and vanadium-based redox transitions, respectively. The results are very similar with the case of Wells-Dawson tungstophosphates. However, niobium-substituted Wells-Dawson tungstoarsenates showed significantly shifted redox couples. This indicates vanadium or molybdenum center in the heteropolyanion framework was more electrochemically accessible and reducible than tungsten center in the Wells-Dawson tungstoarsenate frameworks. Otherwise, substituted-niobium has negative effect to the reducibility of Wells-Dawson tungstoarsenates. First electron reduction potentials are summarized in Table 3.14. Like, first electron reduction potential increased in the order of α_2-$K_7As_2W_{17}Nb_1O_{62}$ < α-$K_6As_2W_{18}O_{62}$ < α_2-$K_6As_2W_{17}Mo_1O_{62}$ < α_2-$K_7As_2W_{17}V_1O_{62}$.

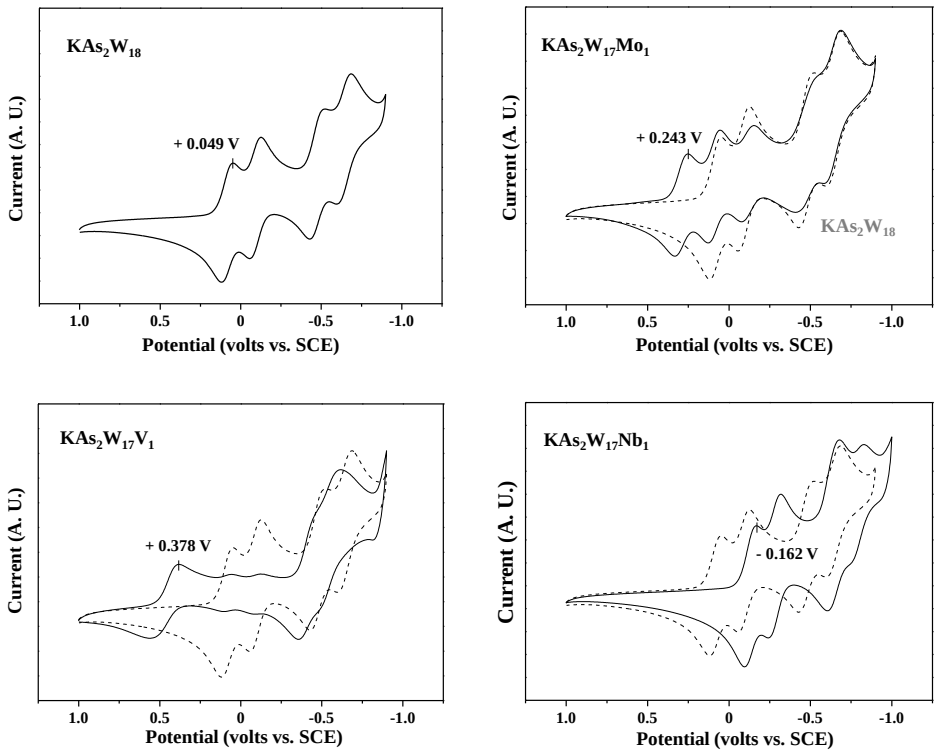

Fig. 3.34. Cyclic voltammograms of α-$K_6As_2W_{18}O_{62}$, α_2-$K_6As_2W_{17}Mo_1O_{62}$, α_2-$K_7As_2W_{17}V_1O_{62}$, and α_2-$K_7As_2W_{17}Nb_1O_{62}$ Wells-Dawson HPAs.

3.5.2.2. UV-visible spectroscopy

UV-visible spectroscopy measurements were conducted to probe the bulk electronic structures. Figure 3.35 shows the $[F(R_\infty)\cdot h\nu]^{1/2}$ curves of α-$K_6As_2W_{18}O_{62}$, α$_2$-$K_6As_2W_{17}Mo_1O_{62}$, α$_2$-$K_7As_2W_{17}V_1O_{62}$, and α$_2$-$K_7As_2W_{17}Nb_1O_{62}$ Wells-Dawson HPAs. Absorption edge energies are summarized in Table 3.14. Absorption edge energy (energy gap between the HOMO and the LUMO) decreased in the order of α$_2$-$K_7As_2W_{17}Nb_1O_{62}$ > α-$K_6As_2W_{18}O_{62}$ > α$_2$-$K_6As_2W_{17}Mo_1O_{62}$ > α$_2$-$K_7As_2W_{17}V_1O_{62}$. Because the HOMO is little perturbed by metal-substitution, it could be inferred that α$_2$-$K_7As_2W_{17}V_1O_{62}$ with the smallest absorption edge energy has the lowest energy level of the LUMO.

The difference in absorption edge energy could be understood by considering the differences in electron affinity of metal center, contribution of metal center to the LUMO, and symmetry of HPA structures. As mentioned above, niobium centers shows the greater predisposition than vanadium center to lose its electrons (hard to be reduced). Otherwise, vanadium-center largely contributes/stabilizes the LUMO. Similar with the case of Wells-Dawson tungstophosphates, the energy of metal centers at cap sites were stabilized by vanadium center and the electrochemical reduction of vanadium centers at cap sites became available. It is inferred that added electrons are preferentially delocalized over the vanadium centers. In case of α$_2$-$K_7As_2W_{17}Nb_1O_{62}$, it could be inferred that niobium center could not stabilize but elevate the energy level of metal centers. Therefore, reduction of metal centers at cap site was not available and showed negatively-shifted reduction potential. Among the tested, α$_2$-

$K_7As_2W_{17}V_1O_{62}$ with the smallest band gap showed the highest reduction potential.

Figure 3.36 shows the absorption edge energy plotted as a function of reduction potential. Reduction potential of the catalysts increased with decreasing absorption edge energy. This suggests that the electronic properties plays an important role to determine the reducibility of HPAs and absorption edge energy can be utilized as an alternative diagnostic to estimate the electronic structure and reduction potential in the series of α-$K_6As_2W_{18}O_{62}$, α_2-$K_6As_2W_{17}Mo_1O_{62}$, α_2-$K_7As_2W_{17}V_1O_{62}$, and α_2-$K_7As_2W_{17}Nb_1O_{62}$ Wells-Dawson HPAs.

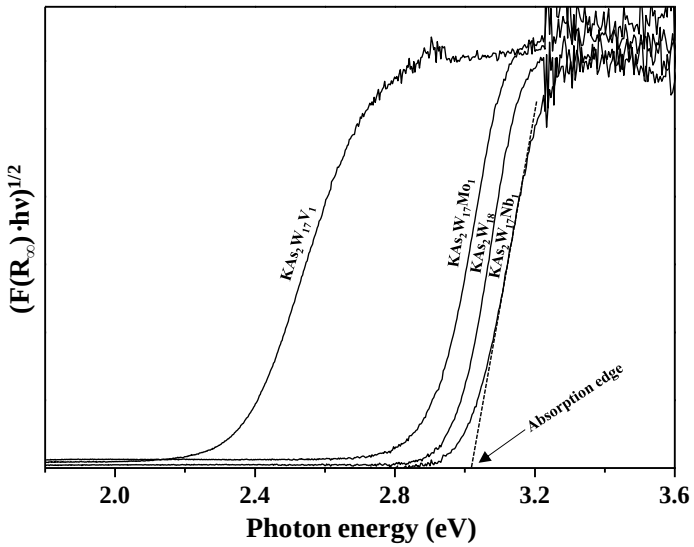

Fig. 3.35. $[F(R_\infty)\cdot h\nu]^{1/2}$ curves of α-$K_6As_2W_{18}O_{62}$, α_2-$K_6As_2W_{17}Mo_1O_{62}$, α_2-$K_7As_2W_{17}V_1O_{62}$, and α_2-$K_7As_2W_{17}Nb_1O_{62}$ Wells-Dawson HPAs.

Table. 3.14.

First electron reduction potentials and absorption edge energies of α-$K_6As_2W_{18}O_{62}$, α_2-$K_6As_2W_{17}Mo_1O_{62}$, α_2-$K_7As_2W_{17}V_1O_{62}$, and α_2-$K_7As_2W_{17}Nb_1O_{62}$ Wells-Dawson HPAs.

Catalyst	1^{st} electron reduction potential (volts vs. SCE)	UV-visible absorption edge energy (eV)
KAs_2W_{18}	+0.049	2.97
$KAs_2W_{17}Mo_1$	+0.243	2.90
$KAs_2W_{17}V_1$	+0.378	2.36
$KAs_2W_{17}Nb_1$	-0.162	3.01

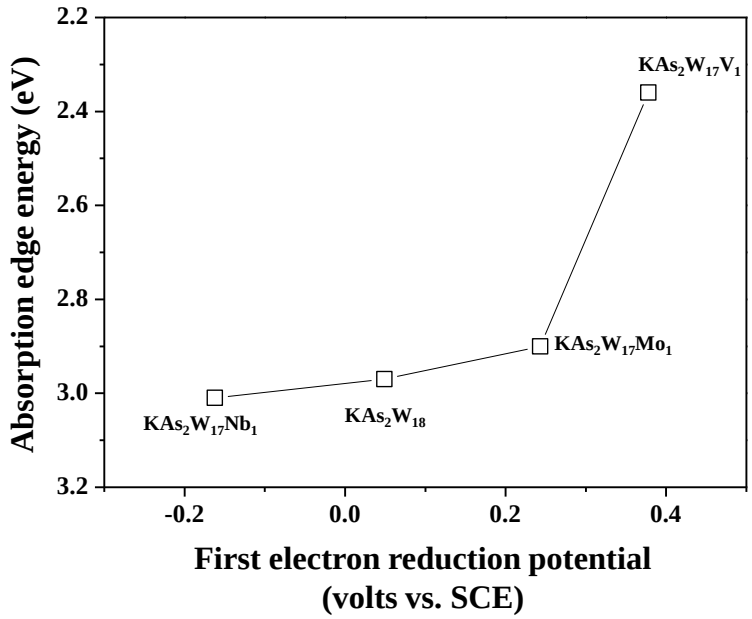

Fig. 3.36. Absorption edge energy plotted as a function of reduction potential.

3.5.3. Catalytic test

Gas-phase oxidative dehydrogenation of benzylamine was carried out over α-$K_6As_2W_{18}O_{62}$, α_2-$K_6As_2W_{17}Mo_1O_{62}$, α_2-$K_7As_2W_{17}V_1O_{62}$, and α_2-$K_7As_2W_{17}Nb_1O_{62}$ Wells-Dawson HPAs. The catalysts exhibited a stable catalytic performance during a 5 h-reaction. In this work, dibenzylimine was mainly formed and trace amounts of benzonitrile and benzaldehyde were detected. None of them was detected without oxygen, indicating that dibenzylimine, benzonitrile, benzaldehyde is formed via oxidative dehydrogenation reaction. Figure 3.37 shows the catalytic performance of α_2-$K_7As_2W_{17}V_1O_{62}$ during the 5 h-reaction and yield for dibenzylimine after a 5 h-reaction. Yield for dibenzylimine increased in the order of α_2-$K_7P_2W_{17}Nb_1O_{62}$ < α-$K_6P_2W_{18}O_{62}$ < $K_6P_2W_{17}Mo_1O_{62}$ < α_2-$K_7P_2W_{17}V_1O_{62}$.

When considering the fact that vanadium center is easier to be reduced than other metal centers in the electrochemical measurement, it is inferred that vanadium-substitution provided efficient active sites for oxidative dehydrogenation by contributing to the density of accessible electronic states (unoccupied orbitals) in the Wells-Dawson tungstoarsenate frameworks. This result suggests that reducibility of the metal centers in the Wells-Dawson tungstoarsenate frameworks plays an important role in the oxidative dehydrogenation reaction of benzylamine. Interestingly, metal-substitution (as addenda atom) showed the similar effect on the redox properties and the catalytic activity, even in a different series of HPAs.

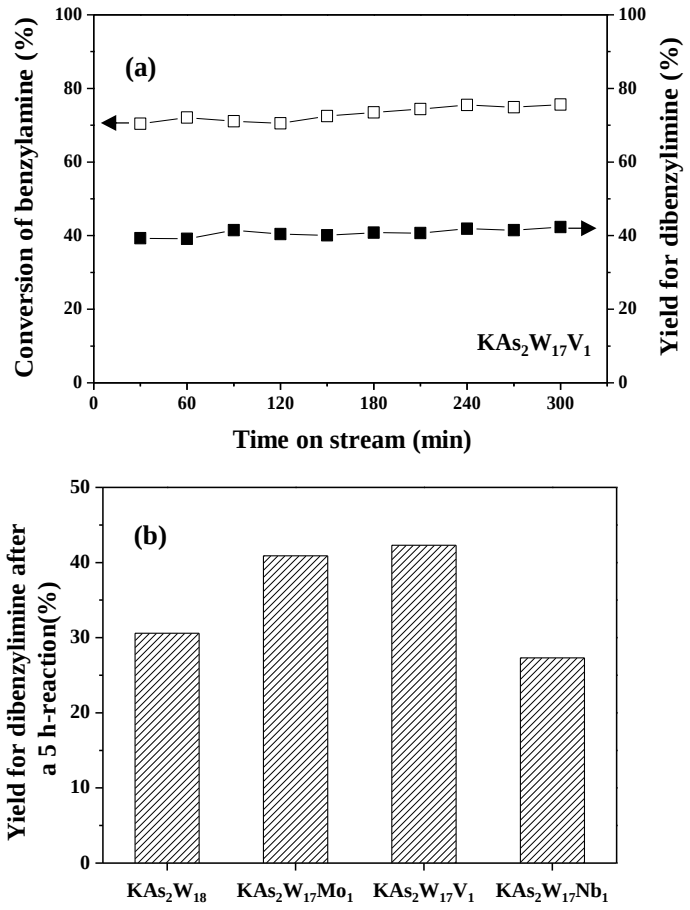

Fig. 3.37. (a) Catalytic performance of α_2-$K_7As_2W_{17}V_1O_{62}$ during the 5 h-reaction and (b) yield for dibenzylimine after a 5 h-reaction.

Chapter 4. Conclusions

In this work, several series of transition metal-substituted HPA catalysts with different addenda atoms, central atoms, contents, and structures were designed and synthesized in order to elucidate the catalytic redox properties and catalytic activities in oxidation catalysis. They were investigated by several experimental techniques including electrochemical analysis, UV-visible spectroscopy, and scanning tunneling microscopy (STM) in order to elucidate the relationship between electronic structure and redox properties. Furthermore, the reliabilities of absorption edge energy and negative differential resistance (NDR) peak voltage determined by UV-visible spectroscopy and scanning tunneling microscopy, respectively, were also examined as alternative parameters for the redox property.

In molybdenum-substituted $H_6P_2W_{18-x}Mo_xO_{62}$ (x=0, 3, 9, 15, 18) Wells-Dawson HPAs, molybdenum-substituted Wells-Dawson HPAs showed an additional molybdenum-based redox transition at more positive potential. First electron reduction potentials increased with increasing molybdenum-substitution. Absorption edge energy determined from the linear fit of $[F(R_\infty)\cdot h\nu]^{1/2}$ decreased with increasing molybdenum content. In STM measurements, two-dimensional self-assembled HPA arrays were observed. Tunneling spectra taken at bright corrugations showed a distinctive current-voltage responses, referred to as negative differential resistance (NDR) phenomenon. NDR peak voltage appeared at less negative voltage with increasing the molybdenum content. In case of Wells-Dawson tungstophosphate, added electrons are generally delocalized over

twelve tungsten centers at equatorial sites. In case of molybdenum-substituted heteropolyanion, however, the energy of metal centers at cap sites is stabilized by more reducible molybdenum and the electrochemical reduction of molybdenum centers at cap sites would be available. Among the investigated, $H_6P_2Mo_{18}O_{62}$ showed the highest reduction potential and the smallest energy gap. It is inferred that the most stabilized energy level of the LUMO in the $H_6P_2Mo_{18}O_{62}$, due to the contribution of reducible molybdenum metal centers, provided the electrochemically accessible metal centers and resulted in the highest reduction potential. Gas-phase oxidative dehydrogenation of ethanol to acetaldehyde was carried out as a model reaction to probe oxidation catalysis of $H_6P_2W_{18-x}Mo_xO_{62}$ (x=0, 3, 9, 15, 18) Wells-Dawson HPAs. Yield for acetaldehyde (oxidation product) increased with increasing molybdenum content. Among the tested catalysts, $H_6P_2Mo_{18}O_{62}$ with the highest reduction potential showed the best catalytic performance. Molybdenum-substitution provided efficient active sites for oxidative dehydrogenation by contributing to the density of accessible electronic states (unoccupied orbitals). The results suggests that reducibility of the metal centers in the Wells-Dawson tungstophosphate frameworks plays an important role in the oxidative dehydrogenation of ethanol.

Group 5 metal (V and Nb)-substituted Wells-Dawson tungstophosphates were synthesized via direct incorporation of transition metal into the mono-lacunary species to yield the selectively-substituted structures. In the electrochemical analysis, vanadium-substituted Wells-Dawson tungstophosphates showed an additional vanadium-based redox transitions at more positive potential. However, niobium-substituted Wells-Dawson tungstophosphates showed significantly shifted redox transitions. First electron

reduction potential increased in the order of α_2-$K_7P_2W_{17}Nb_1O_{62}$ < α-$K_6P_2W_{18}O_{62}$ < α_2-$K_6P_2W_{17}Mo_1O_{62}$ < α_2-$K_7P_2W_{17}V_1O_{62}$. Absorption edge energy determined by UV-visible spectroscopy decreased in the order of α_2-$K_7P_2W_{17}Nb_1O_{62}$ > α-$K_6P_2W_{18}O_{62}$ > α_2-$K_6P_2W_{17}Mo_1O_{62}$ > α_2-$K_7P_2W_{17}V_1O_{62}$. The trend of NDR peak voltage was also well consistent with that of absorption edge energy. It is inferred that the energy level of metal centers at cap sites was stabilized by more reducible vanadium which largely contributes and stabilizes the LUMO and the electrochemical reduction of vanadium centers at cap sites would be available. Therefore, electrochemically added electrons are preferentially localized on the vanadium center. Otherwise, niobium center shows the greater predisposition than vanadium center to lose its electrons (hard to be reduced). In case of α_2-$K_7P_2W_{17}Nb_1O_{62}$, niobium center could not stabilize but elevate the energy level of metal centers. Gas-phase oxidative dehydrogenation of benzylamine was carried out as a model reaction to probe oxidation catalysis. Yield for dibenzylimine (oxidation product) increased in the order of α_2-$K_7P_2W_{17}Nb_1O_{62}$ < α-$K_6P_2W_{18}O_{62}$ < α_2-$K_6P_2W_{17}Mo_1O_{62}$ < α_2-$K_7P_2W_{17}V_1O_{62}$.

Heteropolytungstates with different central atom, α-$H_nXW_{12}O_{40}$ ($X=Co^{2+}$, B^{3+}, Si^{4+}, and P^{5+}) Keggin HPAs were prepared to elucidate the effect of central atom on the redox properties and catalytic activity. All α-$H_nXW_{12}O_{40}$ HPA catalysts exhibited well-defined reversible and stepwise tungsten-centered redox transitions during the electrochemical measurements. First electron reduction potential increased in the order of α-$H_6CoW_{12}O_{40}$ < α-$H_5BW_{12}O_{40}$ < α-$H_4SiW_{12}O_{40}$ < α-$H_3PW_{12}O_{40}$ catalysts. Absorption edge energy determined by UV-visible spectroscopy decreased in the order of α-$H_6CoW_{12}O_{40}$ > α-$H_5BW_{12}O_{40}$ > α-$H_4SiW_{12}O_{40}$ > α-$H_3PW_{12}O_{40}$ catalysts. The trend of NDR peak

voltage was also well consistent with that of absorption edge energy. Keggin-type heteropolyanion with larger negative charge and smaller size resulted in poor reducibility of heteropolyanion due to the smaller capacity to accept electrons. Among the tested, PO_4^{3-} anion with smaller negative charge and lager size is the most effective to enhance the reducibility.

Another heteropolytungstates containing AsO_4^{3-} as a central unit were also examined. The series of α-$K_6As_2W_{18-x}Mo_xO_{62}$ (x=0-3) Wells-Dawson HPAs were prepared via direct incorporation of transition metal into the mono-, di-, and tri-lacunary species. In electrochemical analysis, α-$K_6As_2W_{18}O_{62}$ exhibited four tungsten-centered redox transitions. However, molybdenum-substituted α-$K_6As_2W_{18-x}Mo_xO_{62}$ (x=1-3) exhibited an additional molybdenum-centered redox transition at more positive potential. First electron reduction potential increased with increasing molybdenum content. Absorption edge energy decreased with increasing molybdenum content. NDR peak voltage appeared at less negative voltage with increasing molybdenum content. These results are well consistent with the results in the series of $H_6P_2W_{18-x}Mo_xO_{62}$ (x=0, 3, 9, 15, 18). Gas-phase oxidative dehydrogenation of benzyl alcohol was carried out as a model reaction to track the oxidation catalysis. Yield for benzaldehyde (oxidation product) increased with increasing molybdenum content.

Furthermore, group 5 metal-substituted α_2-$K_7As_2W_{17}V_1O_{62}$ and α_2-$K_7As_2W_{17}Nb_1O_{62}$ Wells-Dawson HPAs were examined. In the electrochemical analysis, vanadium-substituted Wells-Dawson tungstoarsenates showed additional vanadium-centered redox transitions at more positive potential. However, niobium-substituted Wells-Dawson tungstoarsenates showed significantly shifted redox transitions. First electron reduction potential increased

in the order of α_2-$K_7As_2W_{17}Nb_1O_{62}$ < α-$K_6As_2W_{18}O_{62}$ < α_2-$K_6As_2W_{17}Mo_1O_{62}$ < α_2-$K_7As_2W_{17}V_1O_{62}$. Absorption edge energy determined by UV-visible spectroscopy decreased in the order of α_2-$K_7As_2W_{17}Nb_1O_{62}$ > α-$K_6As_2W_{18}O_{62}$ > α_2-$K_6As_2W_{17}Mo_1O_{62}$ > α_2-$K_7As_2W_{17}V_1O_{62}$. Gas-phase oxidative dehydrogenation of benzylamine was carried out as a model reaction to track the oxidation catalysis. Yield for dibenzylimine (oxidation product) increased in the order of α_2-$K_7As_2W_{17}Nb_1O_{62}$ < α-$K_6As_2W_{18}O_{62}$ < α_2-$K_6As_2W_{17}Mo_1O_{62}$ < α_2-$K_7As_2W_{17}V_1O_{62}$.

From the results, it was found that redox properties of HPAs could be altered by changing the constituent elements, compositions, or structures. It could be concluded that redox properties of HPAs, which are closely related to the electronic structure, play an important role to determine the catalytic activities in the oxidative dehydrogenation reactions. Furthermore, it was successfully demonstrated that absorption edge energy and NDR peak voltage can be utilized as alternative parameters to estimate the reducibility of HPAs.

Bibliography

[1] T. Okuhara, N. Mizuno, M. Misono, "Catalytic chemistry of heteropoly compounds", *Adv. Catal.* 41 (1995) 113.

[2] B. Dawson, "The structure of the 9 (18)-heteropolyanion in potassium 9 (18)-tungstophosphate, $K_6(P_2W_{18}O_{62})\cdot 14H_2O$", *Acta. Cryst.* 6 (1953) 113.

[3] R.G. Finke, M. Droege, J.R. Hutchinson, O. Gansow, "Trivacant heteropolytungstate derivatives: the rational synthesis, characterization, and tungsten-^{183}W NMR spectra of $P_2W_{18}M_4(H_2O)_2O_{68}^{10-}$ (M = Co, Cu, Zn)", *J. Am. Chem. Soc.* 103 (1981) 1587.

[4] C. Preyssler, "Existence of 18-tungsto-3-phosphate", *Bull. Soc. Chim. Fr* (1970) 30.

[5] D.E. Katsoulis, "A survey of applications of polyoxometalates", *Chem. Rev.* 98 (1998) 359.

[6] E. Drechsel, "Simple methods for the preparation of some inorganic acids", *Ber.* 20 (1887) 1452.

[7] S.R. Matkovic, G.M. Valle, L.E. Briand, "Optimization of the operative conditions for heteropolyacids synthesis through ion exchange", *Mater. Res.* 8 (2005) 351.

[8] M. Misono, I. Ono, G. Koyano, A. Aoshima, "Heteropolyacids. Versatile green catalysts usable in a variety of reaction media", *Pure Appl. Chem.* 72 (2000) 1305.

[9] K. Eguchi, N. Yamazoe, T. Seiyama, "Thermal Behavior of 12-Molybdophosphates", *Nippon Kagaku Kaishi* (1981) 336.

[10] L.E. Briand, G.T. Baronetti, H.J. Thomas, “The state of the art on Wells–Dawson heteropoly-compounds. A review of their properties and applications”, *Appl. Catal. A: Gen.* 256 (2003) 37.

[11] J.J. Borrás-Almenar, E. Coronado, A. Müller, M.T. Pope, “Polyoxometalate molecular science”, Springer (2003).

[12] K. Katamura, T. Nakamura, K. Sakata, M. Misono, Y. Yoneda, “Reduction mechanism of 12-molybdo-and 12-tungstophosphoric acids in the solid state”, *Chem. Lett*. (1981) 89.

[13] B. Keita, Y.W. Lu, L. Nadjo, R. Contant, M. Abbessi, J. Canny, M. Richet, “Electrochemical and catalytic behaviour of Dawson-type complexes derived from [(1), 2, 3-$P_2Mo_2W_{15}O_{61}$]$^{10-}$ and first transition metal ions”, *J. Electroanal. Chem.* 477 (1999) 146.

[14] E. Papaconstantinou, “Photochemistry of polyoxometalates of molybdenum and tungsten and/or vanadium”, *Chem. Soc. Rev.* 18 (1989) 1.

[15] A.M. Khenkin, R. Neumann, “Mixed-addenda vanadium-substituted polyfluorooxometalates: synthesis, characterization, and catalytic aerobic oxidation”, *Inorg. Chem.* 39 (2000) 3455.

[16] C. Comuzzi, G. Dolcetti, A. Trovarelli, F. Cavani, F. Trifiró, J. Llorca, R.G. Finke, “The solid-state rearrangement of the Wells-Dawson $K_6P_2W_{18}O_{62}\cdot 10H_2O$ to a stable Keggin-type heteropolyanion phase: a catalyst for the selective oxidation of isobutane to isobutene”, *Catal. Lett*. 36 (1996) 75.

[17] T. Wijesekera, J.E. Lyons, P.E. Ellis Jr., “Wells-Dawson type heteropolyacids, their preparation and use as oxidation catalysts”, Patent WO 00/09262 (2000).

[18] L.E. Briand, H.J. Thomas, G.T. Baronetti, “Thermal stability and catalytic activity of Wells-Dawson tungsten heteropoly salts”, *Appl. Catal. A : Gen.*, 201 (2000) 191.

[19] A.M. Khenkin, L. Weiner, Y. Wang, R. Neumann, “Electron and oxygen transfer in polyoxometalate, $H_5PV_2Mo_{10}O_{40}$, catalyzed oxidation of aromatic and alkyl aromatic compounds: evidence for aerobic Mars-van Krevelen-type reactions in the liquid homogeneous phase”, *J. Am. Chem. Soc.* 123 (2001) 8531.

[20] N. Mizuno, J.-S. Min, A. Taguchi, “Preparation and characterization of $Cs_{2.8}H_{1.2}PMo_{11}Fe(H_2O)O_{39}\cdot 6H_2O$ and investigation of effects of iron-substitution on heterogeneous oxidative dehydrogenation of 2-propanol”, *Chem. Mater.* 16 (2004) 2819.

[21] R.S. Weber, “Molecular orbital study of C-H bond breaking during the oxidative dehydrogenation of methanol catalyzed by metal oxide surfaces”, *J. Phys. Chem.* 98 (1994) 2999.

[22] N. Mizuno, K. Katamura, Y. Yoneda, M. Misono, “Catalysis by heteropoly compounds: V. The reduction mechanism of $H_3PMo_{12}O_{40}$”, *J. Catal.* 83 (1983) 384.

[23] F. Jonnevijlle, C.M. Tourné, G.F. Tourné, “Preparation and characterization of heteropolytungstates containing group 3a elements”, *Inorg. Chem.* 21 (1982) 2742.

[24] N. Mizuno, M. Misono, “Heteropolyanions in catalysis”, *J. Mol. Catal.* 86 (1994) 319.

[25] D.R. Park, J.H. Song, S.H. Lee, S.H. Song, H. Kim, J.C. Jung, I.K. Song,

"Redox properties of $H_3PMo_xW_{12-x}O_{40}$ and $H_6P_2Mo_xW_{18-x}O_{62}$ heteropolyacid catalysts and their catalytic activity for benzyl alcohol oxidation", *Appl. Catal. A: Gen*. 349 (2008) 222.

[26] P. Kubelka, F. Munk, "An article on optics of paint layers", *Z. Tech. Phys.* 12 (1931) 593.

[27] D. R. Park, S. Park, Y. Bang, I. K. Song, "Redox property and oxidation catalysis of group 5 metal (V, Nb, Ta)-containing Keggin and Wells-Dawson heteropolyacid (HPA) catalysts", *Appl. Catal. A: Gen.* 373 (2010) 201.

[28] I.-M. Mbomekalle, Y.W. Lu, B. Keita, L. Nadjo, "Simple, high yield and reagent-saving synthesis of pure α-$K_6P_2W_{18}O_{62}\cdot 14H_2O$", *Inorg. Chem. Commun*. 7 (2004) 86.

[29] R. Contant, "18. Potassium octadecatungstodiphosphates (V) and related lacunary compounds", *Inorg. Synth.* 27 (1990) 104.

[30] C. Rocchiccioli-Deltcheff, M. Fournier, R. Franck, R. Thouvenot, "Vibrational investigations of polyoxometalates. 2. Evidence for anion-anion interactions in molybdenum(VI) and tungsten(VI) compounds related to the Keggin structure", *Inorg. Chem.* 22 (1983) 207.

[31] A.L. Nolan. R.C. Burns, G.A. Lawrance, "Oxidation of $[Co^{II}W_{12}O_{40}]^{6-}$ to $[Co^{III}W_{12}O_{40}]^{5-}$ by peroxomonosulfate in strong and weak acid solutions, an example of zero-order kinetics", *J. Chem. Soc., Dalton Trans.* (1988) 3041.

[32] I.K. Song, R.B. Shnitser, J.J. Cowan, C.L. Hill, M.A. Barteau, "Nanoscale characterization of redox and acid properties of Keggin-type heteropolyacids by scanning tunneling microscopy and tunneling spectroscopy: Effect of heteroatom substitution", *Inorg. Chem.* 41 (2002)

1292.

[33] I.M. Mbomekalle, B. Keita, L. Nadjo, R. Contant, N. Belai. M.T. Pope, "Rationalization and improvement of the syntheses of two octadecatungstoarsenates: the novel α-$K_7[H_4AsW_{18}O_{62}]\cdot 18H_2O$ and the well known symmetrical α-$K_6[As_2W_{18}O_{62}]\cdot 14H_2O$", *Inorg. Chim. Acta* 342 (2003) 219.

[34] R. Contant, R. Thouvenot, "Heteropolyanions de type Dawson. 2. Synthèses de polyoxotungstoarsénates lacunaires dérivant de l'octadécatungstodiarsénate. Étude structurale par RMN du tungstène-183 des octadéca(molybdotungstovanado)diarsénates apparéntes", *Can. J. Chem.* 69 (1991) 1498.

[35] P. Villabrille, G. Romanelli, L. Gassa, P. Vázquez, C. Cáceres, "Synthesis and characterization of Fe- and Cu-doped molybdovanadophosphoric acids and their application in catalytic oxidation", *Appl. Catal. A: Gen.* 324 (2007) 69.

[36] K. Chen, A.T. Bell, E. Iglesia, "The relationship between the electronic and redox properties of dispersed metal oxides and their turnover rates in oxidative dehydrogenation reactions", *J. Catal*. 209 (2002) 35.

[37] T. Yamase, "Photo- and electrochromism of polyoxometalates and related materials", *Chem. Rev.* 98 (2011) 307.

[38] X. López, C. Bo, and J.-M. Poblet, "Relative stability in α- and β-Wells-Dawson heteropolyanions: A DFT study of $[P_2M_{18}O_{62}]^{n-}$ (M = W and Mo) and $[P_2W_{15}V_3O_{62}]^{n-}$", *Inorg. Chem.* 42 (2003) 2634.

[39] J. V. Lauritsen, R. T. Vang, and F. Besenbacher, "From atom-resolved scanning tunneling microscopy (STM) studies to the design of new

catalysts", *Catal. Today* 111 (2006) 34.

[40] B.A. Watson, M.A. Barteau, L. Haggerty, A.M. Lenhoff, "Scanning tunneling microscopy and tunneling spectroscopy of ordered hetero- and isopolyanion arrays on graphite", 8 (1992) 1145.

[41] C.B. Gorman, R.L. Carroll, R.R. Fuierer, "Negative differential resistance in patterned electroactive self-assembled monolayers", *Langmuir* 17 (2001) 6923.

[42] F.I. Dalidchik, B.A. Budanov, N.N. Kolchenko, E.M. Balashov, S.A. Kovalevskii, "Resonance tunneling spectroscopy of heteropoly compounds", *J. Exp. Theor. Phys.* 115 (2012) 1068.

[43] J. Bartis, Y. Kunina, M. Blumenstein, L.C. Francesconi, "Preparation and tungsten-183 NMR characterization of $[\alpha\text{-}1\text{-}P_2W_{17}O_{61}]^{10-}$, $[\alpha\text{-}1\text{-}Zn(H_2O)P_2W_{17}O_{61}]^{8-}$, and $[\alpha\text{-}2\text{-}Zn(H_2O)P_2W_{17}O_{61}]^{8-}$", *Inorg. Chem.* 35 (1996) 1497.

[44] X. López, C. Bo, and J.-M. Poblet, "Electronic properties of polyoxometalates: electron and proton affinity of mixed-addenda Keggin and Wells−Dawson anions", *J. Am. Chem. Soc.124* (2002) 12574.

[45] K.T.V. Rao, B. Haribabu, P.S.S. Prasad, N. Lingaiah, "Vapor-phase selective aerobic oxidation of benzylamine to dibenzylimine over silica-supported vanadium-substituted tungstophosphoric acid catalyst", *Green Chem.* 15 (2013) 837.

[46] L. Adamczyk, K. Miecznikowski, "Solid-state electrochemical behavior of Keggin-type borotungstic acid single crystal", *J. Solid State Electrochem.* 17 (2013) 1167.

[47] T. Rajkumar, G.R. Rao, "Synthesis and characterization of hybrid

molecular material prepared by ionic liquid and silicotungstic acid", *Mater. Chem. Phys*. 112 (2008) 853.

[48] B. Keita, Y. Jean, B. Levy, L. Nadjo, and R. Contant, New Journal of Chemistry 26 (2002) 1314.

[49] X. López, J.A. Fernández, J.M. Poblet, "Redox properties of polyoxometalates: new insights on the anion charge effect", *Dalton Trans.* (2006) 1162.

[50] I.-M. Mbomekallé, X. López, J.M. Poblet, F. Sécheresse, B. Keita, L. Nadjo, "Influence of the heteroatom size on the redox potentials of selected polyoxoanions", *Inorg. Chem.* 49 (2010) 7001.

[51] P.S.N. Rao, K.T.V. Rao, P.S.S. Prasad, N. Lingaiah, "The role of vanadium in ammonium salt of heteropoly molybdate supported on niobia for selective oxidation of benzyl alcohol", *Catal. Commun.* 11 (2010) 547.

요 약(국문초록)

헤테로폴리산은 다양한 구조와 조성을 지닌 금속산화물 클러스터이며 고유의 산화환원 특성과 구조 안정성으로 인해 산화반응 및 광촉매적 환원 반응에서 촉매로 널리 이용되고 있다. 헤테로폴리산을 이용한 산화반응은 지속적으로 연구되어 왔으며, 최근에는 배위원소가 치환된 (Mixed-addenda) 헤테로폴리산이 산화촉매로서 주목받고 있다. 헤테로폴리산의 촉매적 특성과 촉매활성은 촉매의 구성원소를 달리함으로써 분자 수준에서 조절할 수 있는 것으로 알려져 있다. 금속, 반금속 또는 비금속 원소들이 구성원소로서 헤테로폴리산 구조 내에 포함될 수 있으며 이에 따라 이론적으로 조합 가능한 헤테로폴리산은 무수히 많다. 이는 헤테로폴리산의 물성분포가 매우 광범위함을 의미하며, 요구에 따라 다양한 물성을 지닌 헤테로폴리산을 설계할 수 있음을 나타낸다.

본 연구에서는 다양한 전이금속이 치환된 헤테로폴리산을 제조하여 조성과 구조가 산화환원 특성 및 산화반응에서의 촉매활성에 미치는 영향을 확인하고자 하였다. 이를 위해 다양한 구조의 헤테로폴리산 촉매를 제조하고 전기화학적 분석, 자외선-가시광선 분광법 및 주사 터널링 현미경을 이용해 분석하였다. 특히, 자외선-가시광선 분광법으로 측정되는 흡수단 에너지 (Absorption edge energy) 및 주사 터널링 현미경으로 측정되는 NDR (Negative differential

resistance) 전압과 산화환원 특성 간의 상관관계를 분석하였다.

먼저, 서로 다른 조성으로 몰리브데넘이 치환된 Wells-Dawson형 $H_6P_2W_{18-x}Mo_xO_{62}$ (x=0, 3, 9, 15, 18) 헤테로폴리산을 “Etherate 제조법”으로 제조하고 몰리브데넘 치환이 Wells-Dawson형 텅스토인산의 산화환원 특성과 촉매활성에 미치는 영향을 확인하고자 하였다. 순환전압전류법을 통해 $H_6P_2W_{18}O_{62}$ 헤테로폴리산 촉매가 텅스텐 기반의 산화환원쌍을 보임을 확인하였다. 반면 $H_6P_2Mo_{18}O_{62}$ 헤테로폴리산 촉매는 몰리브데넘 기반의 산화환원쌍을 나타내었다. 흥미롭게도 몰리브데넘이 일부 치환된 다른 촉매들에서는 $H_6P_2W_{18}O_{62}$ 헤테로폴리산과 비교해 몰리브데넘 기반의 산화환원쌍이 추가적으로 관찰되었다. 환원전위는 헤테로폴리산 내 몰리브데넘 함량이 증가함에 따라 증가하였다. 헤테로폴리산의 전자구조를 확인하기 위해 자외선-가시광선 분광법을 수행하였으며 이로부터 측정된 흡수단 에너지는 몰리브데넘 함량이 증가함에 따라 감소하였다. 추가적인 표면의 국부적 전자구조 분석을 위해 주사 터널링 현미경을 이용하였다. 주사 터널링 현미경을 통해 얻어진 이미지를 통해 단순한 물리적 증착을 통해서도 헤테로폴리산이 그래파이트 상에서 정렬된 2차원 구조를 형성함을 확인하였다. 이미지의 밝은 부분에서 측정한 투과 스펙트럼에서는 NDR 현상이 관찰되었으며, NDR 전압은 몰리브데넘 함량이 증가함에 따라 증가하였다. 최종적으로 산화반응에서의 촉매활성을 확인하기 위해 에탄올의 산화적 탈수소화 반응을 수행하였다. 아세트알데히드 수율은 몰리브데넘 함량이

증가함에 따라 증가하였으며 모든 촉매 중에서 가장 높은 환원전위값을 보인 $H_6P_2Mo_{18}O_{62}$ 헤테폴리산 촉매가 가장 높은 알세트알데히드 수율을 나타내었다.

추가적으로 5족 금속이 치환된 Wells-Dawson형 α_2-$K_7P_2W_{17}V_1O_{62}$ 및 α_2-$K_7P_2W_{17}Nb_1O_{62}$ 헤테로폴리산을 제조하고 5족 금속 치환이 Wells-Dawson형 텅스토인산의 산화환원 특성과 촉매활성에 미치는 영향을 확인하고자 하였다. 해당 촉매는 금속의 선택적 치환을 위해 Lacunary 화합물을 이용하여 제조하였다. α-$K_6P_2W_{18}O_{62}$ 및 α_2-$K_7P_2W_{17}Mo_1O_{62}$ 헤테로폴리산 또한 대조군으로 제조하였다. 순환전압전류법을 통해 α_2-$K_7P_2W_{17}V_1O_{62}$ 및 α_2-$K_7P_2W_{17}Mo_1O_{62}$ 헤테로폴리산에서는 α-$K_6P_2W_{18}O_6$ 헤테로폴리산과 비교해 추가적인 바나듐 및 몰리브데넘 기반의 산화환원쌍이 나타남을 확인하였다. 반면, α_2-$K_7P_2W_{17}Nb_1O_{62}$ 에서는 추가적인 산화환원쌍이 나타나지 않고 텅스텐 기반의 산화환원쌍이 음전압쪽으로 크게 이동함을 확인하였다. 전기화학적 분석을 통해 측정된 환원전위는 α_2-$K_7P_2W_{17}Nb_1O_{62}$ < α-$K_6P_2W_{18}O_{62}$ < α_2-$K_6P_2W_{17}Mo_1O_{62}$ < α_2-$K_7P_2W_{17}V_1O_{62}$ 순으로 증가하였다. 자외선-가시광선 분광법으로 측정된 흡수단 에너지는 α_2-$K_7P_2W_{17}Nb_1O_{62}$ > α-$K_6P_2W_{18}O_{62}$ > α_2-$K_6P_2W_{17}Mo_1O_{62}$ > α_2-$K_7P_2W_{17}V_1O_{62}$ 순으로 감소하였다. 주사 터널링 현미경을 통해 얻어진 이미지를 통해 해당 촉매들이 그래파이트 표면에서 정렬된 2차원 구조를 형성함을 확인하였다. 측정된 NDR 전압은 α_2-$K_7P_2W_{17}Nb_1O_{62}$ < α-$K_6P_2W_{18}O_{62}$ < α_2-$K_6P_2W_{17}Mo_1O_{62}$ < α_2-$K_7P_2W_{17}V_1O_{62}$ 순서로 증가하였다.

해당 촉매의 산화반응에서의 촉매활성을 확인하기 위해 벤질아민의 산화적 탈수소화 반응을 수행하였으며, 디벤질이민의 수율은 α_2-$K_7P_2W_{17}Nb_1O_{62}$ < α-$K_6P_2W_{18}O_{62}$ < α_2-$K_6P_2W_{17}Mo_1O_{62}$ < α_2-$K_7P_2W_{17}V_1O_{62}$ 순서로 증가하였다.

서로 다른 중심원소가 산화환원 특성에 미치는 영향을 확인하기 위해 Keggin형 α-$H_nXW_{12}O_{40}$ (X=Co^{2+}, B^{3+}, Si^{4+}, and P^{5+}) 헤테로폴리산을 제조하였다. 모든 촉매의 순환전류전압 곡선에서 가역적 · 순차적인 텅스텐 기반의 산화환원쌍이 관찰되었다. 환원전위는 α-$H_6CoW_{12}O_{40}$ < α-$H_5BW_{12}O_{40}$ < α-$H_4SiW_{12}O_{40}$ < α-$H_3PW_{12}O_{40}$ 순으로 증가하였다. 자외선-가시광선 분광법으로 측정된 흡수단 에너지는 α-$H_6CoW_{12}O_{40}$ > α-$H_5BW_{12}O_{40}$ > α-$H_4SiW_{12}O_{40}$ > α-$H_3PW_{12}O_{40}$ 순으로 감소 하였다. 이러한 경향은 주사 터널링 현미경 분석을 통해 얻어진 NDR 전압에서도 유사하게 관찰되었다. 상대적으로 큰 사이즈와 낮은 전하를 지닌 PO_4^{3-} 음이온이 촉매의 환원력을 높이는데 효과적인 것으로 나타났다.

또 다른 3가의 AsO_4^{3-} 음이온이 중심 금속으로 포함된 Wells-Dawson형 텅스토비소산에서 전이금속의 치환이 산화환원 특성과 촉매활성에 미치는 영향을 확인하고자 하였다. 이를 위해 서로 다른 조성으로 몰리브데넘이 치환된 Wells-Dawson형 α-$K_6As_2W_{18-x}Mo_xO_{62}$ (x=0-3) 헤테로폴리산을 제조하였다. 순환전압전류 곡선에서 α-$K_6As_2W_{18}O_{62}$가 텅스텐 기반의 산화환원쌍을 나타내는 반면, 몰리브데넘이 치환된 Wells-Dawson형 텅스토비소산에서는 추가적인 몰리브데넘 기반의 산화환원쌍이 관찰되었다. Wells-Dawson형

텅스토인산의 결과와 매우 유사하게, 환원전위는 헤테로폴리산 내 몰리브데넘 함량이 증가함에 따라 증가하였다. 자외선-가시광선 분광법으로 측정된 흡수단 에너지는 몰리브데넘 함량이 증가함에 따라 감소하였다. NDR 전압은 몰리브데넘 함량이 증가함에 따라 증가하였다. 해당 촉매의 산화반응에서의 촉매활성을 확인하기 위해 벤질알코올의 산화적 탈수소화 반응을 수행하였으며, 벤잘데히드 수율은 몰리브데넘 함량이 증가함에 따라 증가하였다.

마지막으로 5족 금속이 Wells-Dawson형 텅스토비소산의 산화환원 특성과 촉매활성에 미치는 영향을 확인하고자 α_2-$K_7As_2W_{17}V_1O_{62}$ 및 α_2-$K_7As_2W_{17}Nb_1O_{62}$ 헤테로폴리산을 제조하였다. α-$K_6As_2W_{18}O_{62}$ 및 α_2-$K_6As_2W_{17}Mo_1O_{62}$ 헤테로폴리산 또한 대조군으로 제조하였다. 순환전압전류법을 통해 α_2-$K_7As_2W_{17}V_1O_{62}$ 및 α_2-$K_7As_2W_{17}Mo_1O_{62}$ 헤테로폴리산에서는 α-$K_6As_2W_{18}O_{62}$ 헤테로폴리산과 비교해 추가적인 바나듐 및 몰리브데넘 기반의 산화환원쌍이 나타남을 확인하였다. 반면, α_2-$K_7As_2W_{17}Nb_1O_{62}$에서는 추가적인 산화환원쌍이 관찰되지 않고 텅스텐 기반의 산화환원쌍이 음전압 영역으로 크게 이동함을 확인하였다. 환원전위는 α_2-$K_7As_2W_{17}Nb_1O_{62}$ < α-$K_6As_2W_{18}O_{62}$ < α_2-$K_6As_2W_{17}Mo_1O_{62}$ < α_2-$K_7As_2W_{17}V_1O_{62}$ 순으로 증가하였다. 자외선-가시광선 분광법으로 측정된 흡수단 에너지는 α_2-$K_7As_2W_{17}Nb_1O_{62}$ > α-$K_6As_2W_{18}O_{62}$ > α_2-$K_6As_2W_{17}Mo_1O_{62}$ > α_2-$K_7As_2W_{17}V_1O_{62}$ 순으로 감소하였다. 해당 촉매의 산화반응에서의 촉매활성을 확인하기 위해 벤질아민의 산화적 탈수소화 반응을 수행하였으며,

디벤질이민의 수율은 α_2-$K_7As_2W_{17}Nb_1O_{62}$ < α-$K_6As_2W_{18}O_{62}$ < α_2-$K_6As_2W_{17}Mo_1O_{62}$ < α_2-$K_7As_2W_{17}V_1O_{62}$ 순서로 증가하였다.

본 연구에서는 다양한 배위원소, 중심원소, 조성 및 구조를 지니는 헤테로폴리산의 제조, 분석 및 모델 산화반응으로의 적용을 통해 산화환원 특성과 산화촉매 반응을 이해하고자 하였다. 본 연구를 통해 헤테로폴리산 촉매의 산화환원 특성은 분자 내 구성성분을 달리함에 따라 쉽게 변화하는 것으로 나타났다. 특히, 헤테로폴리산 촉매의 산화환원 특성은 전자구조와 밀접한 연관성을 가지고 있는 것으로 판단할 수 있었으며, 산화반응에서의 촉매활성을 결정하는 중요한 특성임을 확인하였다. 또한 흡수단 에너지와 NDR 전압은 촉매의 환원력을 측정하기 위한 상호보완적 수치로서 이용될 수 있음을 확인하였다.

주요어: 헤테로폴리산, 전이 금속, 산화환원 특성, 산화반응, 전자구조

학 번: 2010-21019

List of publications

Papers

International papers published (First author)

1. **J.H. Choi**, T.H. Kang, Y. Bang, J.H. Song, I.K. Song, "Electrochemical and UV-visible Spectroscopy Studies of $K_6As_2W_{18-x}Mo_xO_{62}$ (x=0-3) Wells-Dawson Heteropolyacid Catalysts for Oxidative Dehydrogenation of Benzyl Alcohol", *Catalysis Communications*, 50, pp.29-33 (2014)

2. **J.H. Choi**, T.H. Kang, Y. Bang, J. Yoo, J.O. Jun, I.K. Song, "STM Investigation of Nano-structured α-$K_5PW_{11}O_{39}(M{\cdot}OH_2)$ (M = Mn^{II}, Co^{II}, Ni^{II}, and Zn^{II}) Heteropolyacid Catalyst Monolayers", *Journal of Nanoscience and Nanotechnology* (In Press).

3. **J.H. Choi**, T.H. Kang, J.H. Song, Y. Bang, I.K. Song, "Redox Behavior and Oxidation Catalysis of $H_nXW_{12}O_{40}$ (X=Co^{2+}, B^{3+}, Si^{4+}, and P^{5+}) Keggin Heteropolyacid Catalysts", *Catalysis Communications*, 43, pp.155-158 (2014).

4. **J.H. Choi**, Y.J. Lee, T.H. Kang, Y. Bang, J.H. Song, J.C. Jung, I.K. Song, "Redox Properties of α_2-$K_8P_2W_{17}(M{\cdot}OH_2)O_{61}$ (M=Mn^{II}, Zn^{II}, Fe^{II}, Co^{II}, and Ni^{II}) Wells-Dawson Heteropolyacids Probed by Scanning Tunneling Microscopy and Tunneling Spectroscopy", *Catalysis Communications*, 39, pp.60-64 (2013).

5. **J.H. Choi**, J.K. Kim, D.R. Park, T.H. Kang, J.H. Song, I.K. Song, "Redox Properties and Oxidation Catalysis of Transition Metal-substituted α-$K_5PW_{11}O_{39}(M{\cdot}OH_2)$ (M = Mn^{II}, Co^{II}, Ni^{II}, and Zn^{II}) Keggin Heteropolyacid Catalysts for Liquid-phase Oxidation of 2-Propanol", *Journal of Molecular*

Catalysis A: Chemical, 371, pp.111-117 (2013).

6. **J.H. Choi**, J.K. Kim, S. Park, J.H. Song, I.K. Song, "Redox Properties and Oxidation Catalysis of Potassium Salts of Transition Metal-substituted α_2-$K_8P_2W_{17}O_{61}(M{\cdot}OH_2)$ (M = Mn^{II}, Zn^{II}, Fe^{II}, Co^{II}, Cu^{II}, and Ni^{II}) Wells-Dawson Heteropolyacids", *Applied Catalysis A: General*, 427-428, pp.79-84 (2012).

7. **J.H. Choi**, D.R. Park, S. Park, I.K. Song, "Scanning Tunneling Microscopy Study of Nano-structured Polyatom-substituted $H_4PW_{11}M_1O_{40}$ Keggin and $H_7P_2W_{17}M_1O_{62}$ (M=Nb, Ta) Wells-Dawson Heteropolyacid Catalysts", *Journal of Nanoscience and Nanotechnology*, 12(7), pp.5864-5869 (2012).

8. **J.H. Choi**, J.K. Kim, D.R. Park, S. Park, J. Yi, I.K. Song, "Etherification of n-Butanol to Di-n-butyl Ether over $H_3PMo_{12-x}W_xO_{40}$ (x=0, 3, 6, 9, 12) Keggin and $H_6P_2Mo_{18-x}W_xO_{62}$ (x=0, 3, 9, 15, 18) Wells-Dawson Heteropolyacid Catalysts", *Catalysis Communications*, 14(1), pp.48-51 (2011).

9. **J.H. Choi**, D.R. Park, S. Park, I.K. Song, "Scanning Tunneling Microscopy and Tunneling Spectroscopy Studies of Niobium-containing $H_{6+x}P_2W_{18-x}Nb_xO_{62}$ (x=0, 1, 2, 3) Wells-Dawson Heteropolyacid Catalysts to Probe Their Redox Property and Oxidation Catalysis", *Korean Journal of Chemical Engineering*, 28(11), pp.2137-2141 (2011).

10. **J.H. Choi**, D.R. Park, S. Park, I.K. Song, "Nano-structured $H_{3+x}PW_{12-x}Nb_xO_{40}$ (x=0-3) Keggin Heteropolyacid Catalysts", *Journal of Nanoscience and Nanotechnology*, 11(9), pp.7870-7875 (2011).

11. **J.H. Choi**, D.R. Park, S. Park, I.K. Song, "Scanning Tunneling Microscopy Study of $H_{6+x}P_2Mo_{18-x}V_xO_{62}$ (x = 0-3) Wells-Dawson Heteropolyacid Catalysts: Correlation of NDR Peak Voltage with Reduction Potential and Oxidation Catalysis", *Catalysis Letters*, 141(6), pp.826-832 (2011).

12. **J.H. Choi**, D.R. Park, S. Park, I.K. Song, "Scanning Tunneling Microscopy and Tunneling Spectroscopy of Nano-structured $H_6P_2Mo_xW_{18-x}O_{62}$ (x=0, 3, 9, 15, 18) Wells-Dawson Heteropolyacids", *Journal of Nanoscience and Nanotechnology*, 11(7), pp.6533-6528 (2011).

International papers published (Co-author)

1. T.H. Kang, **J.H. Choi**, Y. Bang, J. Yoo, J.H. Song, W. Joe, J.S. Choi, I.K. Song, "Dehydration of Glycerin to Acrolein over $H_3PW_{12}O_{40}$ Heteropolyacid Catalyst Supported on Silica-alumina", *Journal of Molecular Catalysis A: Chemical* (In Press).

2. K.H. Kang, U.G. Hong, J.O. Jun, J.H. Song, Y. Bang, **J.H. Choi**, S.J. Han, I.K. Song, "Hydrogenation of Succinic Acid to γ-Butyrolactone and 1,4-Butanediol over Mesoporous Rhenium-copper-carbon Composite Catalyst", *Journal of Molecular Catalysis A: Chemical*, 395, pp.234-242 (2014).

3. S.J. Han, Y. Bang, J. Yoo, S. Park, K.H. Kang, **J.H. Choi**, J.H. Song, I.K. Song, "Hydrogen Production by Steam Reforming of Ethanol over P123-assisted Mesoporous Ni-Al_2O_3-ZrO_2 Xerogel Catalysts", *International Journal of Hydrogen Energy*, 39(20), pp.10445-10453 (2014).

4. J.K. Kim, H.W. Park, U.G. Hong, **J.H. Choi**, I.K. Song, "$Cs_xH_{3.0-x}PW_{12}O_{40}$ (X=2.0-3.0) Heteropolyacid Nano-catalysts for Catalytic Decomposition of 2,3-Dihydrobenzofuran to Aromatics", *Journal of Nanoscience and Nanotechnology* (In Press).

5. Y. Bang, S.J. Han, J. Yoo, S. Park, **J.H. Choi**, Y.J. Lee, J.H. Song, I.K. Song, "Hydrogen Production by Steam Reforming of Liquefied Natural Gas (LNG)

over Mesoporous Nickel-phosphorus-alumina Aerogel Catalyst", *International Journal of Hydrogen Energy*, 39(10), pp.4909-4916 (2014).

6. Y. Bang, S.J. Han, J. Yoo, **J.H. Choi**, J.K. Lee, J.H. Song, J. Lee, I.K. Song, "Hydrogen Production by Steam Reforming of Simulated Liquefied Natural Gas (LNG) over Nickel Catalyst Supported on Mesoporous Phosphorus-modified Alumina Xerogel", *Applied Catalysis B: Environmental*, 148-149, pp.269-280 (2014).

7. Y. Bang, S.J. Han, J. Yoo, **J.H. Choi**, K.H. Kang, J.H. Song, J.G. Seo, J.C. Jung, I.K. Song, "Hydrogen Production by Steam Reforming of Liquefied Natural Gas (LNG) over Trimethylbenzene-assisted Ordered Mesoporous Nickel-alumina Catalyst", *International Journal of Hydrogen Energy*, 38(21), pp.8751-8758 (2013).

8. H.W. Park, J.K. Kim, U.G. Hong, Y.J. Lee, **J.H. Choi**, Y. Bang, I.K. Song, "Catalytic Decomposition of 1,3-Diphenoxybenzene to Monomeric Cyclic Compounds over Palladium Catalysts Supported on Acidic Activated Carbon Aerogels", *Applied Catalysis A: General*, 456, pp.59-66 (2013).

9. J.K. Kim, **J.H. Choi**, D.R. Park, I.K. Song, "Etherification of n-Butanol to Di-n-butyl Ether over Keggin-, Wells-Dawson-, and Preyssler-type Heteropolyacid Catalysts", *Journal of Nanoscience and Nanotechnology*, 13(12), pp.8121-8126 (2013).

10. H.W. Park, U.G. Hong, Y.J. Lee, **J.H. Choi**, I.K. Song, "Catalytic Decomposition of 4-Phenoxyphenol to Aromatics over $Pd/Cs_XH_{3.0-X}PW_{12}O_{40}$/Activated Carbon Aerogel (X=2.0-3.0)",*Journal of Nanoscience and Nanotechnology*, 13(12), pp.7963-7968 (2013).

11. H.W. Park, U.G. Hong, Y.J. Lee, **J.H. Choi**, I.K. Song, "Catalytic

Decomposition of 4-Phenoxyphenol to Aromatics over Pd/X$Cs_{2.5}H_{0.5}PW_{12}O_{40}$/ACA (X=10, 20, 30, 40, and 50 wt%) Catalysts", *Applied Catalysis A: General*, 437-438, pp.112-119 (2012).

12. J.K. Kim, **J.H. Choi**, J.H. Song, J. Yi, I.K. Song, "Etherification of n-Butanol to Di-n-butyl Ether over $H_nXW_{12}O_{40}$ (X= Co^{2+}, B^{3+}, Si^{4+}, and P^{5+}) Keggin Heteropolyacid Catalysts", *Catalysis Communications*, 27, pp.5-8 (2012).

13. S. Park, **J.H. Choi**, T.J. Kim, Y.-M. Chung, S.-H. Oh, I.K. Song, "Direct Synthesis of Hydrogen Peroxide from Hydrogen and Oxygen over Pd/$Cs_xH_{3-x}PW_{12}O_{40}$/MCF (X=1.7, 2.0, 2.2, 2.5, and 2.7) Catalysts", *Journal of Molecular Catalysis A: Chemical*, 353-354, pp.37-43 (2012).

14. S. Park, **J.H. Choi**, T.J. Kim, Y.-M. Chung, S.-H, Oh, I.K. Song, "Direct Synthesis of H_2O_2 from H_2 and O_2 over Pd Catalyst Supported on $Cs_{2.5}H_{0.5}PW_{12}O_{40}$-MCF Silica", *Catalysis Today*, 185(1), pp.162-167 (2012).

15. D.R. Park, **J.H. Choi**, S. Park, I.K. Song, "Reduction Potential, UV-visible Absorption Edge Energy, and Oxidation Catalysis of Niobium-containing $H_{3+x}PW_{12-x}Nb_xO_{40}$ Keggin and $H_{6+x}P_2W_{18-x}Nb_xO_{62}$ Wells-Dawson Heteropolyacid Catalysts", *Applied Catalysis A: General*, 394(1-2), pp.201-208 (2011).

16. S. Park, D.R. Park, **J.H. Choi**, T.J. Kim, Y.-M. Chung, S.-H. Oh, I.K. Song, "Direct Synthesis of Hydrogen Peroxide from Hydrogen and Oxygen over Palladium Catalyst Supported on $H_3PW_{12}O_{40}$-incorporated MCF Silica", *Journal of Molecular Catalysis A: Chemical*, 336(1-2), pp.78-86 (2011).

17. H.W. Park, S. Park, D.R. Park, **J.H. Choi**, I.K. Song, "Catalytic Decomposition of Phenethyl Phenyl Ether and Benzyl Phenyl Ether to Aromatics over Pd/$Cs_xH_{3.0-x}PW_{12}O_{40}$ (X=2.0, 2.3, 2.5, 2.8, and 3.0)", *Journal of Industrial and*

Engineering Chemistry, 17(4), pp.736-741 (2011).

18. H.W. Park, S. Park, D.R. Park, **J.H. Choi**, I.K. Song, "Catalytic Decomposition of Benzyl Phenyl Ether to Aromatics over Cesium-exchanged Heteropolyacid Catalyst", *Korean Journal of Chemical Engineering*, 28(5), pp.1177-1180 (2011).

19. S. Park, D.R. Park, **J.H. Choi**, T.J. Kim, Y.-M. Chung, S.-H. Oh, I.K. Song, "Direct Synthesis of Hydrogen Peroxide from Hydrogen and Oxygen over Insoluble $Cs_{2.5}H_{0.5}PW_{12}O_{40}$ Heteropolyacid Supported on Pd/MCF", *Journal of Molecular Catalysis A: Chemical*, 332(1-2), pp.76-83 (2010).

20. H.W. Park, S. Park, D.R. Park, **J.H. Choi**, I.K. Song, "Decomposition of Phenethyl Phenyl Ether to Aromatics over $Cs_xH_{3.0-x}PW_{12}O_{40}$ (X=2.0-3.0) Heteropolyacid Catalysts", *Catalysis Communications*, 12(1), pp.1-4 (2010).

21. D.R. Park, S. Park, **J.H. Choi**, I.K. Song, "Acidity of Group 5 Metal (V, Nb, Ta)-substituted Keggin and Wells-Dawson Heteropolyacid (HPA) Catalysts and Their Application to Esterification of Acetic Acid with Ethanol", *Catalysis Letters*, 135(3-4), pp.269-274 (2010).

Domestic papers published (Co-author)

1. 김정권, **최정호**, 이종협, 송인규, "Keggin형 $H_{3+x}PW_{12-x}Nb_xO_{40}$ (x=0, 1, 2, 3) 및 Wells-Dawson형 $H_{6+x}P_2W_{18-x}Nb_xO_{62}$ (x=0, 1, 2, 3) 헤테로폴리산 촉매를 이용한 n-Butanol로부터 Di-n-Butyl Ether의 제조", 화학공학, 50(2), pp.251-256 (2012).

Patents

Registered patents

1. 송인규, 이혜진, 조왕래, **최정호**, "디메틸카보네이트 제조용 갈륨 옥사이드-세륨 옥사이드-지르코늄 옥사이드 복합 촉매 및 상기 촉매를 이용한 디메틸카보네이트의 제조방법", 대한민국 특허출원 10-2011-0118902 (2011), 대한민국특허 제 1,318,255호 (2013).

Applied patents

1. 조왕래, 송인규, 강태훈, **최정호**, 최준선, "글리세린 탈수반응용 촉매, 이의 제조방법 및 상기 촉매를 이용하여 글리세린으로부터 아크롤레인을 제조하는 방법", 대한민국 특허출원 10-2014-0071548 (2014).

2. 송인규, 김정권, 홍웅기, **최정호**, "중형기공성 탄소에 담지된 양이온 치환 헤테로폴리산 및 귀금속 담지촉매, 그 제조방법 및 상기 촉매를 이용한 리그닌 화합물 분해 방법", 대한민국 특허출원 10-2013-0128048 (2013).

3. 송인규, 이종협, **최정호**, 박동률, 이윤재, "헤테로폴리산 촉매를 이용한 디부틸에테르 제조방법", 대한민국 특허출원 10-2011-0020933 (2011).

4. 송인규, 박동률, 방용주, **최정호**, 이윤재, "카본 에어로젤에 고정화된 헤테로폴리산 담지 촉매, 그 제조방법 및 상기 촉매를 이용한 이소프로판올의 산화반응에 의한 아세톤 제조방법", 대한민국 특허출원 10-2010-0021178 (2010).

Conferences

International conferences (First author)

1. **J.H. Choi**, T.H. Kang, Y. Bang, I.K. Song, "Scanning Tunneling Microscopy and Tunneling Spectroscopy Investigations of Nano-structured α_2-$K_6As_2W_{18-x}Mo_xO_{62}$ (x=0-3) Wells-Dawson Heteropolyacid Catalyst Monolayers", *NANO KOREA 2014*, P1404-002, COEX, Seoul, Korea (2014/7/2-4).

2. **J.H. Choi**, T.H. Kang, Y. Bang, J. Yoo, J.O. Jun, I.K. Song, "STM Investigation of Nano-structured α-$K_5PW_{11}O_{39}$(M OH_2) (M = Mn^{II}, Co^{II}, Ni^{II}, and Zn^{II}) Heteropolyacid Catalyst Monolayers",*NANO Korea 2013 Symposium*, P1303_006, Coex, Seoul, Korea (2013/7/10-12).

3. **J.H. Choi**, T.H. Kang, I.K. Song, "Redox Properties and Oxidation Catalysis of Transition Metal-substituted Wells-Dawson Heteropolyacids Probed by Scanning Tunneling Microscopy", *The ^{9th}World Congress of Chemical Engineering (The ^{15th} Asian Pacific Confederation Chemical Engineering Congress)*, P-01-135, COEX, Korea (2013/8/18-23).

4. **J.H. Choi**, J.K. Kim, S. Park, I.K. Song, "Redox Properties of Potassium Salts of Transition Metal-substituted Wells-Dawson Heteropolyacids Probed by Scanning Tunneling Microscopy", *The 10th NANO KOREA 2012 Symposium*, P1202_007, COEX, Korea (2012/8/16-18).

5. **J.H. Choi**, D.R. Park, S. Park, J.K. Kim, I.K. Song, "Scanning Tunneling Microscopy and Tunneling Spectroscopy Study of $H_6P_2Mo_xW_{18-x}O_{62}$ (x=0, 3, 9, 15, 18) Wells-Dawson Heteropolyacids", *The 15th International Congress on Catalysis*, 6608, Munich, Germany (2012/07/1-7).

6. **J.H. Choi**, D.R. Park, S. Park, I.K. Song, "Scanning Tunneling Microscopy

Study of Nano-structured Group 5 Metal-substituted Keggin and Wells-Dawson Heteropolyacid Catalysts", *The 9th International Nanotech Symposium & Exhibition in Korea* (NANO KOREA 2011), P1103_012, Kintex, Seoul, Korea (2011/8/24-26).

7. **J.H. Choi**, D.R. Park, I.K. Song, "Scanning Tunneling Microscopy and Tunneling Spectroscopy of Nano-structured $H_{6+x}P_2Mo_{18-x}V_xO_{62}$ Wells-Dawson Heteropolyacids", *The IEEE Nanotechnology Conference 2010* (IEEE Nano 2010), NKP_TS04_013, KINTEX, Seoul, Korea (2010/8/17-20).

International conferences (Co-author)

1. Y. Bang, S.J. Han, J. Yoo, **J.H. Choi**, J.K. Lee, I.K. Song, "Hydrogen Production by Steam Reforming of Liquefied Natural Gas (LNG) over Nickel Catalyst Supported on Mesoporous Phosphorus-modified Alumina Xerogel", *20th WHEC(World Hydrogen Energy Conference) 2014*, 58, Kwangju, Korea (2014/6/15-20).

2. Y. Bang, S.J. Han, J. Yoo, S. Park, **J.H. Choi**, J. Lee, I.K. Song, "Hydrogen Production by Steam Reforming of LNG over Nickel-phosphorus-alumina Catalyst Prepared by a Templating Sol-gel Method", *NANO KOREA 2014*, P1406_001, COEX, Seoul, Korea (2014/7/2-4).

3. T.H. Kang, **J.H. Choi**, J.S. Choi, I.K. Song, "Dehydration of Glycerin to Acrolein over Heteropolyacid Nano-catalyst Supported on Amorphous Silica-alumina", *NANO KOREA 2014*, P1403_028, COEX, Seoul, Korea (2014/7/2-4).

4. Y. Bang, S.J. Han, J. Yoo, **J.H. Choi**, K.H. Kang, I.K. Song, "Preparation of Structure-modified Ordered Mesoporous Nickel-alumina Catalyst for Hydrogen Production by Steam Reforming of Liquefied Natural Gas (LNG)", *International*

Conference on Hydrogen Production - 2014, P-45, Fukuoka, Japan (2014/2/2-5).

5. J.K. Kim, **J.H. Choi**, D.R. Park, I.K. Song, "Etherification of n-Butanol to Di-n-butyl Ether over Heteroatom-substituted Keggin Heteropolyacid Catalysts", *The 14th Korea-Japan Symposium on Catalysis*, GP09, Nagoya, Japan (2013/7/1-3).

6. T.H. Kang, **J.H. Choi**, J.S. Choi, I.K. Song, "Dehydration of Glycerol to Acrolein over Keggin-, Wells-Dawson- and Preyssler-type Heteropolyacid Nano-catalysts", *NANO Korea 2013 Symposium*, P1303_010, Coex, Seoul, Korea (2013/7/10-12).

7. J.K. Kim, H.W. Park, U.G. Hong, **J.H. Choi**, I.K. Song, "$Cs_xH_{3.0-x}PW_{12}O_{40}$ (X=2.0-3.0) Heteropolyacid Nano-catalysts for Catalytic Decomposition of 2,3-Dihydrobenzofuran to Aromatics", *NANO Korea 2013 Symposium*, P1303_009, Coex, Seoul, Korea (2013/7/10-12).

8. J.K. Kim, **J.H. Choi**, D.R. Park, J. Yi, I.K. Song, "Etherification of n-Butanol to Di-n-butyl Ether over Heteropolyacid Catalysts with Different Structure", *The 10th NANO KOREA 2012 Symposium*, P1208_022, COEX, Korea (2012/8/16-18).

9. S. Park, **J.H. Choi**, T.J. Kim, Y.-M. Chung, S.-H. Oh, I.K. Song, "Direct Synthesis of H_2O_2 from H_2 and O_2 over Pd Catalyst Supported on Heteropolyacid-MCF Silica", *The 13th Korea-Japan Symposim on Catalysis*, YO A-07, Jeju, Korea (2011/05/23-25).

Domestic conferences (First author)

1. **최정호**, 강태훈, 방용주, 송인규, "몰리브덴이 선택적으로 치환된 Wells-Dawson형 Tungstoarsenate의 산화환원 특성에 관한 연구", 2014년 한국화학공학회 추계학술회의, P촉매금-1, 대전 DCC (2014/10/22-24).

2. **최정호**, 강태훈, 방용주, 송인규, "서로 다른 중심원소를 가지는 Keggin형 헤테로폴리산의 산화환원 특성에 관한 연구", 2014년 한국공업화학회 춘계학술회의, 1P-259, 제주 ICC (2014/4/30-5/2).

3. **최정호**, 강태훈, 방용주, 송인규, "Keggin형 α-$H_nXW_{12}O_{40}$($X=Co^{2+}$, B^{3+}, Si^{4+}, and P^{5+}) 헤테로폴리산 촉매의 산화환원 및 반응활성에 관한 연구", 2014년 한국화학공학회 춘계학술회의, P촉매금-3, 창원 컨벤션센터 (2014/4/23-25).

4. **최정호**, 강태훈, 방용주, 강기혁, 송인규, "4주기 전이금속이 배위된 Keggin형 헤테로폴리산 촉매의 산화환원 특성에 관한 연구", 2013년 한국공업화학회 추계학술회의, 2P-181, 대전 컨벤션센터 (2013/10/30-11/1).

5. **최정호**, 강태훈, 방용주, 강기혁, 송인규, "Keggin형 α-$K_5PW_{11}O_{39}$(M?OH_2) ($M=Mn^{2+}$, Co^{2+}, Ni^{2+}, Zn^{2+}) 헤테로폴리산 촉매의 산화환원 및 반응활성에 관한 연구", 2013년 한국화학공학회 추계학술회의, P촉매목-10, 대구 EXCO (2013/10/23-25).

6. **최정호**, 강태훈, 송인규, "Wells-Dawson형 α_2-$K_8P_2W_{17}O_{61}$(M?OH_2) ($M=Mn^{2+}$, Fe^{2+}, Co^{2+}, Ni^{2+}, Zn^{2+})헤테로폴리산 촉매의 산화환원 및 반응활성에 관한 연구", 2013년 한국공업화학회 춘계학술회의, 1P-395, 제주 국제컨벤션센터 (2013/5/1-3).

7. **최정호**, 강태훈, 송인규, "4주기 전이금속이 배위된 Wells-Dawson형 헤테로폴리산 촉매의 산화환원 특성 및 반응활성에 관한 연구", 2013년 한국화학공학회 춘계학술회의, P촉매금-3, 광주 김대중컨벤션센터 (2013/4/24-26).

8. **최정호**, 김정권, 박동률, 송인규, "STM 분석을 통한 Keggin형 $H_4PW_{11}M_1O_{40}$ 및 Wells-Dawson형 $H_7P_2W_{17}M_1O_{62}$ (M=Nb, Ta) 헤테로폴리산의 산화환원 특성연구", 2012년 한국공업화학회 추계학술회의, 2P-181, 대전컨벤션센터 (2012/10/31-11/2).

9. **최정호**, 김정권, 박동률, 송인규, "5족 전이금속(Nb, Ta)이 단일 치환된 Keggin형 및 Wells-Dawson형 헤테로폴리산의 STM 연구", 2012년 한국화학공학회 추계학술회의, P촉매수-9, 부산 BEXCO (2012/10/24-26).

10. **최정호**, 송인규, 김정권, 박선영, "4주기 전이금속이 단일 치환된 Wells-Dawson형 헤테로폴리산의 STM 연구", 2012년 한국공업화학회 춘계학술회의, 2P-200, 김대중컨벤션센터 (2012/5/9-11).

11. **최정호**, 송인규, 김정권, 박선영, "STM 분석을 통한 Wells-Dawson형 $K_8P_2W_{17}O_{61}$(M?OH_2) (M=Mn^{II}, Fe^{II}, Co^{II}, Ni^{II}, Cu^{II}, and Zn^{II}) 헤테로폴리산의 산화환원 특성연구", 2012년 한국화학공학회 춘계학술회의, P촉매금-27, 제주ICC (2012/4/25-27).

12. **최정호**, 박동률, 김정권, 송인규, "STM 분석을 통한 니오븀이 배위된 Keggin형 헤테로폴리산의 산화환원 특성연구", 2011년 한국공업화학회 추계학술회의, 1P-261, 경원대학교 (2011/11/2-4).

13. **최정호**, 박동률, 김정권, 송인규, "니오븀이 배위된 $H_{6+x}P_2W_{18-}$

$_{x}Nb_{x}O_{62}$ Wells-Dawson형 헤테로폴리산의 STM 연구", 2011년 한국화학공학회 추계학술회의, P촉매목-10, 송도컨벤시아 (2011/10/26-28).

14. **최정호**, 박동률, 송인규, "n-Butanol의 탈수화반응을 통한 di-n-butyl ether의 제조", 2011년 한국공업화학회 춘계학술회의, 2P-296, 제주국제켄벤션센터 (2011/5/11-13).

15. **최정호**, 박동률, 송인규, "STM 연구를 통한 바나듐이 치환된 Wells-Dawson형 헤테로폴리산의 산화환원 특성 분석", 2011년 한국화학공학회 춘계학술회의, P촉매목-9, 창원켄벤션센터 (2011/4/27-29).

16. **최정호**, 박동률, 송인규, "Wells-Dawson형 헤테로폴리산의 그래파이트 표면증착을 통한 STM 연구", 2010년 한국공업화학회 추계학술회의, 2P-175, 대전컨벤션센터 (2010/10/27-29).

17. **최정호**, 박동률, 송인규, "그래파이트 표면에 증착된 Wells-Dawson형 헤테로폴리산의 STM 연구", 2010년 한국화학공학회 추계학술회의, P촉매금-8, 대전컨벤션센터 (2010/10/20-22).

18. **최정호**, 박동률, 박선영, 송인규, "5족 원소가 치환된 헤테로폴리산의 그래파이트 표면증착을 통한 STM 연구", 2010년 한국공업화학회 춘계학술회의, 2P-246, 부산 BEXCO (2010/5/13-14).

19. **최정호**, 박동률, 박선영, 송인규, "그래파이트 표면에 증착된 헤테로폴리산의 STM 연구", 2010년 한국화학공학회 춘계학술회의, P촉매목-6, 대구 EXCO (2010/4/21-23).

Domestic conferences (Co-author)

1. 강기혁, 홍웅기, 전진오, 방용주, **최정호**, 한승주, 송인규, "레늄-구리-카본 복합체 촉매 상에서 숙신산의 수소화를 통한 감마부티로락톤과 1,4-부탄디올의 제조", 2014년 한국화학공학회 추계학술회의, P촉매금-2, 대전 DCC (2014/10/22-24).

2. 강태훈, **최정호**, 최준선, 조왕래, 송인규, "$H_3PW_{12}O_{40}$/silica-alumina 촉매를 이용한 글리세린으로부터 아크롤레인의 합성", 2014년 한국화학공학회 추계학술회의, P촉매금-5, 대전 DCC (2014/10/22-24).

3. 방용주, 박승원, 한승주, 유재경, **최정호**, 송인규, "킬레이트화된 니켈 전구체의 함침을 통한 니켈/알루미나 촉매의 제조 및 액화천연가스의 수증기 개질 반응으로의 적용", 2014년 한국화학공학회 추계학술회의, P촉매금-11, 대전 DCC (2014/10/22-24).

4. 방용주, 한승주, 유재경, 박승원, **최정호**, 송인규, "탄소 입자를 주형 물질로 하는 중형기공성 니켈-인-알루미나 촉매의 제조 및 액화천연가스의 수증기 개질 반응으로의 적용", 2014년 한국공업화학회 춘계학술회의, 1P-256, 제주 ICC (2014/4/30-5/2).

5. 강태훈, **최정호**, 조왕래, 최준선, 송인규, "실리카 알루미나에 담지한 헤테로폴리산 담지 촉매 제조 및 글리세린으로부터 아크롤레인 합성", 2014년 한국공업화학회 춘계학술회의, 1P-257, 제주 ICC (2014/4/30-5/2).

6. 강태훈, **최정호**, 조왕래, 최준선, 송인규, "$H_3PW_{12}O_{40}$/Silica-alumina 촉매를 이용한 글리세린으로부터 아크롤레인의 합성", 2014년 한국화학공학회 춘계학술회의, P촉매금-6, 창원 컨벤션센터 (2014/4/23-25).

7. 방용주, 한승주, 유재경, 박승원, **최정호**, 송인규,“인이 도입된 중형기공성 니켈-알루미나 촉매 상의 액화천연가스의 수증기 개질 반응”, 2014년 한국화학공학회 춘계학술회의, O촉매목-10, 창원 컨벤션센터 (2014/4/23-25).

8. 방용주, 한승주, 유재경, **최정호**, 송인규, “인이 도입된 중형기공성 니켈-인-알루미나 에어로젤 촉매의 제조 및 액화천연가스의 수증기 개질 반응으로의 적용”, 2013년 한국공업화학회 추계학술회의, 2P-253, 대전 컨벤션센터 (2013/10/30-11/1).

9. 강태훈, **최정호**, 최준선, 송인규, “$H_3PW_{12}O_{40}$/silica-alumina 촉매를 이용한 글리세린으로부터 아크롤레인의 합성”, 2013년 한국공업화학회 추계학술회의, 2P-180, 대전 컨벤션센터 (2013/10/30-11/1).

10. 방용주, 한승주, 유재경, **최정호**, 송인규, “인이 도입된 중형기공성 니켈/알루미나 제어로젤 촉매 상의 액화천연가스의 수증기 개질 반응을 통한 수소 가스 생산”, 2013년 한국화학공학회 추계학술회의, P촉매목-2, 대구 EXCO (2013/10/23-25).

11. 강태훈, **최정호**, 최준선, 송인규, “실리카 알루미나에 담지한 헤테로폴리산 담지 촉매 제조 및 글리세린으로부터 아크롤레인을 합성하는 공정으로의 적용”, 2013년 한국화학공학회 추계학술회의, P촉매목-5, 대구 EXCO (2013/10/23-25).

12. 김정권, 홍웅기, **최정호**, 송인규, “$Cs_xH_{3.0-x}PW_{12}O_{40}$ (X=2.0-3.0) 헤테로폴리산 촉매를 이용한 리그닌 모델화합물로부터 방향족 생성에 관한 연구”, 2013년 한국공업화학회 춘계학술회의, 1P-442, 제주

국제컨벤션센터 (2013/5/1-3).

13. 김정권, 홍웅기, **<u>최정호</u>**, 송인규, "양이온이 치환된 헤테로폴리산 촉매를 이용한 리그닌 모델 화합물 분해", 2013년 한국화학공학회 춘계학술회의, P촉매금-4, 광주 김대중컨벤션센터 (2013/4/24-26).

14. 김정권, **<u>최정호</u>**, 박동률, 송인규, "헤테로폴리산 촉매를 이용한 n-butanol의 탈수화반응을 통한 di-n-butyl ether의 합성", 2012년 한국공업화학회 추계학술회의, 2P-184, 대전컨벤션센터 (2012/10/31-11/2).

15. 김정권, **<u>최정호</u>**, 박동률, 송인규, "다양한 구조의 헤테로폴리산을 이용한 Di-n-Butyl Ether의 합성에 관한 연구", 2012년 한국화학공학회 추계학술회의, P촉매수-8, 부산 BEXCO (2012/10/24-26).

16. 김정권, **<u>최정호</u>**, 이종협, 송인규, "Keggin형 헤테로폴리산 $H_{8-n}X^{n+}W_{12}O_{40}$ (X^{n+}= Co^{2+}, B^{3+}, Si^{4+}, and P^{5+})를 이용한 butanol로부터 di-n-butyl ether의 탈수화 반응", 2012년 한국공업화학회 춘계학술회의, 2P-167, 김대중컨벤션센터 (2012/5/9-11).

17. 김정권, **<u>최정호</u>**, 이종협, 송인규, "중심원소가 치환된 Keggin형 헤테로폴리산을 이용한 di-n-butyl ether의 합성에 관한 연구", 2012년 한국화학공학회 춘계학술회의, P촉매금-28, 제주ICC (2012/4/25-27).

18. 박선영, **<u>최정호</u>**, 김태진, 정영민, 오승훈, 송인규, "불용성 헤테로폴리산을 고정한 셀룰라폼 구조의 중형기공 실리카에 팔라듐을 담지한 촉매에 의한 과산화수소 직접 제조 반응에 관한 연구", 2011년 한국공업화학회 추계학술회의, 1P-259, 경원대학교 (2011/11/2-4).

19. 김정권, **최정호**, 이종협, 송인규, "헤테로폴리산 촉매를 이용한 n-butanol로부터 di-n-butyl ether 합성에 관한 연구", 2011년 한국공업화학회 추계학술회의, 1P-266, 경원대학교 (2011/11/2-4).

20. 박선영, **최정호**, 김태진, 정영민, 오승훈, 송인규, "산소와 수소로부터 과산화수소를 직접 제조하는 반응에서 공정 변수의 영향에 관한 연구", 2011년 한국화학공학회 추계학술회의, P촉매목-7, 송도컨벤시아 (2011/10/26-28).

21. 김정권, **최정호**, 이종협, 송인규, "전이금속이 배위된 헤테로폴리산 촉매를 이용한 di-n-butyl ether 합성에 관한 연구", 2011년 한국화학공학회 추계학술회의, P촉매목-13, 송도컨벤시아 (2011/10/26-28).

22. 박선영, **최정호**, 김태진, 정영민, 오승훈, 송인규, "헤테로폴리산을 고정한 중형기공 실리카에 팔라듐을 담지한 촉매에 의한 과산화수소 직접 제조 반응에 관한 연구", 2011년 한국화학공학회 춘계학술회의, O촉매E금-5, 창원켄벤션센터 (2011/4/27-29).

23. 박동률, **최정호**, 박선영, 송인규, "Nb이 배위된 Keggin 및 Wells-Dawson형 헤테로폴리산(HPA)의 산화환원 특성 및 반응 활성에 관한 연구", 2010년 한국공업화학회 추계학술회의, 2P-170, 대전컨벤션센터 (2010/10/27-29).

24. 박선영, 박동률, **최정호**, 김태진, 정영민, 오승훈, 송인규, "헤테로폴리산이 고정화된 중형기공 실리카에 팔라듐-금을 담지한 촉매를 이용한 과산화수소 직접 제조 반응에 관한 연구", 2010년 한국공업화학회 추계학술회의, 2P-171, 대전컨벤션센터 (2010/10/27-29).

25. 박해웅, 박선영, 박동률, **최정호**, 송인규, "세슘 이온이 치환된 헤테로폴리산을 이용한 리그닌 모델 화합물 분해", 2010년 한국공업화학회 추계학술회의, 2P-176, 대전컨벤션센터 (2010/10/27-29).

26. 박선영, 박동률, **최정호**, 김태진, 정영민, 오승훈, 송인규, "헤테로폴리산이 도입된 셀룰라폼 구조의 중형기공 실리카에 팔라듐을 담지한 촉매를 이용한 과산화수소 직접 제조 반응에 관한 연구", 2010년 한국화학공학회 추계학술회의, P촉매금-1, 대전컨벤션센터 (2010/10/20-22).

27. 박동률, 박선영, **최정호**, 송인규, "니오븀을 포함하는 $H_{3+x}PW_{12-x}Nb_xO_{40}$ Keggin 및 $H_{6+x}P_2W_{18-x}Nb_xO_{62}$ Wells-Dawson형 헤테로폴리산의 촉매 작용", 2010년 한국화학공학회 추계학술회의, P촉매금-4, 대전컨벤션센터 (2010/10/20-22).

28. 박해웅, 박선영, 박동률, **최정호**, 송인규, "$Pd/Cs_xH_{3.0-x}PW_{12}O_{40}$ (X=2.0, 2.3, 2.5, 2.8, 3.0) 촉매를 이용한 리그닌 모델 화합물 분해', 2010년 한국화학공학회 추계학술회의, P촉매금-9, 대전컨벤션센터 (2010/10/20-22).

29. 박동률, **최정호**, 송인규, "5족 금속(M=V, Nb, Ta)이 배위된 Keggin 및 Wells-Dawson형 헤테로폴리산의 촉매 작용", 2010년 한국공업화학회 춘계학술회의, 2P-240, 부산 BEXCO (2010/5/13-14).

30. 박해웅, **최정호**, 송인규, "헤테로폴리산 촉매를 이용한 리그닌 분해 반응", 2010년 한국공업화학회 춘계학술회의, 2P-242, 부산 BEXCO (2010/5/13-14).

31. 박선영, 박동률, **최정호**, 김태진, 정영민, 오승훈, 송인규, "산성기능기가

도입된 셀룰라폼 구조의 중형기공 실리카에 담지된 팔라듐 촉매를 이용한 과산화수소 직접 제조 반응에 관한 연구", 2010년 한국공업화학회 춘계학술회의, 2P-252, 부산 BEXCO (2010/5/13-14).

32. 박선영, 박동률, **최정호**, 김태진, 정영민, 오승훈, 송인규, "헤테로폴리산이 고정화된 셀룰라폼 구조의 중형기공 실리카에 담지된 팔라듐 촉매를 이용한 과산화수소 직접 제조 반응에 관한 연구", 2010년 한국화학공학회 춘계학술회의, P촉매목-8, 대구 EXCO (2010/4/21-23).

33. 박동률, **최정호**, 송인규, "5족 금속을 포함하는 Keggin 및 Wells-Dawson형 헤테로폴리산(HPA)의 촉매 특성 및 반응 활성에 관한 연구", 2010년 한국화학공학회 춘계학술회의, P촉매목-11, 대구 EXCO (2010/4/21-23).

34. 박해웅, **최정호**, 송인규, "산 촉매를 이용한 리그닌 모델 화합물 분해 반응", 2010년 한국화학공학회 춘계학술회의, P촉매목-12, 대구 EXCO (2010/4/21-23).